Deep Learning-Assisted Digital Image Techniques for In-situ Damage Characterization of Non-crimp Fabric Reinforced Reactive Thermoplastic Composites

by

Erli Shi

A thesis

presented to the University of Waterloo

in fulfillment of the

thesis requirement for the degree of

Doctor of Philosophy

in

Mechanical and Mechatronics Engineering

Waterloo, Ontario, Canada, 2025

© Erli Shi 2025

Examining Committee Membership

The following served on the examining committee for this thesis. The decision of the examining committee is by majority vote.

Supervisor	John Montesano, Ph.D. Associate Professor, University of Waterloo
External Examiner	Farid Taheri, Ph.D. Professor, Dalhousie University
Internal Member	Hamid Jahed, Ph.D. Professor, University of Waterloo
Internal Member	Elliot Biro, Ph.D. Associate Professor, University of Waterloo
Internal-external Member	Thomas Willett, Ph.D. Associate Professor, University of Waterloo

Author's Declaration

This thesis consists of material all of which I authored or co-authored: see Statement of Contributions included in the thesis. This is a true copy of the thesis, including any required final revisions, as accepted by my examiners.

I understand that my thesis may be made electronically available to the public.

Statement of Contributions

I am responsible for the writing, conception, methodology, software development, formal analysis, investigation, validation, visualization, and data curation of all the research tasks presented in this work. I gratefully acknowledge the valuable contributions and collaboration of my co-authors in the preparation and publication of the associated journal papers.

Professor John Montesano: Supervision, Writing – Review & Editing, Conceptualization, Validation, Resources, Supervision, Project Administration, Funding Acquisition.

Yu Zeng: Appendix D – Data Curation, Review & Editing.

Khizar Rouf: Appendix D – Data Curation, Review & Editing.

Abstract

Infusible unidirectional non-crimp fabric (UD-NCF) glass fiber-reinforced reactive thermoplastic composites have emerged as promising candidates for primary load-bearing structures such as wind turbine blades due to their excellent mechanical performance, recyclability, and compatibility with liquid composite molding (LCM) processes. Their application in extreme service environments, including cyclic loading and low temperatures down to -50°C, places significant demands on structural integrity. These conditions highlight the need for a comprehensive understanding of the mechanical response, damage evolution, and failure mechanisms at -50°C to ensure long-term durability and reliability. Despite growing interest in thermoplastic composite systems, a critical gap remains in the literature, specifically the limited understanding of the damage behavior and failure characteristics under such demanding conditions. This research aims to develop an automated, AI-driven, in-situ non-destructive digital imaging technique for damage characterization of an infusible UD-NCF glass fiber-reinforced reactive thermoplastic acrylic (NCF-GF/acrylic) composite material. The study is structured around four main objectives, each addressed through a dedicated research task.

In Task 1, the mechanical performance and failure characteristics of NCF-GF/acrylic were investigated and compared to epoxy-based counterparts (NCF-GF/epoxy) at room (22°C) and low (–50°C) temperatures. Both materials exhibited increased stiffness and strength at LT under longitudinal, transverse, and in-plane shear loading conditions; however, NCF-GF/acrylic showed distinct damage features, including greater supporting fiber yarn splitting and breakage, reduced tow fiber bridging, and a transition from ductile to brittle behavior. This task provided key insights into the damage and failure mechanisms of NCF-GF/acrylic and demonstrated its potential as a viable alternative to epoxy-based systems for wind energy applications in cold climates.

An in-situ digital imaging technique was developed in Task 2 to characterize damage in NCF-GF/acrylic cross-ply laminates subjected to tensile loading at LT. A custom algorithm was developed to automatically detect the initiation and growth of 90° tow cracks, matrix cracks, and 0° tow cracks through image stacking, shift-correction, and thresholding. The laminates exhibited four stages of deformation/damage, including linear elastic, onset/growth of 90° fiber tow cracks, onset/growth of 0° fiber tow cracks, and progressive failure of 0° fiber tows. Although at LT, the effective laminate strength and stiffness increased by 4% and 13%, respectively, damage initiated sooner and propagated at a higher rate leading to a 60% increase in crack density at saturation. The digital imaging technique

proved to effectively detect local damage in the glass fiber/thermoplastic laminates, which led to a deeper understanding of their low-temperature deformation response, damage characteristics, and damage tolerance.

Through Task 3, a novel integrated digital imaging technique was developed to automatically characterize damage and simultaneously monitor stiffness degradation in NCF-GF/acrylic cross-ply laminates subject to tension-tension cyclic loading. Under a peak stress of 50% UTS, the laminate exhibited four distinct stages of stiffness degradation, including a significant drop during the first cycle due to 90º fiber tow crack initiation, a gradual decrease due to crack multiplication and propagation up to saturation, a stable phase comprising localized delamination crack propagation, and a sudden drop prior to specimen failure. Under a peak stress of 75% UTS, both 0º and 90º fiber tow cracks developed during the first stage followed by an accelerated growth rate and reduced 90º tow crack density at saturation. The integrated digital imaging technique proved to effectively correlate damage events with stiffness degradation, leading to a deeper understanding of the fatigue behavior of glass fiber/thermoplastic composites.

A deep learning based convolutional neural network was integrated with digital imaging technique to characterize damage in NCF-GF/acrylic composite laminates in Task 4. Images from prior experimental studies were preprocessed and annotated with six feature-related classes, which were subsequently divided into training and testing sets. A U-Net architecture incorporating skip connections, dropout, and weighted Dice loss function was employed. Results showed that smaller batch sizes achieved the lowest weighted Dice loss and the highest Dice coefficients. Notably, the Dice coefficient improved significantly from ~0.736 for balanced class weights to ~0.840 for highly biased class weights, representing a 14.1% increase in the prediction accuracy of 90º tow cracks. Early stopping at appropriate epochs effectively minimized overfitting while optimizing accuracy. The model demonstrated strong capability in identifying damage initiation, progression, and interaction, and was seamlessly integrated with automated crack counting algorithms for quantitative damage assessment. Furthermore, the dataset provides a robust foundation for future research on advanced deep learning methodologies for damage characterization in non-crimp fabric composites.

Acknowledgements

This thesis would not have been possible without the generous support of many individuals and organizations, to whom I extend my deepest gratitude. First and foremost, I am especially grateful to my supervisor, Professor John Montesano, for granting me the remarkable opportunity to contribute to this project and for welcoming me into his esteemed research group. His exceptional mentorship, insightful guidance, and unwavering support have been instrumental at every stage of this endeavor.

The execution of the experimental work in this research project would not have been possible without the support of Professor Hamid Jahed, the experienced research staff from the Fatigue and Stress Analysis Lab, and the technicians from the Department of Mechanical and Mechatronics Engineering. I would like to express my sincere thanks to Tom Gawel, Jason Benninger, Eckhard Budziarek, Richard Gordon, and Alan Woo for their unparalleled assistance throughout the experimental phase. A special note of thanks is owed to Dr. Behzad Behravesh for his dedicated training, guidance, and support in operating the testing equipment and troubleshooting the test setup.

I also gratefully acknowledge the generous financial support provided by several organizations. The Ontario Center of Innovation (OCI), the Natural Sciences and Engineering Research Council of Canada (NSERC), Borrum Energy Solutions, and the China Scholarship Council (CSC) played a crucial role in funding this research. The Saertex Group is also acknowledged for providing the unidirectional non-crimp fabric used in this research.

I would like to express my heartfelt appreciation to my beloved parents, Changzhi Shi and Heling Bao, whose unwavering love and support have been a constant source of strength throughout the most challenging moments of this journey. I am deeply grateful to my wife, Lin Liu, as well as my mother-in-law, Tongfan Zhang, and father-in-law, Yonghai Liu, for their understanding, encouragement, and the many sacrifices they made, which allowed me to dedicate myself fully to this research.

I am also thankful for the support and friendship of my colleagues and friends at the University of Waterloo. In particular, I would like to thank Milos Zivkovic, Khizar Rouf, Yu Zeng, and all other members of my research group for their continued encouragement, motivation, and insightful technical discussions throughout this journey.

Finally, I would like to express my sincere gratitude to my mentor, Dr. Lucy Li, from the National Research Council of Canada. Her guidance and support in all aspects, including career advice, skill development, and professional growth, have been truly invaluable.

Dedication

"To my beloved parents and my family."

Table of Contents

Examining Committee Membership ii

Author's Declaration iii

Statement of Contributions iv

Abstract v

Acknowledgements vii

Dedication ix

List of Figures xiii

List of Tables xix

List of abbreviations xx

Chapter 1 Introduction 1

1.1 Research Motivation 2

1.2 Thesis Outline 6

Chapter 2 Background and Literature Review 7

2.1 Overview of FRP Composite Materials and LCM Processes 8

2.2 Deformation Response and Damage Characteristics of FRP Composites Under Low Temperatures 10

2.3 Fatigue Response and Damage Characteristics of FRP Composites 15

2.4 Damage Monitoring Techniques 19

2.5 Deep Learning for Characterizing FRP Composites 23

Chapter 3 Research Objectives and Scope 26

3.1 Research Objectives 27

3.2 Scope of Work 29

3.2.1 Task 1 overview 29

3.2.2 Task 2 overview 30
3.2.3 Task 3 overview 30
3.2.4 Task 4 overview 31
Chapter 4 Synopsis of Research Methodology and Results 32
4.1 Material System and Panel Manufacturing 34
4.1.1 Material system description 34
4.1.2 VARTM process for panel manufacturing 35
4.1.3 In-situ polymerization behavior of resin during panel fabrication 36
4.2 Task 1: Characterization of UD-NCF Composite Material at Room and Low Ambient Temperatures 39
4.2.1 Experimental details 40
4.2.2 Longitudinal tensile response and fractographic analysis 41
4.2.3 Transverse tensile response and fractographic analysis 46
4.2.4 In-plane shear response and fractographic analysis 53
4.3 Task 2: In-situ Damage Characterization of Cross-ply UD-NCF Laminates under Quasi-static Tensile Loading using Developed Digital Imaging Technique 58
4.3.1 Experimental details 58
4.3.2 Laminate effective stress–strain response and modulus degradation 61
4.3.3 Qualitative damage analysis 64
4.3.4 Quantitative damage analysis 73
4.4 Task 3: Characterization of Damage Evolution and Stiffness Degradation of Cross-ply UD-NCF Laminates under Tension-Tension Cyclic Loading using Integrated Digital Imaging Technique 76
4.4.1 Experimental details 76
4.4.2 Verification of integrated digital imaging technique for fatigue testing 80

4.4.3 Rapid evaluation of fatigue threshold 82
4.4.4 Damage evolution and stiffness degradation 84
4.5 Task 4: Development of A Deep Learning-based CNN Model for Damage Characterization in UD-NCF composites 90
4.5.1 Methodology 90
4.5.2 Effect of batch sizes on characterization results 96
4.5.3 Effect of weights on characterization results 98
4.5.4 Effects of epochs on characterization results 100
4.5.5 Experimental validation on the entire dataset 102
Chapter 5 Conclusions and Recommendations 106
5.1 Conclusions 107
5.2 Contributions 112
5.3 Recommendations for Future Work 113
5.3.1 Material characterization 113
5.3.2 Integrated digital imaging technique 114
5.3.3 Deep learning-assisted damage characterization model 114
Letter of Copyrights Permission 115
References 119
Appendix A 140
Appendix B 141
Appendix C 142
Appendix D 143

List of Figures

Fig. 1-1. Schematic of typical wind turbine blade structures. 2
Fig. 1-2. Statistic in Canadian rural communities: (a) diesel and fossil fuel use [5]; (b) wind speed distribution [6]. 3
Fig. 1-3. (a) Schematic showing three regions of damage accumulation in FRP laminates under tension-tension cyclic loading [8] and examples of typical damage modes in FRP composites: (b) fiber-matrix debonding [10]; (c) fiber kinking [11]; (d) matrix cracking [12]; and (e) delamination and fiber fracture [13]. 4
Fig. 2-1. Typical structure of (a) thermoset polymers, and (b) thermoplastic polymers. 9
Fig. 2-2. Schematics of different types of NCFs [39]. 9
Fig. 2-3. Conventional VARTM process set-up [50]. 10
Fig. 2-4. Stress-strain curves of UD GF/epoxy composites at room and low temperatures [51]. 11
Fig. 2-5. Comparison of mechanical properties between glass fiber-reinforced thermoplastic acrylic and thermosetting epoxy laminates (a), and reference stress-strain curve under transverse tensile loading [48]. 13
Fig. 2-6. Comparison of in-plane shear failure characteristics between glass fiber-reinforced thermoplastic acrylic (a) and thermosetting epoxy (b) laminates [74]. 14
Fig. 2-7. (a) Ideal sinusoidal repeated stress cycle under tension-tension fatigue loading; (b) schematic of typical S-N curves for different applied mean stresses (b) [77]. 15
Fig. 2-8. Stiffness degradation and crack density evolution of $[+75^{o}_{3}/-75^{o}_{3}]_{s}$ laminate at different applied stress magnitudes [88]. 17
Fig. 2-9. Illustration of damage initiation beneath the supporting transverse fiber bundles [100]. 19
Fig. 2-10. Illustration of crack counting algorithm based on Gabor filter [26]. 23
Fig. 2-11. Example of a typical CNN architecture (a) and U-Net architecture (b) [161]. 25
Fig. 3-1. Schematic showing the research plan. 29
Fig. 4-1. Architecture of UD-NCF glass fiber reinforcement: (a) surface with tricot stitch pattern, and (b) opposite surface with transversal supporting glass fiber yarns. 34
Fig. 4-2. Schematic of VARTM process setup used to fabricate flat panels. 35
Fig. 4-3. Temperature profile and thermographs captured during resin infusion and polymerization of the UD-NCF composite panels at ambient temperature (phases I - IV of process are shown). Note, the size of the ROI indicated in the thermographs is 250 mm × 250 mm. 36

Fig. 4-4. Longitudinal tensile results at RT and -50°C: (a) average stress-strain curves with scatter bars shown; (b), (c), and (d) comparison of mechanical properties. 43
Fig. 4-5. Fractography of UD-NCF GF/acrylic subjected to longitudinal tensile loading at: (a), (c), and (e) RT; (b), (d), and (f) -50°C. 44
Fig. 4-6. Fractography of UD-NCF GF/epoxy subjected to longitudinal tensile loading at: (a), (c), and (e) RT; (b), (d), and (f) -50°C. 45
Fig. 4-7. Transverse tensile results at RT and -50°C: (a) average stress-strain curves with scatter bars shown; (b), (c), and (d) comparison of mechanical properties. 48
Fig. 4-8. Representative fracture surface and strain contours (revealing transverse cracks within fiber tows for indicated applied uniaxial strain) of UD-NCF GF/acrylic subjected to transverse tensile loading at: (a), (b) RT; (c), (d) -50°C (T*: frame prior to ultimate failure). 49
Fig. 4-9. Representative fracture surface and strain contours (revealing transverse cracks within fiber tows for indicated applied uniaxial strain) of UD-NCF GF/epoxy subjected to transverse tensile loading at: (a), (b) RT; (c), (d) -50°C (T*: frame prior to ultimate failure). 50
Fig. 4-10. Fractography of UD-NCF GF/acrylic subjected to transverse tensile loading at: (a) (b) RT; (c) (d) -50°C. 51
Fig. 4-11. Fractography of UD-NCF GF/epoxy subjected to transverse tensile loading at: (a) (b) RT; (c) (d) -50°C. 52
Fig. 4-12. In-plane shear results at RT and -50°C: (a) average stress-strain curves with scatter bars shown; (b), (c), and (d) comparison of mechanical properties. 54
Fig. 4-13. Fractography of UD-NCF GF/acrylic subjected to 10° off-axis tensile loading at: (a), (c), and (e) RT; (b), (d), and (f) -50°C. 56
Fig. 4-14. Fractography of UD-NCF GF/epoxy subjected to 10° off-axis tensile loading at: (a), (c), and (e) RT; (b), (d), and (f) -50°C. 57
Fig. 4-15. (a) Image of the material microstructure and laminate plies; (b) test specimen configuration and dimension 59
Fig. 4-16. Digital imaging technique for in-situ damage monitoring with environmental chamber set-up for testing at -50°C (only one digital camera is used for damage monitoring). 60
Fig. 4-17. Illustration of image processing to identify cracks: a) original image of specimen containing cracks; b) processed image with cracks identified in red. 60

Fig. 4-18. Quasi-static tensile test results at 22°C and -50°C for the cross-ply specimens: (a) stress-strain responses; (b) normalized longitudinal modulus degradation curves (stages I-IV are indicated); (c) mechanical property comparison (average values and standard deviation shown in bar charts). ... 63
Fig. 4-19. Schematic of the main observed damage modes: (a) specimen surface view; (b) specimen edge view with resin rich area and with supporting glass fiber yarns between adjacent 90° fiber layers, respectively; (c) specimen cross-sectional view. ... 64
Fig. 4-20. Surface image captured by the developed digital imaging technique and the corresponding microscopic observation on the edge and cross-section of the same specimen. ... 65
Fig. 4-21. Intra-laminar damage evolution in cross-ply laminates at 22°C (units for scales: cm). ... 66
Fig. 4-22. Micro-scale damage observation of RT samples tested up to: (a) 110 MPa; (b) 400 MPa. 67
Fig. 4-23. Fractography of specimen tested at 22°C: (a) image of fracture surface; (b) micrograph of fracture surface view; (c) micrograph of fracture edge view. ... 68
Fig. 4-24. Intra-laminar damage evolution in cross-ply laminates at -50°C (units for scales: cm). ... 69
Fig. 4-25. Micro-scale damage observation of LT samples tested up to: (a) 116 MPa; (b) 230 MPa; (c) 440 MPa. ... 71
Fig. 4-26. Fractography of specimen tested at -50°C: (a) image of fracture surface; (b) micrograph of fracture surface view; (c) micrograph of fracture edge view. ... 71
Fig. 4-27. Images of fracture surfaces for representative specimens captured using SEM: (a), (b) View on a fiber tow in the 90° ply for a specimen tested at 22°C; (c), (d) View on a fiber tow in the 90° ply for a specimen tested at -50°C. ... 72
Fig. 4-28. Schematic of damage evolution at 22°C and -50°C subjected to quasi-static tensile loading (only resin rich area between 90° fiber layers is shown). ... 73
Fig. 4-29. 90° tow crack density evolution at 22°C and -50°C. ... 75
Fig. 4-30. Examples of independent crack propagation at 22°C and -50°C: (a) curves for the first three cracks in different 90° fiber tows; (b) illustration of the length increasement for crack 1 at 22°C; (c) illustration of the length increasement for crack 1 at -50°C (Note that for clear crack visibility purposes, the detected cracks were offset, the color of the images were tuned, and the axis were labeled in pixels). ... 75
Fig. 4-31. Schematics for: a) specimen geometry and dimension; b) fatigue loading and damage observation profile. ... 77
Fig. 4-32. Test setup for use of the integrated digital imaging technique. ... 79

Fig. 4-33. Example of crack counting process. 80
Fig. 4-34. (a) Schematics of strain measurement methods considered for fully speckled and partially speckled specimens, (b) Comparison of normalized longitudinal stiffness degradation curves calculated from average strains in ROIs and virtual extensometers for the fully speckled and partially speckled specimens cyclically loaded in tension-tension at a peak stress of 50%UTS..... 81
Fig. 4-35. (a) Surface images of two specimens captured prior to testing (undamaged), during a preliminary fatigue test (original image containing damage), and after automated crack identification using the developed digital imaging technique (detected cracks). (b) The corresponding micrograph on the edge of a specimen. 82
Fig. 4-36. (a) Average surface temperature profile vs. number of cycles at indicated maximum stress magnitudes; (b) increase of average surface temperature after stabilization vs. maximum stress magnitudes; (c) temperature distribution (°C) map after stabilization within the gauge region captured by IR camera. 84
Fig. 4-37. Normalized longitudinal stiffness profiles for indicated peak cyclic stresses and direct correlation with damage evolution at different cyclic intervals. Note, the damage mechanisms automatically identified by the developed code are not identified in the captured images shown for improved clarity. 85
Fig. 4-38. Quantitative damage analysis at 50%UTS: a) 90º tow crack density evolution; (b) representative crack length increasement during fatigue testing for 90° tow cracks (Note that for clear crack visibility purposes, the detected cracks were offset and the axis were labeled in pixels)..... 86
Fig. 4-39. 90º tow crack density evolution at 75%UTS. 87
Fig. 4-40. Representative crack length increasement at 75%UTS for 0° tow cracks (Note that for clear crack visibility purposes, the detected cracks were offset and the axis were labeled in pixels)..... 88
Fig. 4-41. Microscopic observation of specimen edge damage at different cyclic intervals under a peak stress of 50%UTS with corresponding surface images: (a) undamaged specimen; (b) 1 cycle; (c) 26,000 cycles; (d) 49,950 cycles. 89
Fig. 4-42. Image preprocessing process: (a) initial image captured using the digital imaging technique with its histogram; (b) image ROI and its histogram; (c) image shift correction to ensure consistent damage monitoring within ROI (examples of stitching loops are circled in the first and last images for comparison). 91

Fig. 4-43. Examples of image annotation in CVAT: (a) the first image with its annotation; (b) the last image with its annotation; (c) masks for different classes. 91
Fig. 4-44. Examples of images and their corresponding masks in the testing set at: (a) first index group; (b) second index group; (c) third index group. 92
Fig. 4-45. U-Net architecture with the implementation of dropout regularization. 94
Fig. 4-46. Crack counting process (zoomed-in view): (a) segmented mask example for Class 1; (b) skeletonization to achieve uniform width for crack counting; (c) overlay of the skeletonized mask on the image for visualization. 96
Fig. 4-47. Effect of batch size on the training process: (a) weighted Dice loss over epochs; (b) mean Dice coefficient (Class 1 to Class 4) over epochs; (c) Dice coefficient for Class 1 over epochs. 97
Fig. 4-48. Effect of different class weights on the training process: (a) weighted Dice loss over epochs; (b) mean Dice coefficient (Class 1, Class3, and Class4) over epochs; (c) Dice coefficient for Class 1 over epochs. 98
Fig. 4-49. Visualization of the effect of different class weight configurations on model segmentation results: (a) raw input image with ground truth labels for Class 1 and Class 2; (b) segmented results using weight configuration [211111]; (c) segmented results using weight configuration [201111].. 100
Fig. 4-50. Effect of epochs on training and testing performance: (a) comparison of training and testing weighted Dice loss over epochs; (b) comparison of training and testing Dice coefficient for Class 1 over epochs. 101
Fig. 4-51. Visualization of model segmentation results in different index groups: (a) representative example from the first index group; (b) representative example from the second index group; (c) representative example from the third index group. 102
Fig. 4-52. Comparison and validation of segmented and actual 90° tow cracks (Class 1) under quasi-static tensile loading at -50°C: (a) example of crack initiation and evolution within 90° glass fiber tow (generated image on left); (b) crack development and interaction at ~429MPa (generated image on left); (c) microscope observation at the indicated location for validation. 103
Fig. 4-53. Comparison and validation of segmented and actual 90° tow crack (Class 1) under tension-tension cyclic loading at 75% UTS: (a) example of specimen surface image captured during cyclic loading; (b) segmented 90° tow cracks using the optimized deep learning model; (c) detected 90° tow cracks using conventional automated crack counting algorithms; and (d) microscope observation at the indicated location for validation. 104

Fig. 4-54. Comparison and validation of segmented and experimental results for 90° tow crack density evolution under quasi-static loading. 105

List of Tables

Table 2-1. Summary of capabilities for selected NDE techniques. 22
Table 3-1. Objectives, gaps, and tasks for the research work 27
Table 4-1. Comparison of mechanical, thermal, and physical properties of the matrix. 39
Table 4-2. Test parameters for material characterization. 40
Table 4-3. Specifications for the optical system 41
Table 4-4. Average longitudinal tensile properties (± STV). Change in low temperature property determined with respect to the corresponding room temperature property. 42
Table 4-5. Average transverse tensile properties (± STV). Change in low temperature property determined with respect to the corresponding room temperature property. 47
Table 4-6. Average in-plane shear properties (± STV). Change in low temperature property determined with respect to the corresponding room temperature property. 54
Table 4-7. Average laminate properties (± STV). 64
Table 4-8. Summary of training hyperparameters used in the experiments. 95

List of abbreviations

Abbreviation	Definition
3D	Three Dimensional
AE	Acoustic Emission
BN	Batch Normalization
BS	Batch Size
C–C	Compression-Compression
CDR	Crack Density Rate
CGR	Crack Growth Rate
CNN	Convolutional Neural Networks
Conv	Convolution
CTE	Coefficient of Thermal Expansion
CVAT	Computer Vision Annotation Tool
DI	Digital Imaging
DIC	Digital Image Correlation
DoP	Degree of Polymerization
FAST	Features from Accelerated Segment Test
FRP	Fiber-Reinforced Plastic
GF	Glass Fiber
IRT	Infrared Thermography
IR	Infrared
LCM	Liquid Composite Molding
LED	Light-Emitting Diode
LN_2	Liquid Nitrogen
LT	Low Temperature
MMA	Methyl Methacrylate
NCF	Non-Crimp Fabric
NDE	Non-Destructive Evaluation
NEG	Nippon Electric Glass
ReLU	Rectified Linear Unit
ROI	Region of Interest
RT	Room Temperature
SEM	Scanning Electron Microscope
SURF	Speeded Up Robust Feature
SVM	Support Vector Machines
S–N	Stress-Life
TP	Thermoplastic
TS	Thermoset

T–C	Tension-Compression
T–T	Tension-Tension
UD	Unidirectional
Up-conv	Up-Convolution
UTS	Ultimate Tensile Strength
UT	Ultrasonic Testing
VARTM	Vacuum-Assisted Resin Transfer Molding
VI	Visual Inspection
a	Current Crack Length
a_0	Initial Crack Length
E_1	Longitudinal Tensile Modulus
E_2	Transverse Tensile Modulus
f	Loading Frequency
G_{12}	In-Plane Shear Modulus
$G_{IC\text{-}initiation}$	Strain Energies Released During Initiation
$G_{IC\text{-}propagation}$	Strain Energies Released During Propagation
N	Total Number of Repeated Cycles
N_f	Cycles to Failure
R	Stress Ratio
S_L	In-Plane Shear Strength
T_g	Glass Transition Temperature
X_t	Longitudinal Tensile Strength
Y_t	Transverse Tensile Strength
γ_{12f}	In-Plane Strain at Failure
$\triangle T_{stab}$	Surface Temperature Rise at Stabilization
ε_{1f}	Longitudinal Tensile Strain at Failure
ε_{2f}	Transverse Tensile Strain at Failure
ρ	Crack Density
σ_a	Stress Amplitude
σ_{max}	Maximum Applied Stress
σ_{mean}	Mean Stress
σ_{min}	Minimum Applied Stress
σr	Stress Range
υ_{12}	In-Plane Major Poisson Ratio

Chapter 1
Introduction

1.1 Research Motivation

Fiber-reinforced plastic (FRP) composite materials have become mainstream in many industries due to their high specific strength and stiffness and excellent damage tolerance capabilities when compared to traditional metallic alloys, as well as an unparalleled ability to tailor their anisotropic deformation response[1]. The notable progress in FRP composites technology has resulted in practical implementation within aerospace, automotive, marine, wind energy, and civil structures. In the aerospace industry, for instance, carbon FRP composites have emerged as the material of choice for primary load-bearing components. This is evident in modern commercial aircraft like the Airbus 350 and the Boeing 787, where composites account for over 50% of the airframe structure by weight [2]. In the wind energy industry, glass FRP composites are the preferred materials for critical components such as wind turbine blade structures (Fig. 1-1) [3].

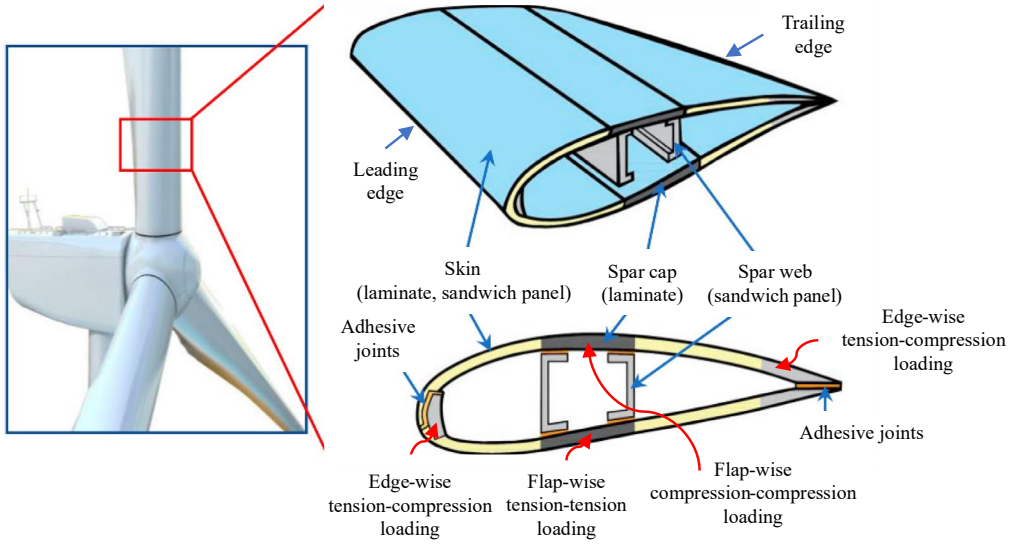


Fig. 1-1. Schematic of typical wind turbine blade structures.

For several decades, diesel generators have been used as the main source of energy for most remote communities in Northern Canada which are not connected to the electricity grid. Recent statistic shows that remote communities consume almost 700 million litres of diesel and other fossil fuels per year to produce electricity and heat [4], refer to Fig. 1-2a for diesel and fossil fuel use in Canadian rural regions. To mitigate environmental and health impacts and promote local economic development, renewable energy policies have been implemented aiming to eliminate diesel-powered electricity in remote communities by 2030 [4]. Microgeneration wind turbines provide a feasible alternative to

contribute towards producing electricity for individual dwellings in these regions. However, extreme operating conditions, such as low temperatures (e.g., -50°C) and strong winds (Fig. 1-2b), increase the demand on wind turbine blade structures. Thus, there is a need to investigate the effect of low temperature (–50°C) on the mechanical properties of FRP composite materials.

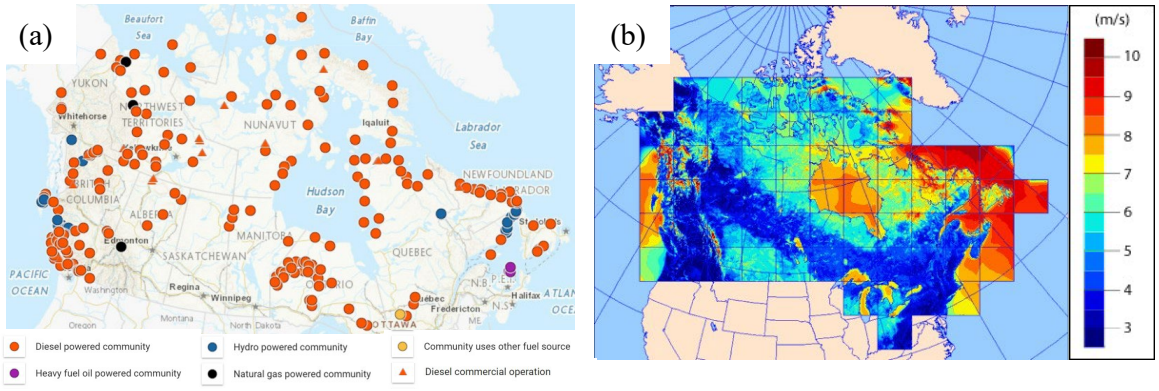


Fig. 1-2. Statistic in Canadian rural communities: (a) diesel and fossil fuel use [5]; (b) wind speed distribution [6].

During operation, the rotation of the blades induces centrifugal loads as well as cyclic bending in both the flap-wise and edge-wise directions as a result of changing aerodynamic and gravitational loads. These cyclic loads can cause damage to evolve and the stiffness of FRP composites to degrade (Fig. 1-3a) [7], resulting in reduced performance over time. The microstructure of FRP composites inherently promotes the development of localized damage mechanisms and their complex interactions, whereby the material is able to tolerate the damage and resist failure [9]. Intralaminar damage mechanisms that have been commonly observed include matrix cracks, fiber-matrix debonds, and fracture or kinking of fibers, while delamination cracks may also develop when interlaminar stresses are sufficiently large (Fig. 1-3b-e). Given that wind turbines are typically designed for a service life of 25–30 years, understanding the fatigue behavior and damage mechanisms of blade materials is essential for ensuring long-term durability and structural efficiency.

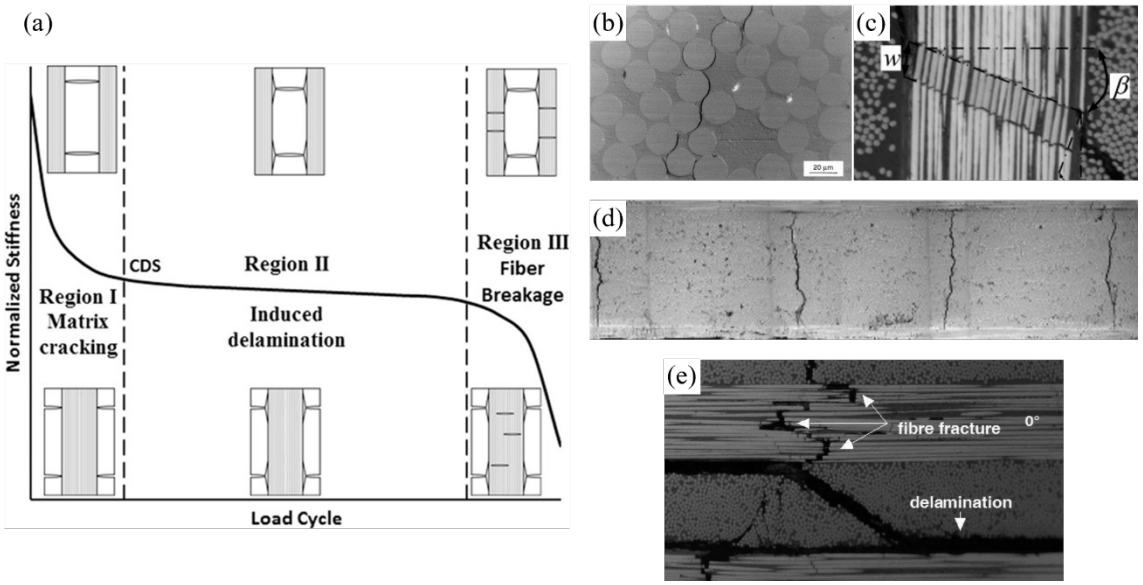


Fig. 1-3. (a) Schematic showing three regions of damage accumulation in FRP laminates under tension-tension cyclic loading [8] and examples of typical damage modes in FRP composites: (b) fiber-matrix debonding [10]; (c) fiber kinking [11]; (d) matrix cracking [12]; and (e) delamination and fiber fracture [13].

Traditional wind turbine blades are typically manufactured from fiber-reinforced/epoxy laminates using a liquid composite molding processes (LCM) such as resin infusion [14],[15]. These thermoset-based composites offer excellent mechanical properties and moderate curing temperature range. However, they have notable drawbacks when used in low-temperature conditions as they have the potential to exhibit brittle failure and consequently an increased susceptibility to delamination [16], [17]. Reduced fracture toughness at low temperatures, in conjunction with the ecological requirements for material recyclability, have prompted further development of fiber-reinforced thermoplastic (TP) composites. In general, manufacturing of fiber-reinforced TP composites with traditional TP resins, such as polyesteretherketone, polyurethane, and polypropylene among others, requires high processing temperatures and pressures to decrease resin viscosity and promote fiber wet out as well as costly equipment and tooling [18], [19]. Resin infusible glass fiber/reactive thermoplastic composite materials are an interesting alternative, which may provide several benefits including improved damage tolerance, fracture toughness, and fatigue resistance at low temperatures as well as feasible end-of-life recyclability options [20]. To ensure sustained and widespread usage of these sustainable candidate

materials for wind turbine blades, their mechanical and damage behavior must be investigated, particularly under low-temperature conditions. This better understanding will enable the optimization of these materials to achieve their maximum potential.

Given the complex and progressive nature of damage in FRP composites, it is essential to implement reliable methods for damage detection and monitoring. To effectively assess and monitor the damage process, a range of non-destructive evaluation (NDE) techniques has been developed. Traditional methods such as visual inspection (VI), ultrasonic testing (UT), and X-ray radiography have been widely used to detect surface and internal defects [21]. However, these techniques often suffer from limitations in resolution, accessibility, or sensitivity to environmental conditions [21]. More advanced techniques like acoustic emission (AE), infrared thermography (IRT), and digital image correlation (DIC) allow for in-situ monitoring and provide insights into damage initiation and progression under realistic loading conditions [22]. However, these techniques do not directly detect damage and may be difficult to calibrate. Digital imaging (DI) techniques have gained significant attention for their ability to capture both surface and sub-surface damage phenomena such as transverse cracks and delamination in FRP composites [23]. DI represents a fast, easy-to-implement, cost-effective, and data rich NDE approach, particularly suitable for composites with relatively translucent constituents. It can be effectively integrated with automated algorithms to quantify the damage [24], [25], [26]. However, existing methods often oversimplify crack geometry, overlook damage interactions, and require extensive parameter tuning. Recent advancements in machine learning and image-processing algorithms have addressed some of these challenges by enhancing detection accuracy and enabling more robust automated qualitative and quantitative damage assessment [27]-[29].The integration of machine learning with digital imaging techniques has the potential to contribute substantially to a more robust understanding of damage evolution and failure mechanisms in FRP composites. Therefore, it is critical to develop integrated digital imaging approaches that not only detect and classify damage with high fidelity but also correlate the observed damage with material degradation metrics such as crack density evolution and stiffness degradation. Such capability would enable more effective real-time monitoring, support the development of accurate predictive models, and ultimately improve the safety and reliability of composite components in service-critical applications.

1.2 Thesis Outline

This dissertation follows a manuscript-based format, comprising a synopsis of the results from a series of publications. Chapter 2 provides relevant background information and a comprehensive literature review on FRP composite materials, the quasi-static and fatigue response and failure characteristics of composites, damage monitoring techniques, and machine learning models. Chapter 3 outlines the main objectives and scope of the proposed research. Chapter 4 presents a synopsis of the research methodology and key results, while Chapter 5 provides conclusions and recommendations for future research. The remainder of the dissertation comprises four appendices, each containing a published or submitted peer-reviewed research article that serve to detail the research results.

Chapter 2

Background and Literature Review

2.1 Overview of FRP Composite Materials and LCM Processes

FRP composites typically comprise two primary constituents: a reinforcing fiber phase that is embedded within a polymer matrix phase. These constituents combine to form a heterogeneous and potentially anisotropic material, exhibiting distinct mechanical properties along different directions. The polymer matrix can be classified as either thermoset (TS) or thermoplastic (TP), which have distinct mechanical properties and feasible manufacturing processes for the corresponding composite material.

Thermosetting polymers, such as epoxy, unsaturated polyester, vinyl esters, and polyimides, are initially in a liquid state and undergo an irreversible curing process, typically thermally activated, during which cross-linking reactions occur (Fig. 2-1a). This results in a three-dimensional covalently bonded network, offering excellent mechanical properties, high thermal stability, chemical resistance, and dimensional rigidity [30]. However, once cured, TS cannot be remelted or reshaped, limiting their recyclability and reprocessing ability. In contrast, TP polymers, such as polyesteretherketone, polyurethane, and polypropylene, consist of long linear or branched molecular chains with minimal or no cross-linking (Fig. 2-1b). These polymers soften when heated and solidify upon cooling, offering advantages such as recyclability, reprocessability, short processing cycles, and higher impact resistance [19], [30]. However, conventional TP resins are not compatible with LCM processes, as they require high processing temperatures and pressures to decrease resin viscosity and promote fiber wet out as well as costly equipment and tooling [18], [19]. Alternatively, in-situ polymerizable monomeric or oligomeric reactive TP materials are compatible with LCM processes, such as polybutylene terephthalate, polyamide-6/12, thermoplastic polyurethane, and polycarbonate, which require molds heated to elevated temperatures to achieve polymerization. This characteristic makes the manufacturing of large-scale structures with reactive TPs, such as wind turbine blades, indeed challenging due to the added expense of high-temperature tooling. As a result, reactive TPs are rarely used in comparison to their thermoset counterparts in wind turbine blades [31], [32]. The growing interest in room-temperature polymerizable fiber-reinforced TP composites with excellent mechanical properties has led to the development of acrylic-based Elium® resins, which consist of methyl methacrylate monomer and acrylic copolymers that undergo free radical in-situ polymerization at room temperature. Moreover, the low viscosity of Elium® resins (i.e., 100-200 mPa.s) makes them suitable for use with LCM processes. The compatibility to produce large-scale composite structures, formability, and recyclability of this resin have recently been demonstrated [33]-[38].

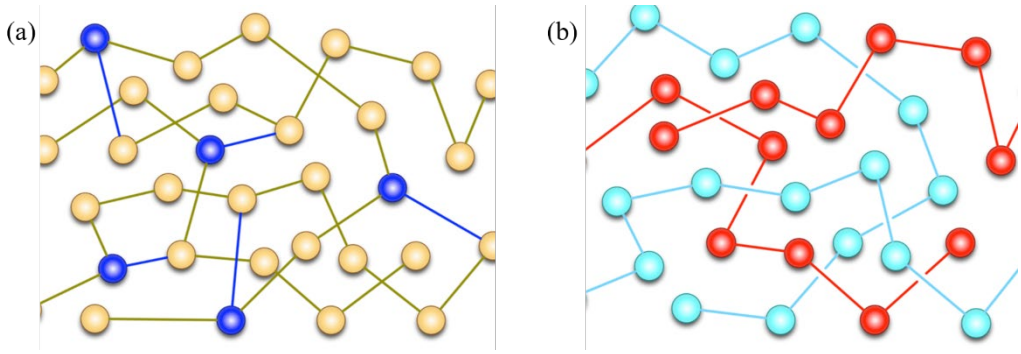


Fig. 2-1. Typical structure of (a) thermoset polymers, and (b) thermoplastic polymers.

The reinforcing fiber phase can be classified as either discontinuous or continuous. Commonly used continuous fibers for structural FRP composite applications include carbon, glass, Kevlar, and boron. These fibers exist in various forms, such as unidirectional (UD) or as a fabric. Reinforcement fabrics can have various forms, including woven, braided, and non-crimp fabrics (NCFs), which are extensively used with LCM processes. However, the in-plane mechanical properties of LCM composites are often compromised as a result of inherent fiber crimp in woven and braided fabrics [39], [40]. The limitation with conventional fabrics has prompted the use of NCFs that comprise stitch bonded UD fiber tows with minimal out-of-plane crimp. UD-NCFs allow for ease of handling during LCM processing and excellent formability during draping [39],[41] and comprise single layer of UD fiber tows that are stitched together which can be stacked in multiple orientations to form a laminate. Bidirectional and multidirectional NCFs contain multiple layers of UD fiber tows that are all stitched together using a lightweight yarn, typically made of polyester, refer to Fig. 2-2 for different types of NCFs. The architecture creates a fabric that possesses both structural integrity and minimized fiber crimp. Despite the improvements in the mechanical properties and the reduction in the manufacturing cost, several characteristics of NCFs have been found to influence the mechanical properties of the manufactured composite products, such as the stitching pattern (or stitching parameters), the size of fibers tows, and the orientation of layers, and the complex microstructures [42]-[46].

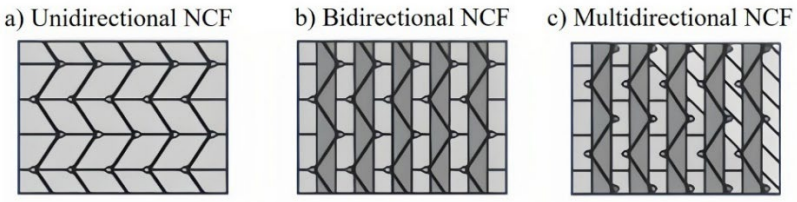


Fig. 2-2. Schematics of different types of NCFs [39].

Composite parts manufactured using UD fibers pre-impregnated with resin (i.e., UD tapes), typically laid manually or robotically and consolidated in an autoclave, offer optimal fiber arrangement and excellent in-plane mechanical properties. However, the manufacturing process for such components is complex and expensive. On the contrary, the out-of-autoclave manufacturing processes, such as LCM processes, typically utilize woven or braided fabrics, providing cost efficiency and ease of handling for large fabric sheets while enabling the production of complex-shaped parts. Among LCM techniques, vacuum-assisted resin transfer molding (VARTM) is particularly appealing due to its simplicity, low tooling cost, and ability to process large components [47]-[49]. In a typical VARTM setup (Fig. 2-3), dry fabric reinforcements are laid onto a rigid tool surface and covered with a sequence of auxiliary materials to facilitate resin flow, aid in demolding, and ensure surface finish quality. The entire assembly is then sealed with a vacuum bag, followed by vacuum application and leak testing. Once a full vacuum is achieved, liquid resin is introduced and drawn into the fiber preform under atmospheric pressure, resulting in complete impregnation of the laminate.

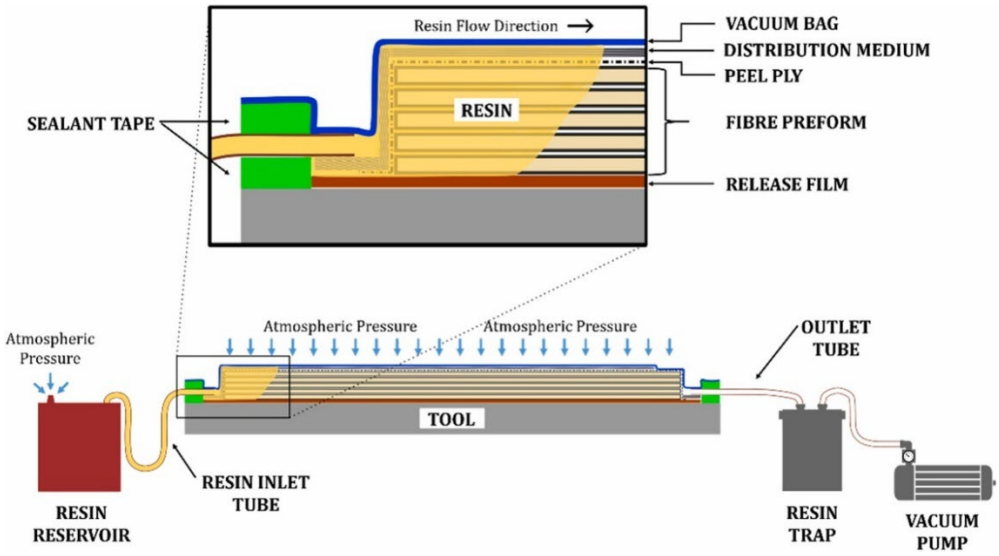


Fig. 2-3. Conventional VARTM process set-up [50].

2.2 Deformation Response and Damage Characteristics of FRP Composites Under Low Temperatures

Many studies have investigated the deformation response, fracture toughness, and damage and failure characteristics of composite materials subjected to quasi-static loading under ambient and low temperature conditions. In particular, research on conventional fiber-reinforced epoxy composites has

consistently reported an increase in longitudinal Young's modulus and tensile strength with decreasing temperature owing to the increased fiber-matrix interfacial strength and matrix strength at lower temperatures. Torabizadeh [51] identified a significant increase in the Young's modulus and longitudinal tensile strength in UD glass fiber/epoxy laminates with decreasing temperature from 20˚C to -60˚C, reporting strengths of 700MPa and 785MPa and modulus of 23.05GPa and 28.65GPa, respectively at each temperature (Fig. 2-4). A 13.5% reduction of strain at failure at -60˚C was also reported. Gong et al. [52] reported a >20% increase in the longitudinal tensile strength for unidirectional and cross-ply glass fiber/epoxy laminates tested at cryogenic temperatures (-196˚C). Similar findings were also reported for woven glass fiber/epoxy composites [53], [54]. Li et al. [55] comparatively assessed the tensile properties of unidirectional and cross-ply NCF glass fiber/epoxy composites at both room and cryogenic temperatures (-196˚C) and reported a significant increase of tensile strength (respectively, 68% and 38%) and modulus (respectively, 10% and 19%) at low temperature. Kim et al. [56] reported a 16% increase in the Young's modulus of UD carbon fiber/epoxy laminates with decreasing temperature from RT to -150˚C. However, the tensile strength of the material decreased by 9% at low temperature. Similarly, a 5% decrease in tensile strength was observed by Kumagai et al. [57] for a woven carbon fiber/epoxy composite tested at -196˚C. The reported reduction in the tensile strength for these materials at low temperature may be due to the internal thermal stresses caused during the cooldown process to RT after curing and subsequent further cooldown to the low ambient test temperature which may have induced localized matrix or fiber-matrix interface cracking. These contradictory results suggest that a more in-depth assessment of the complex damage mechanisms in these materials must be considered to better understand the influence of low ambient temperatures on their mechanical performance. In a recent study, fiber-reinforced epoxy-based composites have been shown to exhibit increased brittle failure modes and lower damage tolerance at low temperatures [14].

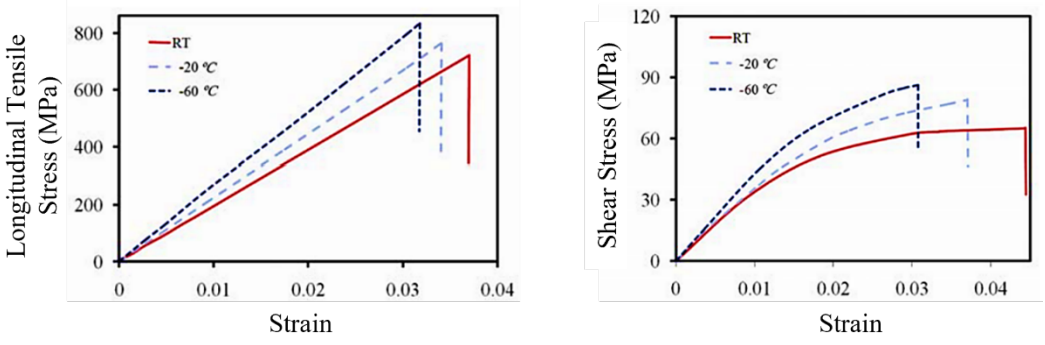


Fig. 2-4. Stress-strain curves of UD GF/epoxy composites at room and low temperatures [51].

Although studies focused on characterizing the behaviour of epoxy-based systems at low temperatures have been widely reported in the literature, similar studies focused on fiber-reinforced thermoplastic composites have also shown that the mechanical properties generally increase at lower temperatures [58], [59]. The combination of UD-NCF and reactive thermoplastic resin offer several key advantages when compared to their epoxy-based counterpart, such as the enhanced mechanical properties, improved environmental resistance, and the ability to be recycled [18]. In particular, the promising mechanical properties of reactive Elium® resins and their composites at room temperature have made them an ideal replacement for infusible epoxy resins [60], [61].Lorriot et al. [62] reported a comparable longitudinal tensile strength (~860MPa) and Young's modulus (~40GPa) in NCF glass fiber/reactive thermoplastic acrylic (Elium®) laminates compared to a similar epoxy-based material system; however, they observed a 5% increase in the strain at failure for the former material. Similar findings were reported by Cousins [63] where a 27% increase in the longitudinal tensile strength (916MPa) and a 10% increase in the Young's modulus (~41GPa) were reported for NCF glass fiber/Elium® laminates when compared to a NCF glass fiber/epoxy system. Obande et al. [48] characterized the transverse tensile properties for Elium®- and epoxy-based NCF glass fiber laminates and reported a 33% increase in the transverse tensile strength and a comparable modulus (13 GPa) for the NCF glass fiber/Elium® laminates (Fig. 2-5). They also reported a marked superiority in Mode-I interlaminar fracture toughness and delamination resistance for the NCF glass fiber/ Elium® system, with $G_{IC\text{-}initiation}$ and $G_{IC\text{-}propagation}$ values 19% and 15% higher than those of the epoxy-based system. Barbosa et al. [64] found that Elium® based woven carbon fiber composites exhibited 40% more resistance to Mode-II interlaminar fracture than their epoxy counterparts. Similar findings were reported by Bhudolia et al. [65] for different ultra-lightweight thermoplastic fabric/Elium® composites. They also characterized the damping, impact and flexural behavior for Elium®- and epoxy- based carbon fiber composites [66]. A higher structural damping (~22%), greater impact major damage energy (~19%), and less delamination (from flexural tests) were reported. The outcomes of these studies suggest that Elium®-based composites may exhibit superior fracture toughness and damage tolerance characteristics at low ambient temperatures when compared to their epoxy-based counterparts.

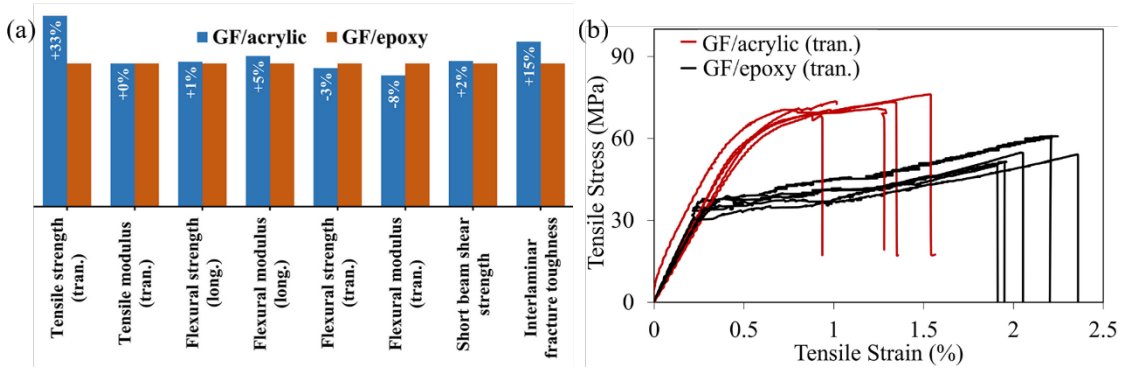


Fig. 2-5. Comparison of mechanical properties between glass fiber-reinforced thermoplastic acrylic and thermosetting epoxy laminates (a), and reference stress-strain curve under transverse tensile loading [48].

Despite several recent studies focused on characterizing fiber-reinforced/Elium® composites, there are few studies reported that focus on their mechanical performance under low ambient temperatures. Boissin et al. [67] reported a significant increase in ultimate tensile strength and elastic modulus for neat Elium® when the temperature decreased from 40°C to 15°C, 31.2% and 21.4% respectively, with a decrease of 52.2% in the ultimate strain. They also identified a comparable tensile property in cross-ply NCF and UD glass fiber/Elium® laminates due to the fiber-dominated mechanical behavior, with different microscale damage behavior where the early onset of damage and continuous fiber/matrix debonding were observed at 15°C. However, a higher shear strength and modulus were observed at 1°C compared to those at 48°C. Cadieu et al. [68] performed the quasi-static indentation tests on woven glass fiber/Elium® laminates from -20°C to 150°C and reported an increase in the maximum contact force, stiffness, elastic energy, and dissipated energy with the decreasing temperature, while the damage initiation depth remained comparable until 60°C where a significant increase of 50% was reported compared to 40°C, indicating a transition from brittle to ductile behavior.

Local damage mechanisms in FRP composites under quasi-static tensile loading typically include matrix cracking, fiber-matrix debonding, and individual fiber breakage. Matrix cracks commonly initiate in the resin-rich regions or within regions containing clusters of fibers due to stress concentrations. Fiber–matrix debonding at the interface can facilitate damage progression by reducing load transfer efficiency, often serving as a precursor to more extensive damage and ultimately contributing to fiber breakage [9]. Local matrix cracks in UD laminates often initiate in the off-axis plies. These cracks can coalesce with fiber-matrix debonds and lead to the formation of through-thickness ply cracks and, eventually, delamination between layers. The density and orientation of ply

cracks are strongly influenced by the layup sequence and the presence of manufacturing defects [9], [69]. For woven and braided composites, the interlaced fiber architecture alters damage initiation and propagation. Damage initiation often occurs within the resin-rich regions between the warp and weft yarns, followed by cracking at the yarn periphery. Through-thickness intra-yarn cracks also can form in the off-axis yarns. These damage mechanisms can lead to severe damage, including fiber fracture, ultimately leading to complete material failure [70]-[72]. The damage and failure characteristics of UD-NCF composites under ambient room temperature conditions have been the focus of few studies. Suratkar [73] investigated damage mechanisms in UD-NCF carbon fiber/epoxy composites under both quasi-static tensile and compressive loadings and correlated crack initiation with the stitching sites adjacent to fiber tows. These cracks subsequently developed into ply cracks, leading to delamination, which was identified as the most critical damage mechanism. Arwood et al. [74] examined the fracture surfaces of NCF glass fiber/ Elium® composites and its epoxy counterpart under compressive and shear loading (Fig. 2-6). They found that residual resin was visible along the entire length of the glass fiber for the thermoplastic composite, while resin split was present on the top of the fiber with the fiber's surface otherwise remaining bare for the epoxy composite. Similar observations were reported by Jespersen et al. [75]. Nevertheless, a comprehensive assessment focused on characterizing the effects of low temperature on damage and failure of NCF fiber-reinforced reactive thermoplastic composites is missing from the literature. Developing a comprehensive understanding of the damage and failure mechanisms of such material systems under low temperature is therefore crucial to ensure their widespread application.

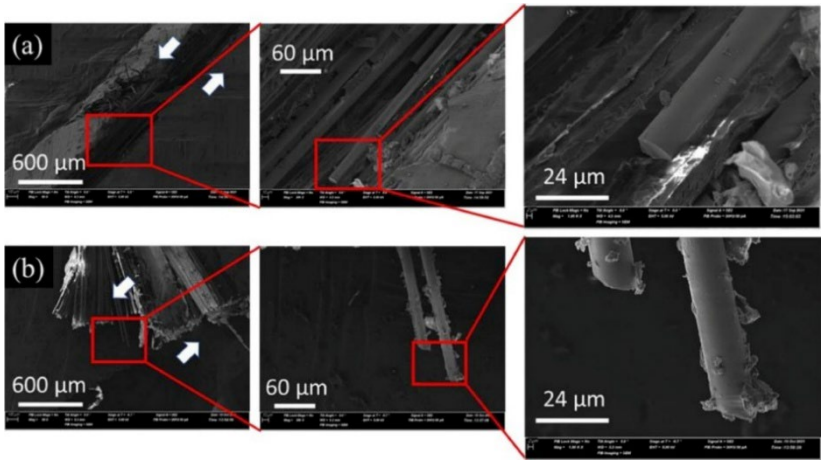


Fig. 2-6. Comparison of in-plane shear failure characteristics between glass fiber-reinforced thermoplastic acrylic (a) and thermosetting epoxy (b) laminates [74].

2.3 Fatigue Response and Damage Characteristics of FRP Composites

Material failure in service when subjected to repeated or cyclic loads of much lower magnitude than its fracture strength is known as fatigue failure. Fatigue has been a critical topic in materials research for over a century. There are numerous examples of structures that are subjected to cyclic loads, such as the varying aerodynamic, centrifugal and gravitational loading on wind turbine blades. In fact, fatigue loading plays an important role in service failures resulting from mechanical causes (fluctuating stresses or strains), particularly in FRP composite materials. Fatigue loading in terms of fluctuating stresses will be considered in this research. There are several main components of the applied load that can determine the extent of fatigue damage in FRP composites [76]: (i) the magnitude of the maximum applied stress that the material is subjected to, σ_{max}; (ii) the magnitude of the fluctuation in the applied stress, typically measured in terms of stress ratio R (= σ_{min} / σ_{max}); (iii) the magnitude of the loading frequency, f; (iv) the total number of repeated cycles, N. Environmental factors such as temperature and moisture can also influence the fatigue performance of FRP composites. A typical repeated stress cycle is defined by its stress amplitude (σ_a), stress range (σ_r), and mean stress (σ_{mean}), all of which contribute to fatigue behavior of FRP composites (Fig. 2-7a).

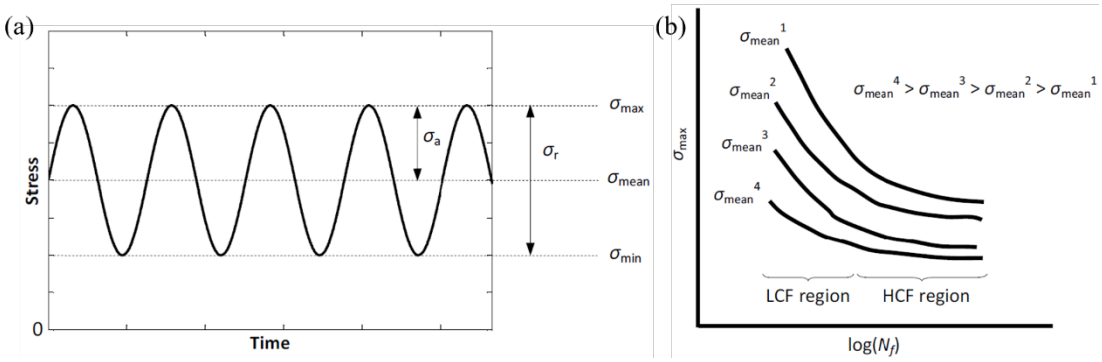


Fig. 2-7. (a) Ideal sinusoidal repeated stress cycle under tension-tension fatigue loading; (b) schematic of typical S-N curves for different applied mean stresses (b) [77].

The stress-life or S-N curve is a common approach to represent the fatigue behaviour of a material in terms of stress (typically σ_{max}) as a function of the number of cycles to failure (N_f). An S-N curve represented by an empirical linear, logarithmic, or power law can often adequately describe the relationship between σ_{max} and N_f for FRP composites [78]; Different values of mean stress significantly influence the fatigue life of FRP composites (Fig. 2-7b). An increase in mean stress generally reduces the number of cycles to failure for a given maximum stress. Additionally, the magnitude of the applied

stress plays a critical role in determining fatigue behavior. At higher stress levels, materials typically fail after fewer cycles, characterizing the low-cycle fatigue regime, which is associated with high strain and rapid damage accumulation. Conversely, lower cyclic stress levels result in a significantly higher number of cycles to failure, representing the high-cycle fatigue regime, where strains are small and damage accumulates gradually. Damage resulting from cyclic loading has a significant impact on the residual strength or stiffness of a composite component [8]. The presence and extent of various forms of damage, ranging from matrix cracking, fiber breakage, and fiber/matrix debonding to inter-laminar cracking (i.e., delamination), play a crucial role in determining the service life of a component, making it an important factor in assessing the damage tolerance of the structure. As a result, other mechanical parameters such as the residual strength ([79]-[82]) and residual stiffness ([42], [83]-[87]) have become indicators of fatigue damage development and criterion for fatigue failure prediction. While residual strength provides direct insight into load-bearing capability, it requires destructive testing and is therefore impractical for in-situ assessment. In contrast, residual stiffness can be measured non-destructively and therefore serves as a valuable indicator for continuously monitoring fatigue damage progression.

Several studies have investigated the fatigue behavior and damage characteristics in FRP laminates comprising UD plies [23], [88]-[95]. Castro et al. [91] studied fiber damage initiation and progression in UD glass fiber-epoxy composites $[0]_6$ under tension-tension fatigue loading with a stress ratio of R=0.05. They found that the fatigue damage initiated during the first cycle and no obvious stiffness degradation throughout the entire lifetime due to few fiber fragments. For multidirectional laminates comprising UD off-axis plies, damage evolution typically comprises the initiation and propagation of matrix cracks up to a saturation state, followed by the onset and growth of induced delamination cracks, and finally by breakage of the axial fibers leading to specimen failure [9]. Drvoderic et al. [88]conducted tension-tension fatigue tests (R=0.1) on off-axis glass/epoxy laminates with a stacking sequence of $[+\theta_3/-\theta_3]_s$ (θ=45º, 60º, 75º, and UD90º), and reported a correlation between off-axis matrix crack evolution and laminate stiffness degradation (Fig. 2-8). Li et al. [94] investigated the early damage accumulation of transverse cracks and delamination in CFRP cross-ply laminates under tension-tension fatigue loading (R=0.1). They reported that transverse cracks dominated damage development in thin $[0/90_2]_S$ laminates, while thicker laminates $[0_2/90_4]_S$ showed greater interaction between transverse cracks and delamination. Quaresimin et al. [92] studied damage initiation and evolution in multidirectional glass/epoxy laminates with layups of $[0/\theta_2/0/-\theta_2]_s$ (θ=50º or 60º) under

R=0.1 tension-tension fatigue loading. S-N data, damage initiation, crack density evolution, stiffness degradation, and Paris-like crack propagation data were extracted and found to be load dependent. They also conducted tension-compression and compression-compression fatigue tests with varying stress ratios (R=-1, -3, -5, -7, -10, and 20) on $[0_2/90_2]_s$ glass/epoxy laminates [93]. Different damage mechanisms were observed at different load ratio, i.e., transverse cracks for $R \geq -3$, inclined short cracks for R = 20, and mixed type of damage for $-10 \leq R \leq -5$. Moreover, the crack initiation and propagation were detrimentally affected by the compressive part of the cycle as a result of the larger residual crack opening displacement and the presence of diffused damage. The evolution of damage in woven and braided laminates under cyclic loading has also been extensively investigated, where crack development within the off-axis yarns has been reported as the main damage mechanism preceding localized inter-yarn cracking, delamination, and specimen failure [96]-[99].

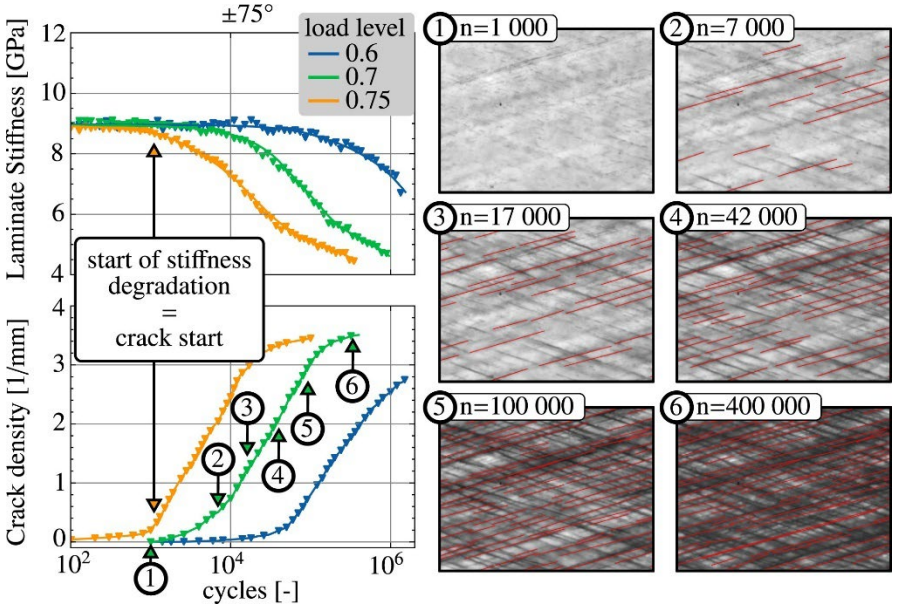


Fig. 2-8. Stiffness degradation and crack density evolution of $[+75^0_3/-75^0_3]_s$ laminate at different applied stress magnitudes [88].

In contrast, the damage evolution in NCF composites remains less understood due to their complex microstructures, including heterogeneous tow arrangements and stitching-induced distortions. Fewer studies have focused on characterizing the fatigue behavior of laminates comprising UD-NCF plies [42], [44], [75], [100], [101]-[105], despite their usage in several structural applications. Asp et al. [44] studied the effects of stitching pattern on tension-tension fatigue performance (R=0.1) in UD-NCF

composites and found that a high stitching density might lead to a shorter fatigue life. Similar results were reported by Vallons et al. [42] for UD-NCF GF-epoxy composites with different stitching patterns. Zangenberg et al. [100] investigated damage progression in UD-NCF glass fiber/polyester composites under tension-tension fatigue loading and found that damage initiated at the site of the supporting transverse fiber bundles (Fig. 2-9). This failure induced higher stresses within the adjacent axial load-bearing fibers, leading to fiber fractures and ultimately the catastrophic failure of the specimen. Jespersen et al. [75] further verified the damage process in UD-NCF composites by observing microcracks at the locations where the supporting transverse fiber bundles intersect with the main fiber tows, which subsequently propagated into the on-axis layers. In a later study by the same group [102], the damage progression scheme was modified for the early stages of cyclic loading where it was reported that some fiber fractures in the on-axis layers initiated simultaneously with off-axis cracks in the backing fiber bundles. Mattson et al. [103] investigated mechanical response and damage evolution in UD-NCF carbon fiber/epoxy cross-ply laminates under tensile loading. Laminates with a $[0°/90°/0°/90°]_s$ layup exhibited a significantly greater stiffness reduction (~40%) compared to the $[90°/0°/90°/0°]_s$ layup (~5%). This difference was attributed to combined damage mechanisms observed in the first layup, including transverse cracks in 90° bundles, extensive delamination between fiber bundles, and failure of 0° bundles. Recent studies [73], [104] have shown that UD-NCF composites exhibit a distinct deformation response and failure characteristics when compared to UD tape composites. Prajapati [105] examined fatigue damage evolution in UD-NCF glass fiber/epoxy composites and observed distinct damage features on the surface and within the bulk of the material. Surface defects, such as voids and micro-scale notches, led to matrix cracking, while in the bulk material clustered fiber breaks in the on-axis layers resulted in matrix cracks within resin-rich regions. The discrepancies between these findings warrant further investigation of the damage characteristics of UD-NCF composites subjected to cyclic loading. Therefore, it is essential to gain a comprehensive understanding of the damage mechanisms in NCF composites, which serves as a key focus of this research.

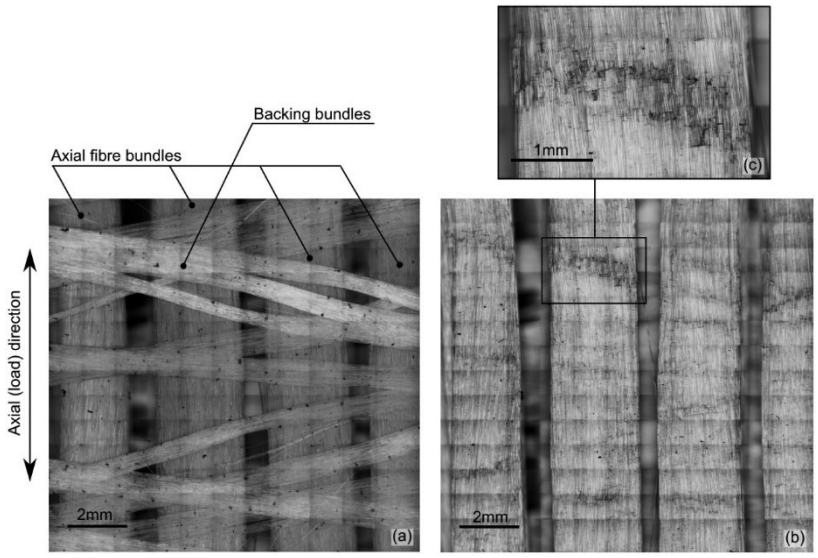


Fig. 2-9. Illustration of damage initiation beneath the supporting transverse fiber bundles [100].

2.4 Damage Monitoring Techniques

NDE involves utilizing a technique to detect and characterize surface and internal defects in a material or structure without causing any damage to the object under inspection [21]. A wide range of NDE techniques has been employed for monitoring damage in FRP composites [21], [22], [106], [107]. Visual inspection (VI) is often considered the initial step in the inspection process. Its effectiveness can be enhanced using dye penetrants, liquid penetrants, and magnetic particles [108]. Though simple, cost-effective, and little skill requirements, VI is limited to detecting visible and near-surface damage [21]. This limitation has prompted the adoption of more advanced NDE techniques capable of detecting complex types of damage in FRP composites, including acoustic emission (AE), ultrasonic testing (UT), X-ray radiography, X-ray computed tomography (CT), digital imaging correlation (DIC), infrared thermography (IR), and digital imaging (DI) techniques.

AE is a well-established in-situ NDE technique for FRP composite materials [109]-[111] and has been successfully employed to monitor fatigue damage development [112]-[115]. AE sensors, typically surface-mounted, detect acoustic waves emitted by microstructural events such as matrix cracks and fiber-matrix debonding. However, the sensitivity of AE sensors to ambient noise makes it challenging to accurately filter the acoustic signals, particularly under low-temperature conditions [21]. In addition, the wide range of acoustic intensity levels, which are distinct for different material systems, makes it challenging to reliably distinguish between different damage modes without substantial calibration.

UT, such as C-scan and A-scan, has been used in many fatigue studies to detect matrix crack and delamination in FRP composites [116]-[120]. While effective under controlled conditions, UT is limited by the poor resolution of the obtained images, high sensitivity to operational and environmental variations, and reduced reliability in low-temperature environment. These factors limit its broader adoption in in-situ fatigue damage monitoring.

X-ray radiography is also a valuable NDE technique for assessing damage in FRP composites at different length scales, such as matrix cracks, delamination, and fiber breakage. Many studies have employed X-ray radiography [121]-[125] for monitoring damage development under cyclic loading. However, traditional X-ray radiography relies on the liquid penetrant (such as iodine) reaching the damage cavities or the damage zone must be known in advance. Otherwise, the damage may go undetected as a result of the relatively close atomic numbers between fiber and matrix. The technique may also pose health risks due to exposure to hazardous contrast agents. In contrast, X-ray CT does not require use of a liquid penetrant, where instead a 3D rendering of internal structures of the specimen can be obtained simply by scanning [75], [126]-[128]. Small-scale in-situ test stages can be integrated into CT scanners to enable in-situ damage monitoring at intervals when the test is paused. However, the equipment is expensive, limited to small specimen sizes, and often unavailable in routine testing environments, and requires significant processing time for scanning and image reconstruction.

IRT is a non-contact technique that can be used to continuously monitor damage development in-situ in FRP composites. Several studies have successfully employed active and passive IRT techniques to monitor fatigue damage development [129]-[133]. IRT is a measurement technique that involves using an infrared (IR) camera to provide time-dependent contour maps of material surface temperature, resulting from energy release during damage initiation and propagation events. However, traditional IRT may not be able to detect fine-scale damage due to limited pixel resolution of the IR camera. While recent studies have utilized high resolution IR cameras to detect fiber-matrix debonding in composite laminates [134], [135], damage within internal layers may remain undetectable due to the low heat emissivity of damage or thermal resistance due to variations in thermal conductivity among different constituents. Additionally, the setup is susceptible to interference from the surrounding environment, which may further impact detection accuracy.

DIC is an in-situ NDE technique that has been used to detect real time damage in FRP composites. DIC enables the calculation of strain contours from specimen surface displacements, which can be correlated to damage events [136]-[140]. Li et al [141] employed DIC to study damage accumulation

(i.e., transverse cracks and delamination) in cross-ply carbon/epoxy laminates under tension-tension (T-T) cyclic loadings. Miskdjian et al [142] were able to use DIC to automatically measure crack density evolution in glass/epoxy laminates with different lay-ups under tensile quasi-static and T-T cyclic loadings. Pannier et al [143] and Foti et al [144] applied DIC to track surface damage evolution in carbon/polyimide woven composites under high temperature cyclic loadings. However, this technique is limited to detecting surface defects and its sensitivity reduces when distinguishing between different damage modes. Moreover, a complex setup was sometimes needed to fully characterize the damage where multiple cameras were employed to capture both the front and edge of the specimen [141],[142]. Nevertheless, DIC can be used to effectively capture stiffness degradation during cyclic loading from the calculated strains [141].

Digital imaging techniques, on the other hand, represent an easy, fast, cost-effective, and data rich NDE approach to detect damage in FRP composites with relatively translucent constituents, such as glass fiber-reinforced plastics [23]-[26], [88], [90], [93], [96], [145], [146]. Refer to Ref. [96] for use of digital imaging techniques to capture damage evolution in woven composites under T-T cyclic loadings, Ref. [88] for angle-ply UD laminates under T-T cyclic loadings, Refs. [145] for cross-ply laminates under T-T cyclic loading, and [93] for cross-ply laminates under tension-compression (T-C) and compression-compression (C-C) loadings. Moreover, digital imaging techniques are capable of integrating automated counting algorithms [24]-[26], [146] to detect off-axis tunnelling cracks at various loading conditions, in contrast to the manual and labor-intensive damage characterization process [8], [95], [97]. Glud et al. [25] developed an automated method for counting off-axis matrix cracks in UD glass fiber mats/epoxy laminates through three main operations comprising image compensation, Gabor filtering, and crack counting. Maragoni et al. [24] created an image analysis tool based on Gabor filters in Matlab® to detect off-axis cracks and quantify crack density in UD glass fiber/epoxy laminates. A similar tool was utilized by Lamon et al. [96] to detect cracks in the warp and weft fiber bundles of woven glass fabric/epoxy laminates. Bender et al. [146] refined the algorithm to enhance temporal accuracy in detecting crack initiation and propagation through motion compensation, background removal, segmentation, Gaussian filtering, image sharpening, thresholding, morphological closing, binarization, and crack counting. In addition to detect off-axis cracks, Carraro et al [23] and Maragoni et al [90] were able to automatically detect and quantify crack-induced delamination in glass/epoxy composites under T-T cyclic loadings. The advancement in computation capabilities and image processing algorithms has further accelerated the adoption of digital imaging techniques.

However, it is difficult to directly measure strain and track stiffness degradation while employing digital imaging techniques. In some studies, extensometers have been mounted on the specimens either above or below the damage monitoring region to track stiffness degradation during cyclic loading [23], [24], [92], [145]. An extended rectangular specimen geometry was used in these studies to ensure an appropriate distance from extensometer to the gripping areas. However, the measured strain may not represent the material deformation response due to high stress concentrations near the gripping region, where a measurement from the specimen gauge center is preferred [147]. Other studies performed separate tests to access damage states and evaluate stiffness degradation, which provided an indirect correlation between damage evolution and stiffness degradation [8], [100].

Although several different non-destructive testing techniques have been developed and used to monitor damage evolution in FRP laminates, these techniques have certain limitations (Table 2-1). Several techniques cannot be used to monitor damage in-situ, requiring removal of the specimen from the test frame and remounting which may introduce errors and impact the accuracy of the results. Several techniques are unable to directly visualize damage and rely on indirect measurements which require re-calibration for each material system for which they are applied, and they are sensitive to ambient conditions. While existing digital imaging techniques are suitable for in-situ damage monitoring of translucent FRP laminates, a direct correlation with the degradation of specimen stiffness during cyclic loading is challenging. Therefore, there is a compelling need for an integrated digital imaging technique that can simultaneously detect damage evolution and monitor stiffness degradation under fatigue loading.

Table 2-1. Summary of capabilities for selected NDE techniques.

NDE	In-situ	Damage detection				Low temperature application	Material limitation
		Matrix cracks	Debonding	Delamination	Fiber breakage		
AE	●	●	●	●	●		
UT		*	*	●			
X-ray		●	●	●	●		
IRT	●	●		●		**	
DIC	●	●				●	
DI	●	●		●	●	●	●

* Limited capability: difficult to correlate the signal to damage modes.

** Limited capability: need special calibration to the camera at the target temperature and require appropriate opening of the environmental chamber (or infrared window installed on the environmental chamber).

2.5 Deep Learning for Characterizing FRP Composites

Current crack counting algorithms are mainly based on Gabor or Gaussian filters [24]-[26], [96], [146]. In these methods, cracks detected from digital imaging are typically represented as straight line segments oriented in specific directions (i.e, along the fiber direction), and their count is determined by summing the distances between the start and end coordinates of each individual crack (Fig. 2-10). However, such approaches often overlook the texture and curvature of cracks, particularly in NCFs with diverse architectures (e.g., stitching patterns, fiber tow sizes, and the presence of supporting fiber bundles) where crack propagation along the fiber tow direction may deviate from a straight line [148]. Moreover, these algorithms tend to neglect crack interactions, including phenomena such as crack coalescence where cracks merge and extend along a straight plane across the width of the specimen, and crack offsetting where cracks initiated at different locations within the tow pass each other without merging [145]. Additionally, the accuracy of such methods often depends on extensive parameter tuning, including adjustments for crack direction, crack width, threshold values, and minimum crack size [146]. These limitations highlight the need for advanced and adaptive approaches. In particular, recent advancements in machine learning and computer vision offer significant potential to enhance the accuracy, robustness, and predictive capabilities of damage characterization in FRP composites.

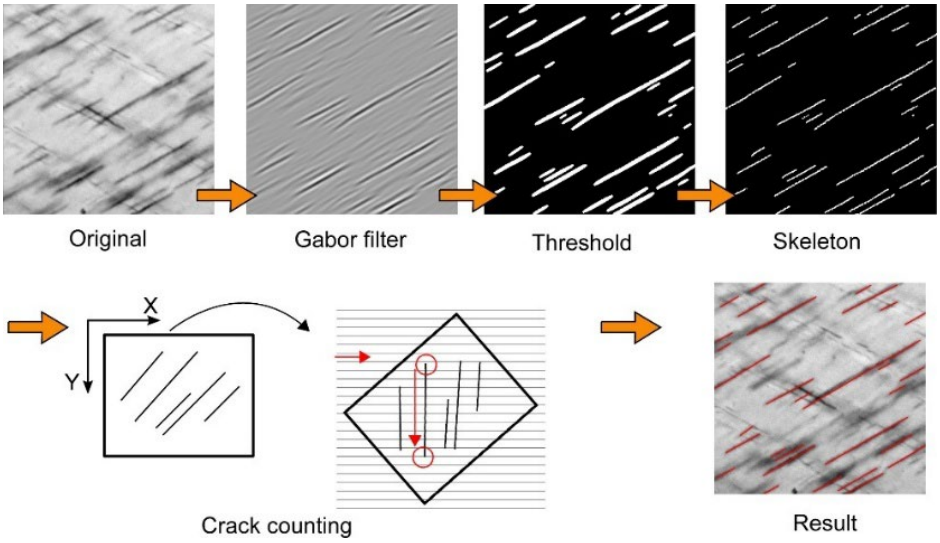


Fig. 2-10. Illustration of crack counting algorithm based on Gabor filter [26].

Convolutional neural networks (CNN) have been extensively applied to image classification tasks in recent years [149]-[152], including for microstructural assessment of FRP composites [152]-[160]. Traditional feature-based image processing approaches have been effective in improving performance in image identification tasks, such as support vector machines (SVM) [153], speeded up robust feature (SURF) [154], features from accelerated segment test (FAST) [155], and Hough transforms [156]. However, CNNs offer significant advantages over these conventional methods by automatically learning hierarchical features directly from raw image data, reducing the reliance on manual feature engineering, and achieving superior accuracy and generalization across complex datasets [157]. A typical CNN architecture comprises multiple convolutional layers to extract features such as edges and textures using filters and activation functions (Fig. 2-11a) [149]. These convolutional layers are typically followed by pooling layers to reduce spatial dimensions while preserving important features. The extracted features are then flattened and passed through fully connected layers to integrate information, with the final output layer generating class probabilities through a softmax or sigmoid activation function, depending on the task.

In tasks like medical image processing and composite damage characterization, the objective extends beyond classification to include precise localization, necessitating the need for assigning class labels to each pixel. The U-Net architecture, introduced by Ronneberger et al. [161], integrates a contracting (down-sampling) path to capture feature information and a symmetric expanding (up-sampling) path to enable precise localization (Fig. 2-11b). This design demonstrated superior performance in segmenting neuronal structures in electron microscopic stacks, achieving a Dice coefficient of 0.7756 on the DIC-HeLa dataset compared to 0.46 by other CNNs. Despite its success, studies applying U-Net architecture to composite materials are limited. Zhu et al. [162] utilized U-Net to classify cracks in the warp and weft yarns, resin-rich regions, and interface regions of 3-D woven carbon fiber/epoxy composites subjected to transverse impact tests, achieving over 88% segmentation accuracy. Oliveira et al. [163] employed a U-Net model to segment impact damage in optical lock-in thermography images of woven carbon fiber/epoxy composites. Dong et al. [164] utilized the U-Net architecture with Dice loss functions to characterize the microstructure of basalt and carbon fiber/poly(L-lactic acid) composites. They reported that models trained with a generalized Dice loss function outperformed those trained with compound loss and cross-entropy loss. However, many studies required small sample sizes in their experimental test setups [162], [165], or focused on simple classification tasks [163], [165]. Moreover, segmented classes were non-overlapping and the influence of key hyperparameters such as batch size,

class weights, and the number of epochs was often overlooked. Furthermore, no studies have combined U-Net architecture with automated crack counting algorithms to classify and count cracks, which are critical for developing damage mechanics modeling in FRP composites.

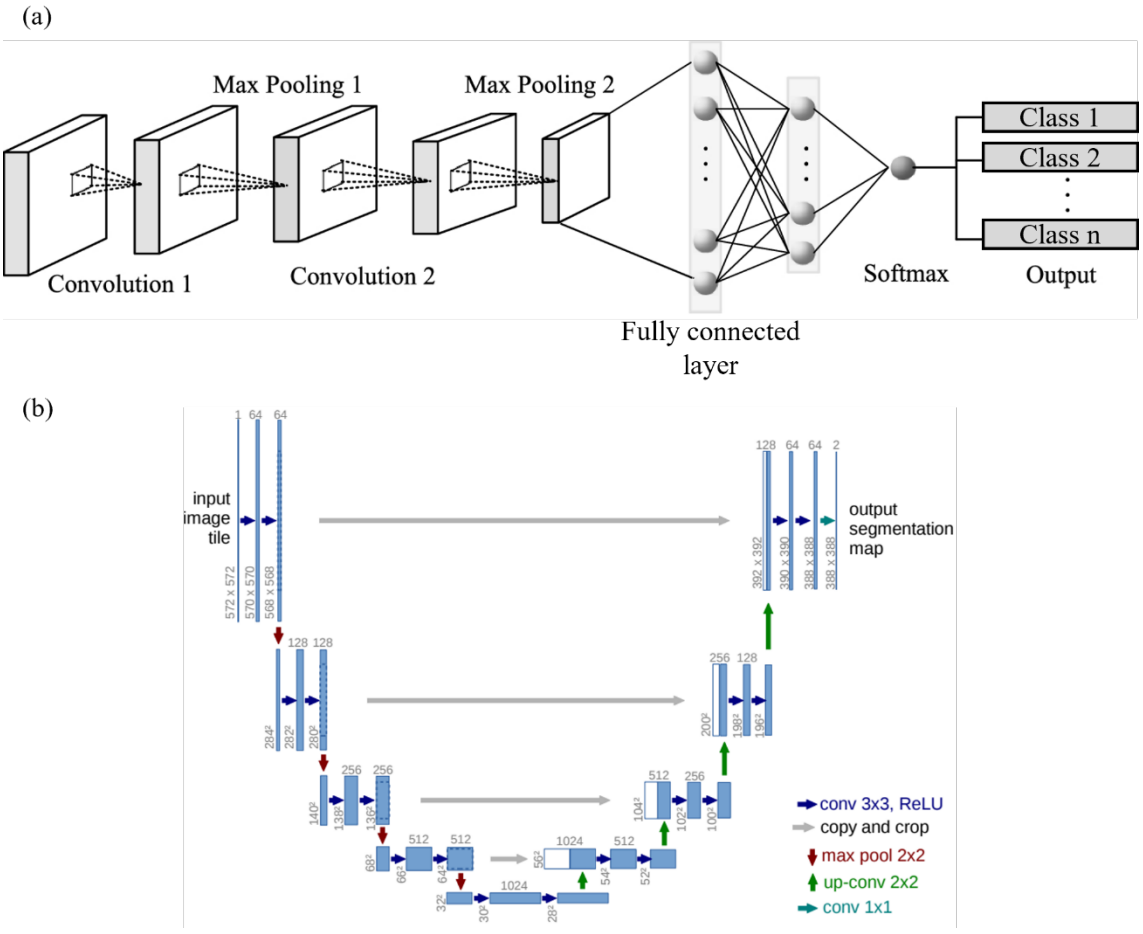


Fig. 2-11. Example of a typical CNN architecture (a) and U-Net architecture (b) [161].

Chapter 3
Research Objectives and Scope

3.1 Research Objectives

The overarching goal of this research is to develop an automated AI-driven non-destructive digital imaging technique for in-situ damage characterization of an infusible UD-NCF glass fiber-reinforced reactive thermoplastic composite material under various ambient temperatures and loading conditions. Stemming from the gaps identified in the literature review (Chapter 2), which are summarized in Table 3-1, the following are the objectives for the research that will contribute toward achieving the stated goal:

1. Assess the influence of low temperature on the deformation response and failure characteristics of the UD-NCF composite material to establish a deeper understanding of the underlying damage mechanisms.
2. Develop and validate an in-situ digital imaging technique to monitor the evolution of damage mechanisms in UD-NCF composite laminates subjected to quasi-static tensile loading.
3. Develop an integrated digital imaging technique to simultaneously monitor the evolution of damage mechanisms and stiffness degradation of UD-NCF composite laminates subjected to tension-tension cyclic loading.
4. Develop a deep learning-based CNN model for efficient and accurate qualitative and quantitative characterization of damage in the UD-NCF composite material.

Note that -50°C was selected for task 1 and task 2 to simulate extreme cold environments representative of service conditions in wind energy applications. Wind turbines are increasingly being deployed in remote or Arctic regions where operating temperatures can reach as low as –50 °C. This temperature represents a critical condition for evaluating the material's mechanical performance and for assessing the robustness and reliability of the proposed in-situ digital imaging technique.

Table 3-1. Objectives, gaps, and tasks for the research work.

Objectives	Gaps in the Literature	Tasks
1. Assess influence of low temperature on deformation response and failure characteristics	- Few studies have focused on characterizing the performance of FRP composites at low temperatures • Most studies do not assess damage evolution and failure mechanisms. • Limited studies focused on fiber-reinforced thermoplastics.	1.1. Develop protocols for manufacturing vacuum assisted infused panels. 1.2. Develop protocols for performing low temperature tests.

	• No studies focused on UD-NCF fiber-reinforced thermoplastic composites.	1.3. Perform tensile tests at RT and -50°C and fractographic assessment. Note: All tests involve a comparison between UD-NCF glass fiber reinforced composites comprising a thermoplastic acrylic and thermosetting epoxy matrices.
2. Develop digital imaging technique to monitor damage under quasi-static tensile loading	- Most established NDE techniques are not suitable for in-situ damage monitoring, are sensitive to noise and ambient conditions, or cannot resolve all damage mechanisms. - Limited studies have examined the effects of low temperature on the evolution of damage mechanisms and failure of NCF composite laminates. - Few studies have used digital imaging techniques for damage characterization glass fiber-reinforced composites at RT: • Most employ a single light source positioned behind the specimen; only a few use front-light illumination for enhanced light compensation and better damage detection. • No studies have applied digital imaging techniques for damage characterization at low temperature.	2.1. Develop protocols for in-situ non-destructive testing. 2.2. Perform quasi-static tests at RT and -50°C to qualitatively assess damage and capture modulus degradation. 2.3. Quantitative damage assessment.
3. Develop integrated digital imaging technique to monitor damage and stiffness degradation under tension-tension cyclic loading	- Few studies have focused on fatigue damage characterization in UD-NCF composite laminates. - Limited studies have employed digital imaging techniques for damage characterization under cyclic loading. - Simultaneously measuring strain and tracking stiffness degradation remains challenging: • Most studies mount extensometers above or below the damage monitoring region to track stiffness degradation. • Some studies use extended specimen geometries to ensure an appropriate distance between the extensometer and gripping areas. • Other studies conduct separate tests to assess damage states and evaluate stiffness degradation.	3.1. Develop an integrated digital imaging technique to simultaneously monitor damage evolution and stiffness degradation. 3.2. Verify the integrated digital imaging technique for fatigue testing. 3.3. Evaluate fatigue thresholds using infrared thermography. 3.4. Characterize damage evolution and stiffness degradation at varying maximum applied stress magnitudes.

4. Develop deep learning-based CNN model for damage characterization	- Few studies have employed crack counting algorithms for automatic detection and quantification of off-axis cracks. - Limitations of current crack counting algorithms: • Failed to consider the texture or actual crack propagation path. • Likely neglect crack interactions. • Require extensive fine-tuning to achieve accurate detection. - No studies have used CNN models to characterize damage in NCF composites - No studies have integrated crack counting algorithms with CNN models for automated damage characterization.	4.1. Establish a methodology for deep learning-based damage characterization. 4.2. Investigate the effect of batch sizes on characterization accuracy. 4.3. Investigate the effect of model weights on characterization results. 4.4. Analyze the effect of epochs on characterization accuracy. 4.5. Perform experimental validation using the entire dataset.

3.2 Scope of Work

The research work comprises four main tasks, each associated with an objective. The research workflow is shown in Fig. 3-1 and described hereafter.

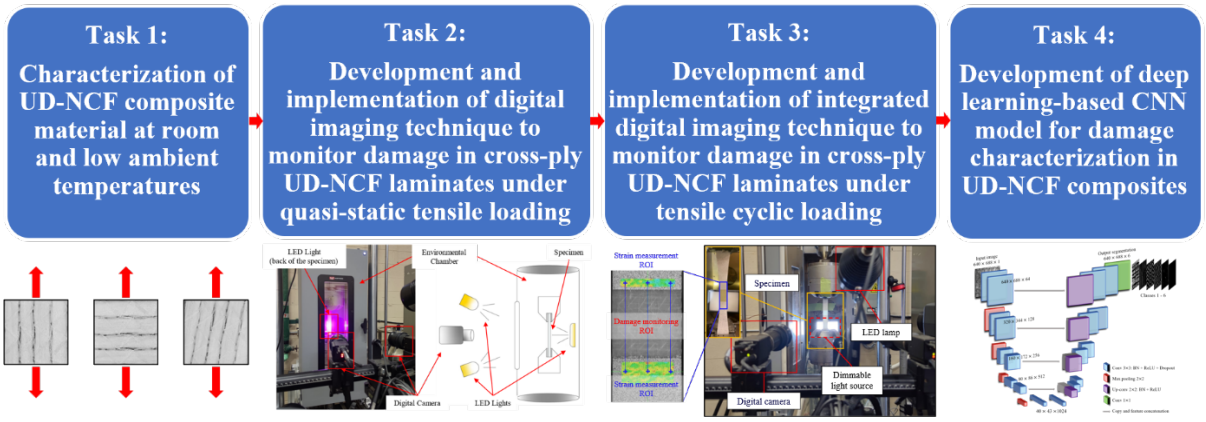


Fig. 3-1. Schematic showing the research plan.

3.2.1 Task 1 overview

Task 1.1 involves developing protocols for manufacturing UD-NCF glass fiber/thermoplastic acrylic composite panels using VARTM process. The in-situ polymerization behavior of thermoplastic resin during panel fabrication is investigated. Task 1.2 focuses on establishing low temperature mechanical testing setup under quasi-static longitudinal, transverse, and 10° off-axis tensile loading conditions.

Task 1.3 includes performing tests at RT and -50°C to evaluate tensile and in-plane shear properties. DIC and post-test optical microscopy are employed to evaluate the effect of temperature on damage evolution and failure mechanisms. All tests comprise comparative study using a UD-NCF glass fiber/epoxy composite counterpart.

3.2.2 Task 2 overview

Task 2.1 involves developing protocols for in-situ non-destructive testing of cross-ply UD-NCF glass fiber/thermoplastic acrylic composite laminates under quasi-static tensile loading at RT and –50°C. A digital imaging technique is developed and integrated into the test frame with cooling capacity. A custom algorithm is implemented to automatically detect crack initiation and growth in real time. Post-test optical microscopy and scanning electron microscope (SEM) are used to validate the developed digital imaging technique and confirm failure mechanisms.

Task 2.2 comprises quasi-static tensile testing of the same laminate at RT and -50°C. At least five tests are conducted at each temperature to qualitatively assess damage evolution and measure laminate modulus degradation. Damage evolution is analyzed using the developed digital imaging technique and validated through light microscopy, while failure characteristics are assessed via SEM. A detailed chronology of damage events is presented.

Task 2.3 focuses on quantitative assessment of damage evolution at both temperatures. Key damage metrics, including crack density, crack density rate during propagation, and crack length increase, are extracted from specimen surface images using an automated crack counting algorithm.

3.2.3 Task 3 overview

Task 3.1 involves developing an integrated digital imaging technique to simultaneously monitor damage evolution and stiffness degradation of cross-ply UD-NCF glass fiber/thermoplastic acrylic composite laminates under tension-tension fatigue loading. A suitable tension-tension cyclic loading profile is determined, followed by a thermographic approach to evaluate the fatigue threshold of the material. A synergistic data acquisition system is integrated with the test frame combining DIC for strain (stiffness) measurement, digital imaging technique for damage evolution, and an automate crack counting algorithm for comprehensive damage analysis.

Task 3.2 focuses on verifying the integrated digital imaging technique for fatigue testing. Preliminary fatigue tests are conducted to validate the accuracy of DIC strain measurements and the simultaneous

imaging of damage using the experimental setup described in Task 3.1. An automated crack counting algorithm is employed to track damage progression alongside strain measurements, while light microscopy is used to inspect specimen edge surfaces and validate observed damage modes.

Task 3.3 comprises the rapid evaluation of fatigue threshold using thermographic approach. An IR camera is synchronized with the test frame controller to measure surface temperature variations during stepwise cyclic tests in situ and in real time. For each specimen, the average surface temperature rises at stabilization for each maximum stress amplitude is plotted against the corresponding maximum stress level to determine the fatigue threshold.

Task 3.4 focuses on characterizing damage evolution and stiffness degradation under varying maximum applied stress magnitudes. Both quantitative and qualitative damage analysis are performed. Different damage modes are identified. Quantitative damage metrics, including crack density, crack propagation rate, and crack length increase, are evaluated to assess damage evolution. Light microscopy is employed at periodic intervals during testing to observe and validate damage states.

3.2.4 Task 4 overview

Task 4.1 involves developing a methodology for deep learning-based damage characterization. First, images from prior experimental work (Task 2) are preprocessed and annotated with six damage- and surface- related classes, which are then divided into training and testing sets. A CNN model is employed for damage characterization. An automated crack counting algorithm is integrated to quantify damage evolution.

Tasks 4.2, 4.3, and 4.4 focus on evaluating the effects of batch sizes, class weights, and epochs on characterization results. A total of four batch sizes and six class weights are evaluated, with periodic testing conducted at epoch intervals of 2 from 0 to 400 epochs. The optimal model is selected based on pertained weights and tuned hypermeters to ensure robust damage characterization.

Task 4.5 comprises experimental validation using the full image dataset obtained from quasi-static tensile and tension-tension fatigue tests (Task 2 and Task 3). These images serve as the input for the optimized model. Both qualitative and quantitative validations are conducted to compressively evaluate the capability of the model in damage classification and quantification.

Chapter 4

Synopsis of Research Methodology and Results

This chapter summarizes the results that were obtained from the tasks outlined in Chapter 3 to address the associated research objectives. First, an overview of the studied UD-NCF glass fiber/thermoplastic acrylic material system and the panel manufacturing process are presented. Next, a summary of the results obtained from characterization of the material at room and low ambient temperatures (Task 1) is provided. An overview of the developed digital imaging technique is presented, with application to in-situ damage characterization of the material under quasi-static tensile loading (Task 2). Thereafter, a summary of the integration of the developed technique with digital image correlation is described, with associated damage progression and stiffness degradation of the material under tension–tension cyclic loading (Task 3). Finally, the development, verification, and validation of a deep learning-based convolutional neural network (CNN) model for qualitative and quantitative damage characterization (Task 4) are presented. Details of the methodology and results for Tasks 1, 2, 3, and 4 can also be found in the papers listed in Appendices A to D, respectively, which are listed here:

Appendix A	E. Shi and J. Montesano, "Effect of low temperature on the mechanical properties and failure characteristics of an infused non-crimp fabric glass fiber-reinforced reactive thermoplastic," (Submitted to Composites Science and Technology_ Under Review)
Appendix B	E. Shi and J. Montesano, "Characterization of damage in non-crimp fabric glass fiber-reinforced reactive thermoplastic composites at low temperature using an in-situ digital imaging technique," Composites Part A: Applied Science and Manufacturing, vol. 190, p. 108674, Mar. 2025, doi: 10.1016/j.compositesa.2024.108674.
Appendix C	E. Shi and J. Montesano, "Integrated digital imaging technique for correlation of damage evolution and stiffness degradation in non-crimp fabric composite materials under cyclic loading," Composite Structures, vol. 371, p. 119513, Nov. 2025, doi: 10.1016/j.compstruct.2025.119513.
Appendix D	E. Shi, J. Montesano, Y. Zeng, and K. Rouf, "Deep Learning-Assisted Damage Characterization in Non-crimp Fabric Composites," (Submitted to Composites Science and Technology - Under Review)

4.1 Material System and Panel Manufacturing

4.1.1 Material system description

The material system under investigation in all Tasks comprised a reactive thermoplastic acrylic resin and a glass fiber UD-NCF reinforcement (NCF GF/acrylic). The resin system consisted of the methyl methacrylate (MMA) acrylic monomer Elium® 188 XO (Arkema Corp., France) and the benzoyl peroxide solution Luperox® AFR40 (Sigma-Aldrich, US) as the initiator. Elium® 188 XO was selected over other grades, such as Elium® 150 which offers enhanced mechanical properties, because it provides lower exothermic temperature during polymerization and a relatively longer open time, enabling the manufacture of large and thick composite components. These processing advantages made it particularly suitable for the present application. In-situ polymerization was enabled by mixing the monomer and initiator with a ratio of 100:2.5. The resin had a post-polymerization dry-Tg of 120°C, a low viscosity of 0.1 Pa·s, and a fast reactivity time of 60-90 minutes at room temperature (RT) [148], [166], which makes it compatible for use with resin infusion processes. The commercially available UD-NCF (Saertex Group, US) was composed of NEG 2026 E-glass fiber tows with a linear density of 2400 tex and width of 3.42 mm. The aligned longitudinal fiber tows were stitched together with warp knitted polyester yarns (110 dtex) in a tricot pattern (Fig. 4-1a). The transversely oriented supporting NEG 2026 glass fiber yarns (275 tex) served to maintain the integrity of the fabric throughout manufacturing (Fig. 4-1b). The total areal density of the fabric was 943 g/m^2.

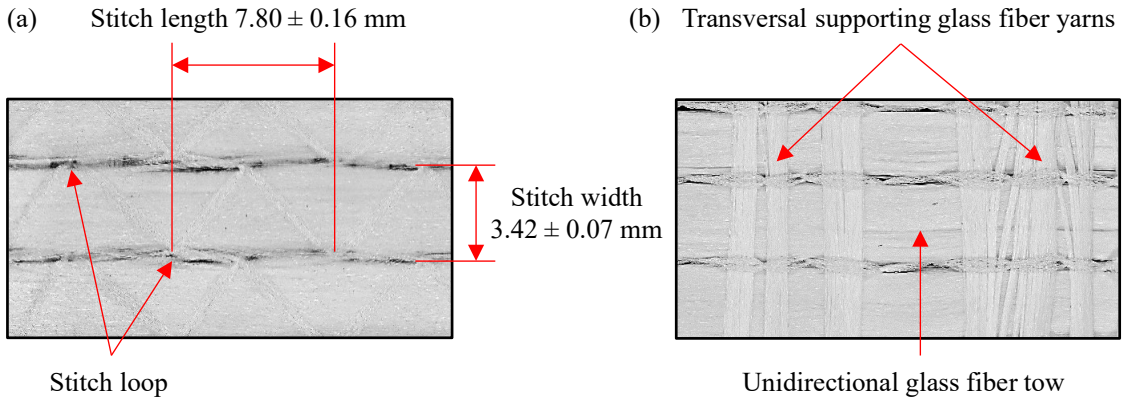


Fig. 4-1. Architecture of UD-NCF glass fiber reinforcement: (a) surface with tricot stitch pattern, and (b) opposite surface with transversal supporting glass fiber yarns.

4.1.2 VARTM process for panel manufacturing

A custom vacuum-assisted resin transfer molding (VARTM) process was developed and used to fabricate flat panels (Fig. 4-2). A 3.175 mm (1/8 inch) thick 6061 aluminum alloy plate used as the lower rigid mold was prepared using Frekote PMC cleaner and sealed with Frekote B-15 sealer, prior to applying several coats of the release agent Loctite® Frekote 770-NC (Henkel, Germany). In each processing cycle, four layers of the UD-NCF with a dimension of 305mm×305mm were cut from a roll and placed onto the mold, i.e., stacking sequence $[0_4]_s$ for Task 1 and $[0/90]_s$ for Tasks 2-4. A peel ply and distribution medium were then placed onto the fabric preform, before sealing the mold with a vacuum bag and sealant tape. Following the vacuum-assisted clamping and the evacuation of the air using a Leybold Trivac D30A vacuum pump (Leybold, Germany), a 25-min leak test was conducted under maximum vacuum pressure of 1000 mbar with the aim of achieving a uniform thickness and fiber volume fraction as well as mitigating voids in the fabricated panels [49]. Infusion of the resin and subsequent three-hour polymerization were performed under RT conditions. The panels remained in the mold for an additional 24 hours at RT prior to demolding. Further details of the VARTM process are found in Ref. [167]. The thickness of the manufactured NCF GF/acrylic panels was measured to be approximately 2.8 mm with an average ply thickness of 0.7 mm. The fiber volume fraction of the fabricated panels was determined by assessing cross-sectional images of the samples using optical microscopy and found to be approximately 46.2±1.2% [167].

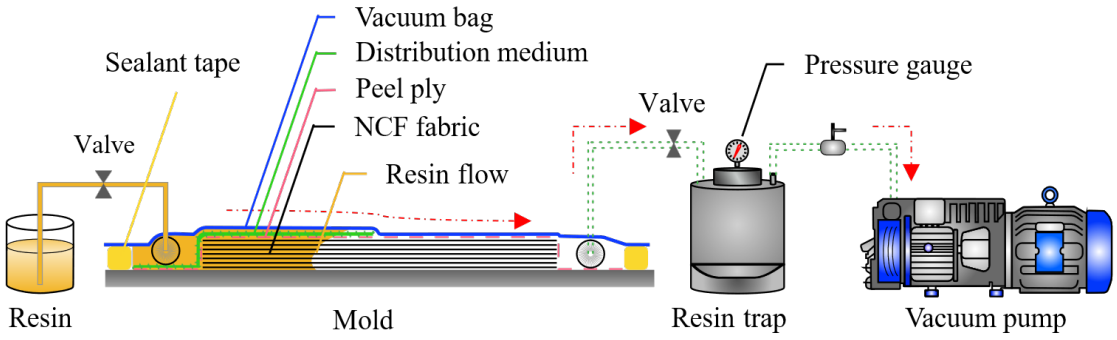


Fig. 4-2. Schematic of VARTM process setup used to fabricate flat panels.

4.1.3 In-situ polymerization behavior of resin during panel fabrication

A FLIR A8581 infrared (IR) camera with a pixel resolution of 1280 × 1024 and a temperature sensitivity of <25 mK was used to capture the temperature profile of the UD-NCF composite material during infusion and polymerization of fabricated panels with stacking sequence $[0/90]_s$. A region of interest (ROI) measuring 250 mm x 250 mm and centered on the panel was used for temperature data extraction (Fig. 4-3).

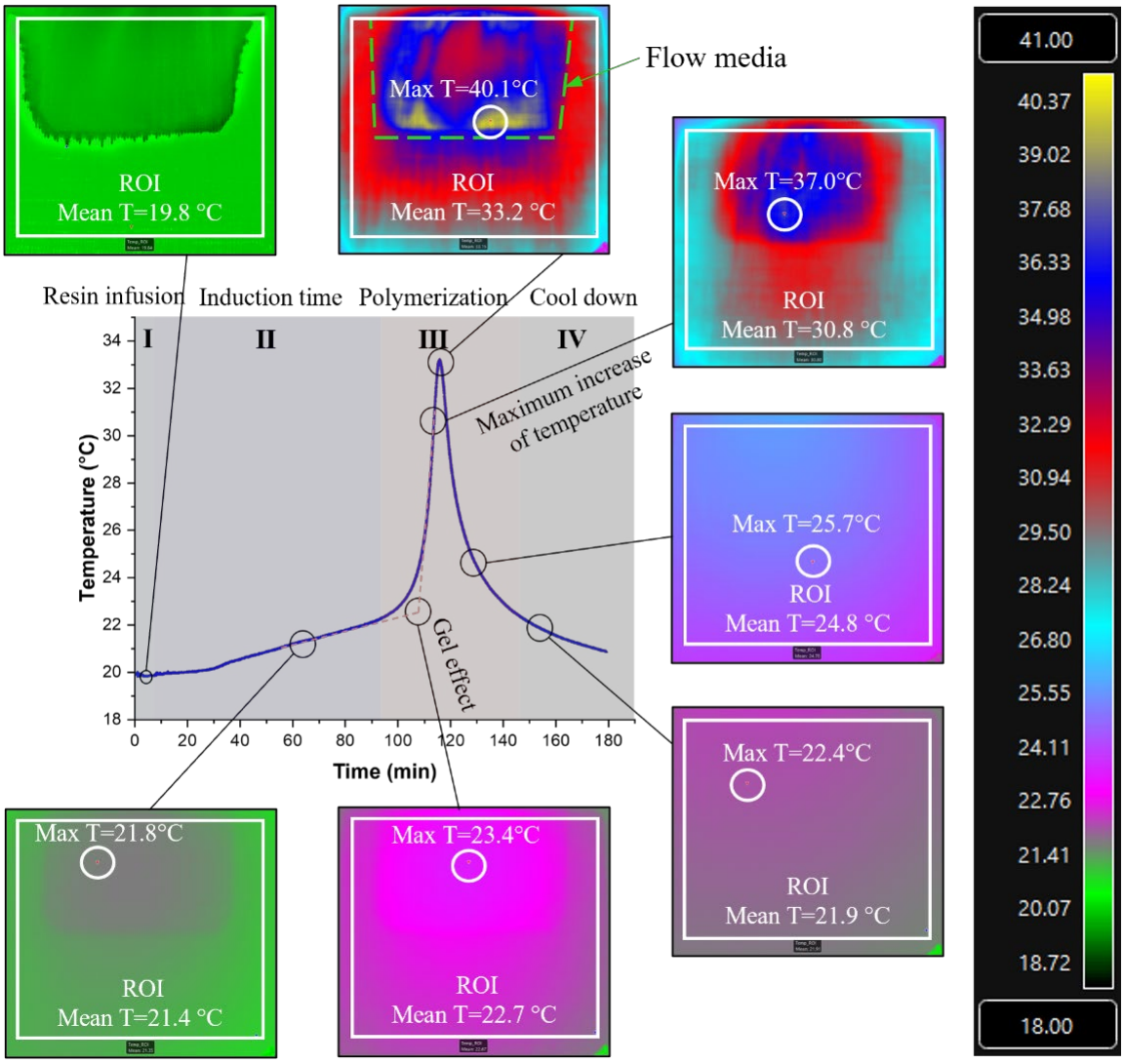


Fig. 4-3. Temperature profile and thermographs captured during resin infusion and polymerization of the UD-NCF composite panels at ambient temperature (phases I - IV of process are shown). Note, the size of the ROI indicated in the thermographs is 250 mm × 250 mm.

The overall polymerization process correlated well with that described in Ref. [168] and comprised an induction period of gradual temperature increase for 92 min (phase II), followed by a sudden temperature rise within 7 min up to a maximum temperature of 33.2°C, after which the temperature gradually decreased to the ambient temperature (phase IV). The polymerization reaction of the MMA monomer was initiated by the benzoyl peroxide, which generated free radicals during the polymerization process [166]. The temperature was uniform over the panel surface during the infusion process with $\Delta T < 1°C$ (phase I). During the induction time (phase II), the termination rate of the expanding macroradicals was controlled by the diffusion and orientation of the radical chain ends. Initially, the diluted solution allowed for the unimpeded movement of the entire macroradical through the solution (known as translational diffusion), leading to an evenly distributed temperature profile in the ROI with $\Delta T<1°C$ (i.e., from 10min to 90min during phase II). However, as the solution became more concentrated, translational diffusion started to impede the termination of macroradicals. At this point, the solution's temperature began to rise noticeably, but not rapidly, from 92min to 108min (beginning of phase III). After the two phases, there was a significant temperature increase from 22.7°C to 33.2°C within 7 min. The phenomenon in which the reaction kinetics undergoes self-acceleration (i.e., the gel effect) could be attributed to the entrapment of both the entire macroradical and its chain ends within the viscous and entangled solution, leading to a significant decrease of the termination rate. Consequently, there was a significant increase in the overall reaction rate and more heat was generated, which produced a nonuniform temperature distribution with $\Delta T \approx 10°C$ (peak of phase III). One can also see that the maximum temperature (40.1°C) occurred near the center region of the panel, correlating well with the contour plots of maximum increase of temperature. During the cool down process, little variation in surface temperature within the ROI was observed with <1°C temperature variation (end of phase III and phase IV).

It was evident from the evolution of the panel surface temperature that the duration of the polymerization process was approximately three hours. Beyond the three hours where polymerization occurred, the monitored temperature plateaued and showed no significant reduction for the remaining 24 hours of monitoring (not shown in Fig. 4-3). The fastest temperature rise (polymerization rate) occurred near the inlet hose beneath the flow media, with a slightly slower temperature rise moving out towards the panel edges. The non-uniformity of temperature across the panel during polymerization may be due to a larger exothermic temperature rise in the region beneath the flow media where the resin content is higher (see upper portion of thermographs in Fig. 4-3). Nevertheless, the temperature

variation across the panel surface was <7°C for the duration of the polymerization process, suggesting that the degree of polymerization was consistent across the panel despite the sharp exothermic temperature peak observed. Moreover, the temperature through the thickness of the relatively thin (2.8mm) manufactured panels was assumed to be uniform. In the paper by Han et al. [168], a coupled thermo-chemical process model was used to predict the temperature evolution and degree of polymerization (DoP) through the thickness of glass fiber/Elium® composite laminates manufactured at room temperature via infusion. The maximum through-thickness temperature variation for a 3.8mm thick laminate was reported to be ~3°C, while the maximum DoP of 0.958 was reported with the largest difference of ~0.01 along the through-thickness direction. To further assess the potential for variations in the degree of polymerization and mechanical properties in the manufactured panels, four samples with dimensions of 60 mm x 60mm were cut from two panels at different locations for dynamic mechanical analysis (see study by Rosso [169] for details). A consistent glass transition temperature of ~123°C was found, which agreed well with the reported value of 120°C (see Section 4.1.1), indicating that the resin across the panels fully polymerized. Also, the rectangular specimens used to perform RT and LT quasi-static tensile tests were cut from different locations on the manufactured panels (see Section 4.3.2 for results). Thus, the quality of the composite panels was deemed to be high owing to a low probability of residual stress and shape distortions during polymerization and solidification, as well as minimal void content or fiber distortions observed in the material.

4.2 Task 1: Characterization of UD-NCF Composite Material at Room and Low Ambient Temperatures

The mechanical performance and failure characteristics of the NCF GF/acrylic composite material were investigated and compared to a conventional epoxy-based counterpart (NCF GF/epoxy) at RT and -50°C. Quasi-static longitudinal, transverse, and 10° off-axis tensile tests were conducted on both materials to evaluate the tensile and in-plane shear properties. DIC and post-test optical microscopy were employed to evaluate damage mechanisms in the studied material systems. This task aimed to assess the influence of low temperature on the mechanical properties of the NCF GF/acrylic material and identify the underlying damage mechanisms, while also establishing the feasibility of the material for its intended application when compared to the NCF GF/epoxy material.

The NCF GF/epoxy material system consisted of the thermoset epoxy resin INF-114 (Pro-Set®, US) mixed with the amide hardener INF-211 (Pro-Set®, US) to a weight ratio of 100:27.4. The primary selection criterion for the epoxy resin was the comparability of the glass transition temperature (Tg) and viscosity with that of the acrylic resin (Table 4-1). Notably, both resins are compatible with resin infusion processes. The NCF GF/epoxy composite panels measuring 305 mm × 305 mm were fabricated using the same resin infusion process described in Section 4.1.2. A two-step curing process was implemented to ensure complete curing, beginning with 24 hours at room temperature followed by post-cure in a convective oven for 8 hours at 82°C prior to demolding. The panel thickness and fiber volume fraction for the NCF GF/epoxy panels were within 1% of the values for NCF GF/acrylic panels (Section 4.1.2).

Table 4-1. Comparison of mechanical, thermal, and physical properties of the matrix.

Properties	Elium® 188 XO [170]	Pro-set® INF-114/211 [171]
Tensile strength (MPa)	66	59
Tensile Modulus (GPa)	3.17	3.68
Elongation at break (%)	2.8	2.0
Glass transition temperature (°C)	107	102
Viscosity at room temperature (mPa.s)	100	296

4.2.1 Experimental details

Rectangular specimens were cut from the manufactured panels using an abrasive water jet cutting machine. Aluminum end tabs were bonded to the specimens to avoid potential gripping-induced failures at both RT and LT. Quasi-static longitudinal, transverse, and 10° off-axis tensile tests were conducted on UD specimens in displacement control using a servo-hydraulic MTS 810 test frame with a ±50 kN capacity load cell (see Table 4-2 for loading rate). Mechanical wedge grips were employed for all RT and LT tests. At each temperature condition, at least five repeated tests were performed to provide sufficient data for statistical purposes. The test parameters and specimen dimensions are summarized in Table 4-2.

Table 4-2. Test parameters for material characterization.

Type of test	Test standard/approach	Stacking sequence	Specimen dimension (L x W x T, mm)	Rate of testing (mm/min)
Longitudinal tension	ASTM D3039	$[0]_4$	275 x 15 x 2.8 (60mm end tab)	2
Transverse tension	ASTM D3039	$[90]_4$	275 x 25 x 2.8 (50mm end tab)	2
10° off-axis tension	NASA TN D-8215	$[10]_4$	200 x 15 x 2.8 (50mm end tab)	1

The 10° off-axis tensile test was selected to evaluate the in-plane shear properties of the material. This method is deemed to be a suitable method for evaluating intralaminar shear properties [172]-[174] compared to standardized ASTM testing such as V-notched beam and ±45° tensile tests [175], [176]. In this approach, specimens are loaded at an angle of 10° biased from fiber orientation, the material is subjected to a multiaxial stress state consisting of longitudinal tension, transverse tension, and in-plane shear stress components. However, the magnitude of the transverse tension stress is not notable for a biased angle of 10° (i.e., < 18% of the shear stress component) and the longitudinal tension stress has minor influence on the shear response. Thus, the shear response is driven by the in-plane shear stress component [172]. The 10° off-axis test was also chosen for its simplicity, as it can be performed using standard tensile fixtures without the need for specialized grips, and for its versatility, allowing application under various loading conditions such as high-rate testing and intralaminar fatigue testing [172].

For LT tests, an Instron E3119-609 environmental chamber with LN2 coolant was integrated with the test frame. Both mechanical grips and test specimens were subjected to the cooling environment to reduce thermal shock and ensure a uniform temperature along the specimen. Prior to performing the

LT tests, a dummy sample was used with two thermocouples glued on both sides of the sample surface to compare the temperature difference between the sample surfaces and the chamber during the cooling process. The chamber temperature was monitored by a control thermocouple positioned at the center of the back wall. The dummy sample was subjected to the cooling environment under load control to ensure no pre-damage was induced. Once the chamber temperature reached the target of -50°C, three additional minutes were needed for the sample to reach the same temperature. The temperature difference between the two thermocouples on the sample surfaces was less than 0.5 °C. Therefore, for the subsequent LT tests, the specimen was allowed to condition for at least five minutes after the target chamber temperature was reached to achieve thermal equilibrium before load was applied to the specimen.

3D DIC was used to monitor the displacement fields and detect potential out-of-plane bending for a subset of the test specimens using a GOM 3D 5MP system, which comprised two 5 MP cameras (Table 4-3). The ROI on the specimen surface, measuring 70 mm in length for the 10° off-axis specimens and 90 mm for longitudinal and transverse tension specimens, were finely speckled with black-on-white spray paint. GOM Aramis software was used to determine strain fields from images captured at a frequency of 3 fps. The average strain in the ROI (pixel size of 41.67 um/pixel) was determined using a subset size of 19 pixels, a step size of 6 pixels, and a strain filter of median.

Table 4-3. Specifications for the optical system.

Camera	Camera resolution	Lens	Exposure time	Frame rate
ARAMIS 5M	5M pixels	Titanar F2.8/50 mm	0.1ms up to 2s	3 Hz

4.2.2 Longitudinal tensile response and fractographic analysis

Both the NCF GF/acrylic and NCF GF/epoxy materials exhibited a near linear elastic stress-strain response with minor nonlinearity prior to failure at both ambient temperatures (Fig. 4-4a). The degree of non-linearity was minimal at the ambient temperature of -50°C, which is indicative of increased brittle failure. Load drops were observed prior to failure due to the non-simultaneous breakage of the 0° fiber clusters, with this phenomenon more evident at -50°C (Fig. 4-4a). The tensile strength increased by 8.12% and 8.95% for NCF GF/acrylic and NCF GF/epoxy respectively at -50°C compared to RT, while the temperature had little influence on the modulus and less influence on the strain at failure (Table 4-4, Fig. 4-4b, c, and d),. At -50°C, the polymer chain mobility for both acrylic and epoxy matrix were restricted, and the molecules were closely compacted. When combined with glass fiber, the

compressive stresses generated on the fiber-matrix interface by the contraction of the matrix and transverse glass fiber could increase the interface strength, leading to an increase in the tensile strength of the composite at low temperature. Moreover, the compressive stresses that developed along the longitudinal loading direction during temperature cooldown could also alleviate the tensile loads, and thus, increase the material strength. The magnitude of the Poisson ratios decreased with decreasing temperature for both materials (Table 4-4) as a result of the increased stiffness of the resin at -50°C, which would tend to have a greater influence on the transverse stiffness of the composite material. Moreover, there was no statistically significant difference between the mechanical properties of the NCF GF/acrylic and NCF GF/epoxy materials at the same temperature. These phenomena can be attributed to the fact that the longitudinal tensile properties are mainly dominated by the glass fibers.

Table 4-4. Average longitudinal tensile properties (± STV). Change in low temperature property determined with respect to the corresponding room temperature property.

Property	UD-NCF GF/acrylic		Change in property	UD-NCF GF/epoxy		Change in property
	RT	-50°C		RT	-50°C	
Tensile Strength X_t (MPa)	1032.88 (±34.33)	1116.71 (±45.25)	+8.12%	1048.37 (±53.29)	1142.20 (±45.14)	+8.95%
Tensile Modulus E_1 (GPa)	37.76 (±0.33)	38.89 (±1.21)	+3.01%	37.70 (±0.22)	38.38 (±0.63)	+1.80%
Strain at failure ε_{1f}(%)	3.18 (±0.22)	3.40 (±0.13)	+7.13%	3.16 (±0.24)	3.34 (±0.15)	+5.66%
In-plane major Poisson ratio, υ_{12}	0.229 (±0.003)	0.217 (±0.008)	-5.15%	0.239 (±0.002)	0.227 (±0.010)	-5.28%

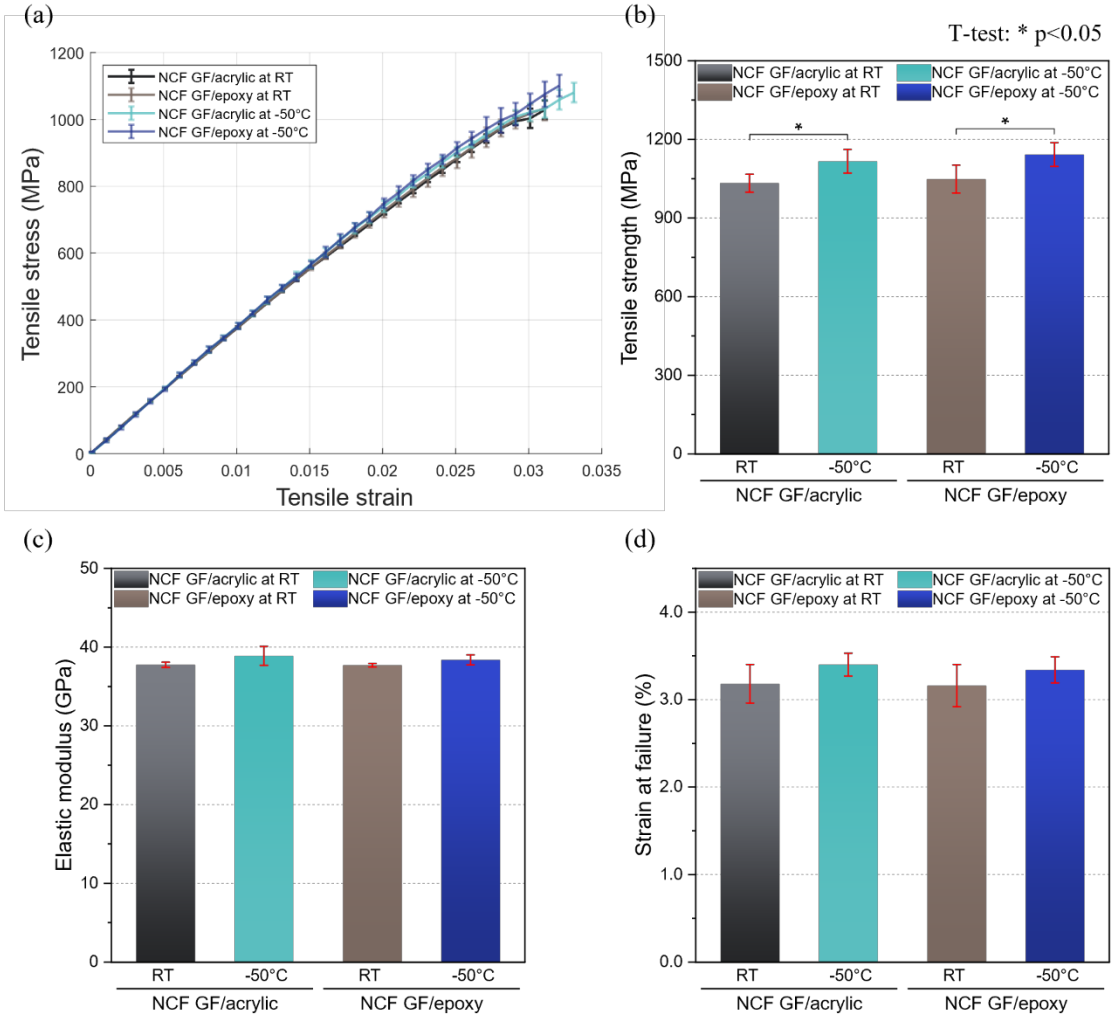


Fig. 4-4. Longitudinal tensile results at RT and -50°C: (a) average stress-strain curves with scatter bars shown; (b), (c), and (d) comparison of mechanical properties.

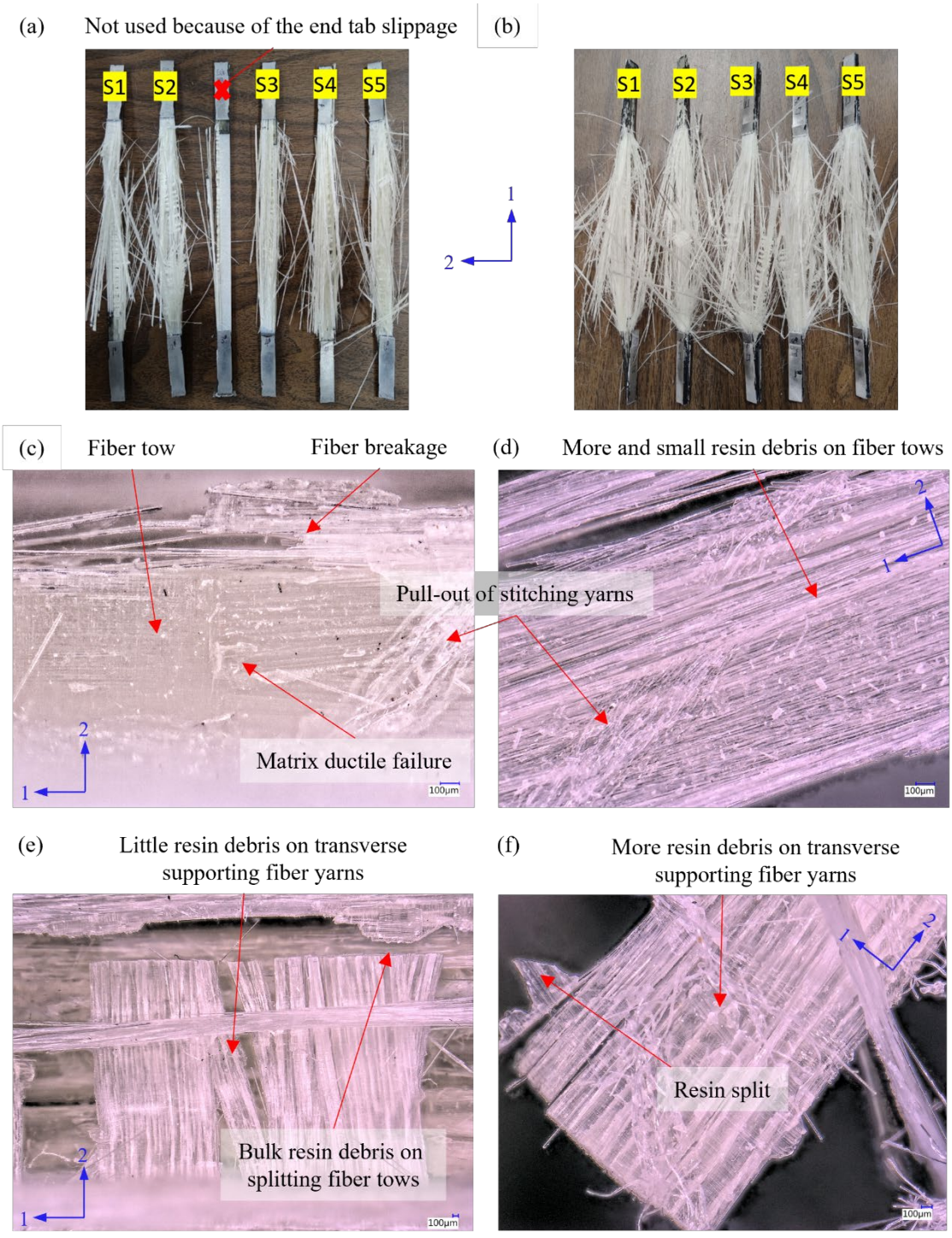


Fig. 4-5. Fractography of UD-NCF GF/acrylic subjected to longitudinal tensile loading at: (a), (c), and (e) RT; (b), (d), and (f) -50°C.

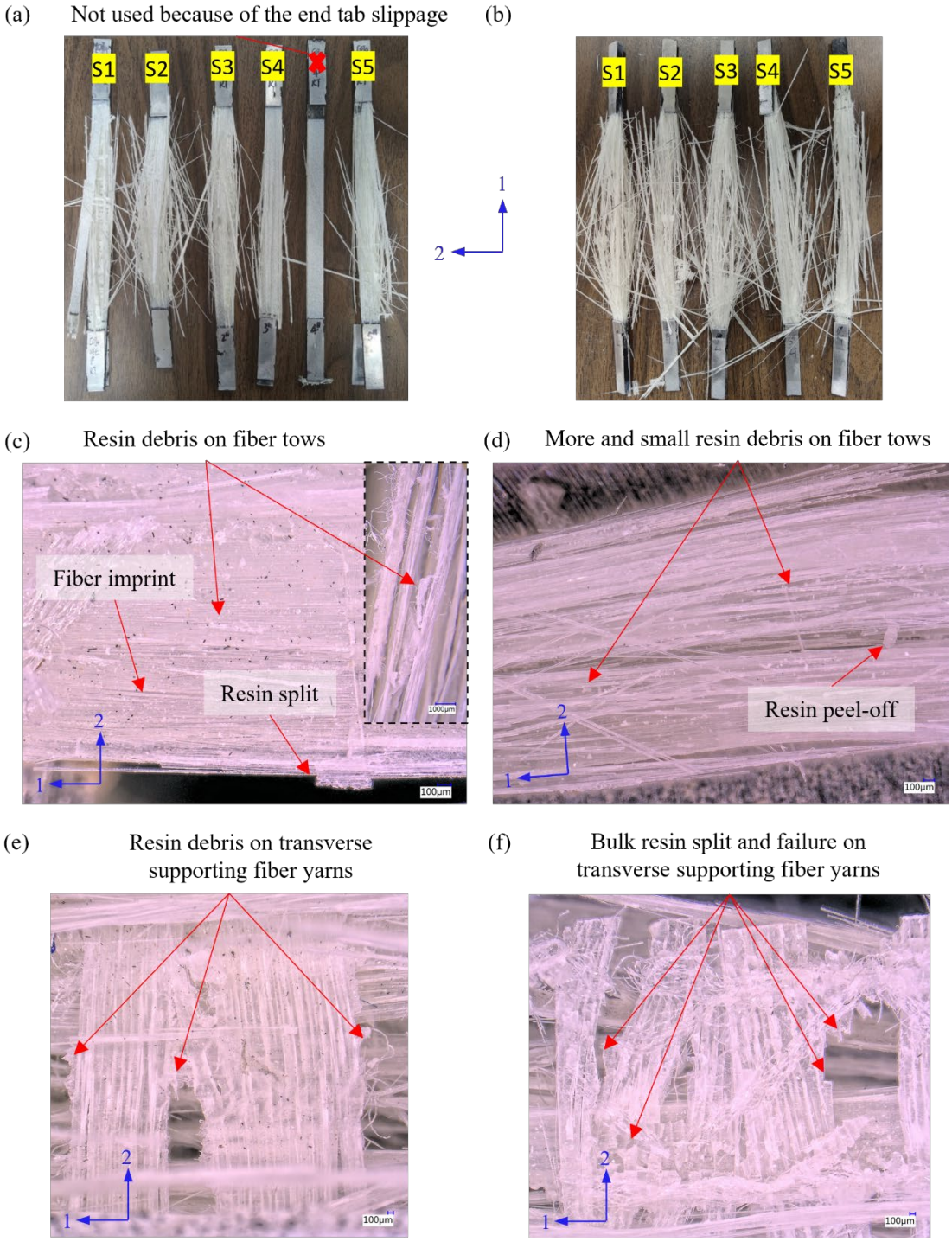


Fig. 4-6. Fractography of UD-NCF GF/epoxy subjected to longitudinal tensile loading at: (a), (c), and (e) RT; (b), (d), and (f) -50°C.

Examination of the fracture surfaces of NCF GF/acrylic and NCF GF/epoxy specimens at different temperatures (Fig. 4-5 and Fig. 4-6) showed that the fracture morphology is temperature dependent. For both materials, at RT the specimens ruptured and fiber tows split into bundles (Fig. 4-5a, Fig. 4-6a) in lieu of a smooth and flat fracture surface as reported by Yang et al. [177] for UD carbon fiber/BMI composites and by Li et al. [55] for multi-axial NCF glass fiber/epoxy composites. However, at -50°C the specimens severely ruptured into more slender fiber bundles (Fig. 4-5b, Fig. 4-6b). The interlayer adhesion improved significantly due to the residual compressive stresses caused by the temperature cooldown, which delayed breakage of the 0° fibers within different layers due to the constraining by the adjacent layers. As a result, more splitting cracks developed within fiber tows at -50°C and accumulated (i.e., tow crack multiplication) and then propagated along the tows (i.e., crack tunneling), resulting in more severe rupture behavior. The temperature-dependent fracture morphology under longitudinal tension loading is an important finding that has not been previously reported and may be characteristic of unidirectional NCF composites. Moreover, from the microscopic observations of fracture surface at different temperatures, one can see that for the NCF GF/acrylic, matrix ductile failure on fiber tows and bulk resin debris on splitting fibers were evident at RT (Fig. 4-5c and e), while resin split as well as more resin debris on fiber tows and transverse supporting fiber yarns could be observed for NCF GF/epoxy (Fig. 4-6c and e), indicating a brittle behavior when compared to NCF GF/acrylic. At -50°C, both acrylic and epoxy resin became more brittle compared to RT. As a result, resin split was observed (Fig. 4-5f and Fig. 4-6f), though more exaggerated for NCF GF/epoxy where bulk resin split and peel-off were evident (Fig. 4-6d and f). In addition, more and small resin debris were embedded on the fiber tows and transverse supporting fiber yarns of both materials, indicating the enhanced interface properties at -50°C, which can therefore improve the load bearing capacity.

4.2.3 Transverse tensile response and fractographic analysis

Both the NCF GF/acrylic and NCF GF/epoxy materials exhibited a similar nonlinear stress-strain response and mechanical properties at RT (Fig. 4-7), characterized by an inelastic threshold of approximately 40 MPa owing to micro-crack development. Obande et al. [48] performed transverse tension tests at RT on similar unidirectional NCF composite materials and found that the deformation response of the GF/acrylic and GF/epoxy materials were distinct (i.e., notably greater strength and inelastic threshold and lower strain at failure for the former material), which is in contrast to the results herein. Lorriot et al. [62] also performed RT transverse tests on similar materials and reported distinct deformation response with the GF/epoxy material exhibiting a higher strength and lower strain at

failure, which also contrast the results herein. At -50°C, however, both materials showed earlier onset of damage and exhibited a distinct bilinear stress-strain response with more pronounced scatter compared to the RT specimens owing to the accelerated accumulation of micro cracks (Fig. 4-7a). Moreover, both tensile strength and elastic modulus notably increased at -50°C, with a 23.21% and 35.26% increase for the NCF GF/acrylic, respectively, and a 25.01% and 29.00% increase for NCF GF/epoxy, respectively (Table 4-5, Fig. 4-7b and c). This result is expected because the material behavior along the direction transverse to the fibers is governed by the matrix and fiber-matrix interface properties, which increase with decreasing temperature. Furthermore, there was no statistically significant difference between the modulus of the NCF GF/acrylic and NCF GF/epoxy materials at the same temperature, while the strength of the latter material was slightly higher at each ambient temperature. Contrary to some previous studies [51], [177] the strain at failure increased at low temperature for both the NCF GF/acrylic and NCF GF/epoxy materials by approximately 48% and 53%, respectively (Fig. 4-7d), which is an important finding. The subsequent paragraphs center on the damage evolution and the macroscopic and microscopic examination of the fracture surface, with the aim of determining the underlying mechanisms responsible for the variation in the observed stress-strain behavior.

Table 4-5. Average transverse tensile properties (± STV). Change in low temperature property determined with respect to the corresponding room temperature property.

Property	UD-NCF GF/acrylic		Change in property	UD-NCF GF/epoxy		Change in property
	RT	-50°C		RT	-50°C	
Tensile Strength Y_t (MPa)	81.34 (±6.95)	100.21 (±3.22)	+23.21%	85.86 (±8.48)	107.33 (±6.94)	+25.01%
Tensile Modulus E_2 (GPa)	12.88 (±0.21)	17.43 (±0.69)	+35.26%	13.18 (±0.16)	17.01 (±0.78)	+29.00%
Strain at failure E_{2f} (%)	1.70 (±0.25)	2.52 (±0.35)	+48.25%	1.60 (±0.27)	2.44 (±0.17)	+52.63%

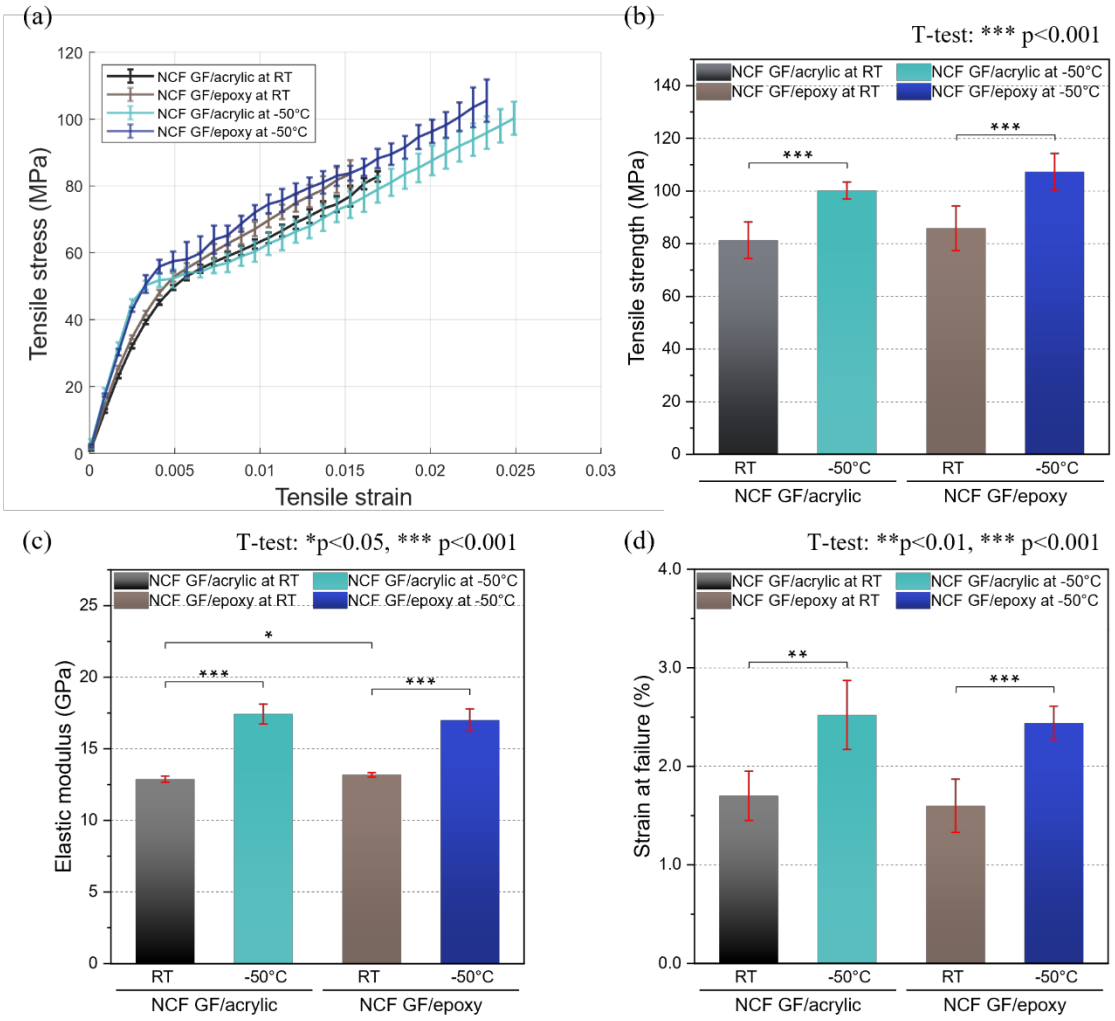


Fig. 4-7. Transverse tensile results at RT and -50°C: (a) average stress-strain curves with scatter bars shown; (b), (c), and (d) comparison of mechanical properties.

For both materials, the fracture surface was oriented perpendicular to the loading direction (Fig. 4-8, Fig. 4-9). Notable transverse cracks within the fiber tows were observed along the length of specimens tested at -50°C (Fig. 4-8c-d, Fig. 4-9c-d), while fewer cracks developed for specimens tested at RT (Fig. 4-8a-b, Fig. 4-9a-b). In case of the NCF GF/acrylic material, evidence of fiber splitting originated from the sparsely distributed transverse supporting fiber yarns and fiber bridging within the fiber tows were observed at RT (Fig. 4-8a). Fiber bridging was also reported in Ref. [48] for a similar GF/acrylic composite at RT. At -50°C, supporting fiber yarn pull-out and breakage as well as notable less fiber bridging were evident which is indicative of increased brittle failure (Fig. 4-8c). The role of the supporting fiber yarns on the failure behavior of the NCF GF/acrylic material at low temperature is an

important observation, which has not previously been reported. Pull-out of the supporting fiber yarns in combination with the increased fiber tow crack density may have contributed to the increase in the strain at failure of the composite material at low temperature. In case of the NCF GF/epoxy material, fracture occurred between the fiber tows and notable supporting fiber yarn pull-out and breakage was observed at both temperatures, though more exaggerated at -50°C where more slender supporting fiber yarn split and breakage were evident (Fig. 4-9a and c). Moreover, multi-fracture zones were observed at -50°C (Fig. 4-9c), indicating a brittle fracture behavior. The increase in the extent of supporting fiber yarn pull-out and increase in fiber tow crack density may have contributed to an increase in the failure strain at low temperature.

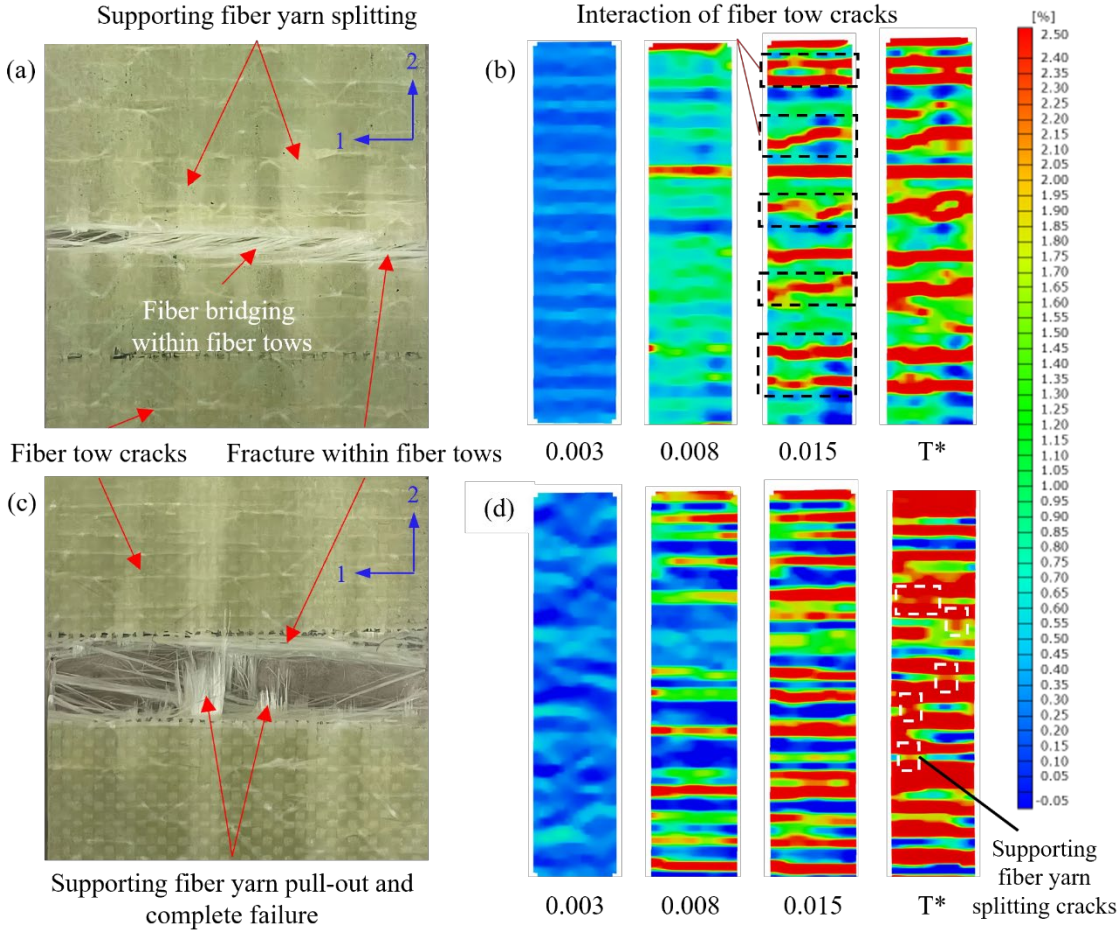


Fig. 4-8. Representative fracture surface and strain contours (revealing transverse cracks within fiber tows for indicated applied uniaxial strain) of UD-NCF GF/acrylic subjected to transverse tensile loading at: (a), (b) RT; (c), (d) -50°C (T*: frame prior to ultimate failure).

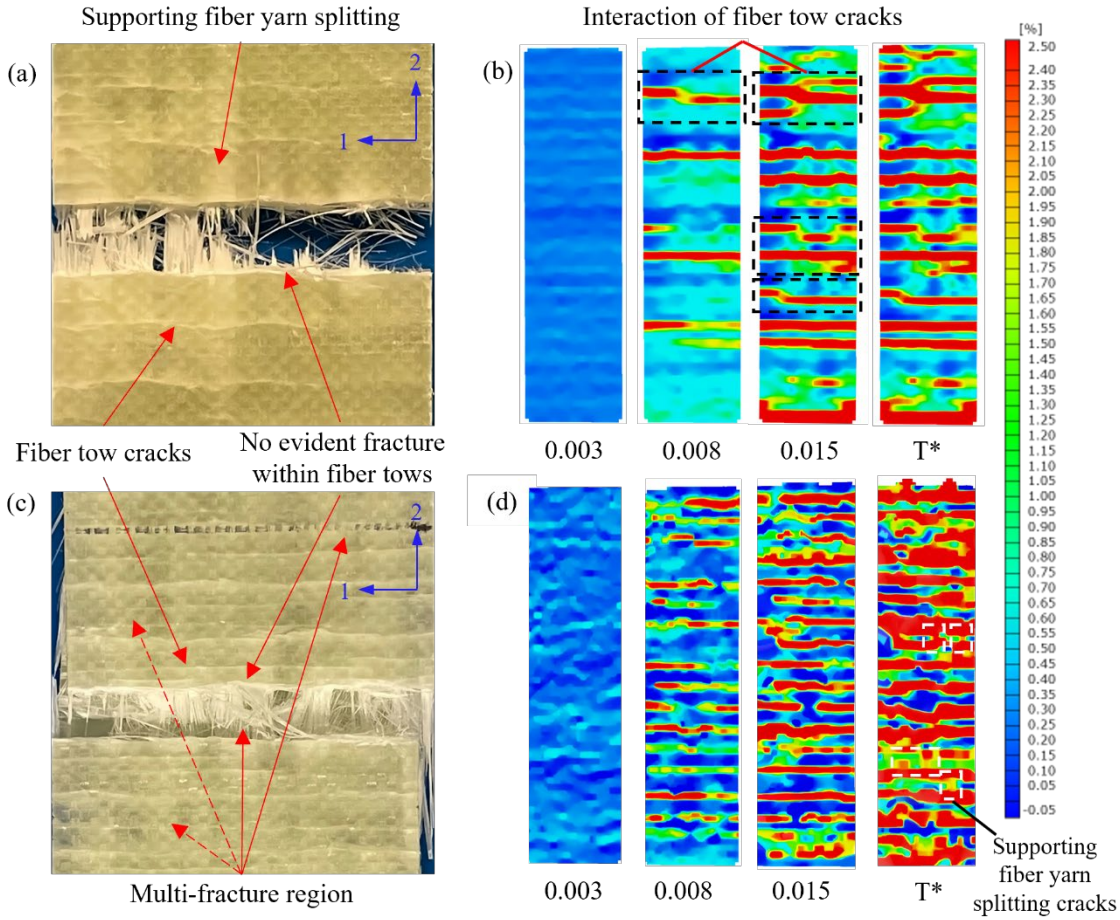


Fig. 4-9. Representative fracture surface and strain contours (revealing transverse cracks within fiber tows for indicated applied uniaxial strain) of UD-NCF GF/epoxy subjected to transverse tensile loading at: (a), (b) RT; (c), (d) -50°C (T*: frame prior to ultimate failure).

A series of time-lapse strain maps obtained from DIC are presented (Fig. 4-8b and d for NCF GF/acrylic and Fig. 4-9b and d for NCF GF/epoxy) in order to highlight the difference in strain development and thus damage evolution at both temperatures. For both materials, the strain maps confirmed that transverse cracks within the fiber tows developed at an earlier stage and with a greater density at -50°C, whereas transverse cracks were more evenly distributed for RT specimens. Moreover, the effects of low temperature on crack multiplication and evolution were highly evident: 1) cracks within fiber tows developed at multiple locations along the specimen length; 2) tow crack propagation (crack tunneling) was pronounced; 3) fewer interaction between the developed tow cracks were observed; 4) more supporting fiber yarn splitting cracks were observed. All these factors led to high

strain domains dominating the strain maps prior to failure, as can be seen from the time frame just before the final failure in Fig. 4-8d and Fig. 4-9d. However, at RT, the developed transverse cracks tended to interact with each other at earlier stages (i.e. strain=0.015 for NCF GF/acrylic and strain=0.008 for NCF GF/epoxy, Fig. 4-8b and Fig. 4-9b) and form more critical damage modes (i.e., delamination) leading to the final failure of the specimen at an earlier stage compared to those at -50°C. In addition, the contribution of supporting fiber yarns in load carrying and transfer was not significant at RT, while more evident at -50°C, a behavior not previously reported in the literature. This indicated the development of damage for both materials is also temperature dependent, though more exaggerated for NCF GF/epoxy.

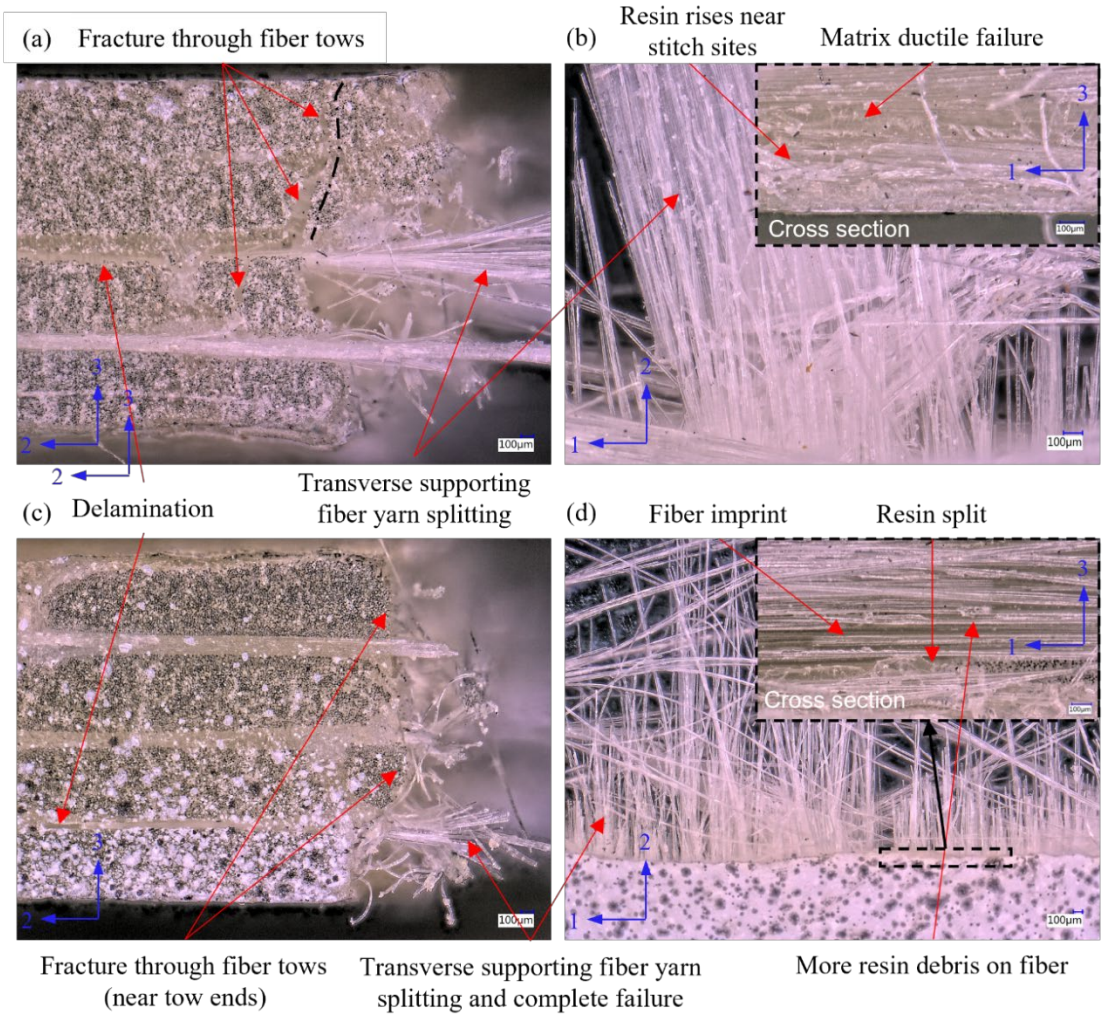


Fig. 4-10. Fractography of UD-NCF GF/acrylic subjected to transverse tensile loading at: (a) (b) RT; (c) (d) -50°C.

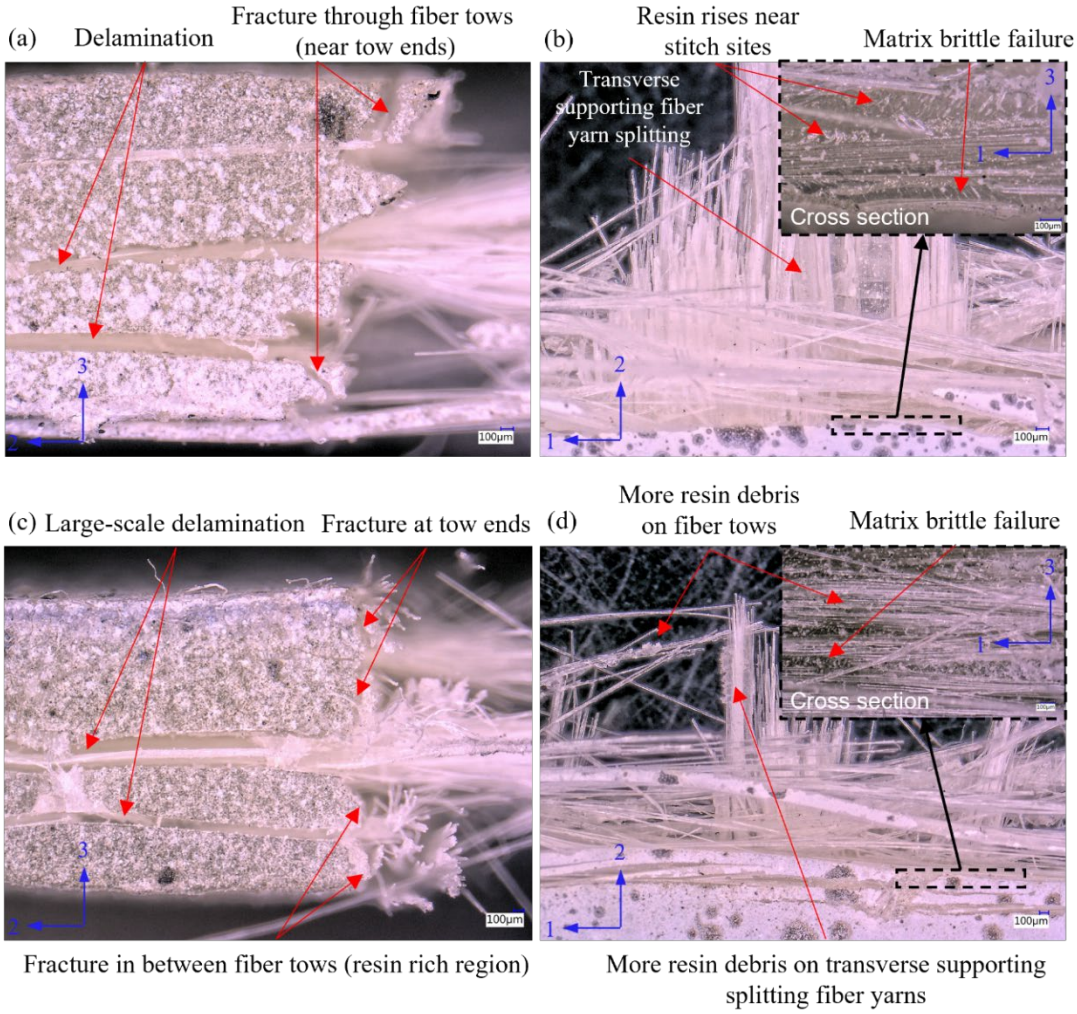


Fig. 4-11. Fractography of UD-NCF GF/epoxy subjected to transverse tensile loading at: (a) (b) RT; (c) (d) -50°C.

Fig. 4-10 shows the microscopic fractography of the UD-NCF GF/acrylic material subjected to transverse tensile loading at RT and -50°C. Fracture through fiber tows and delamination were observed at both temperatures, while the fracture plane was closer to the tow ends of fiber tows at -50°C (Fig. 4-10c). Moreover, crack coalesce and delamination between different plies were evident at RT (Fig. 4-10a), indicating the interactions among different damage modes, leading to an earlier failure event. Evidence of more slender and ruptured supporting fiber yarns and complete failure could be observed -50°C (Fig. 4-10d) compared to several bulk splitting supporting fiber bundles at RT, which further highlights the role of sparsely distributed supporting fiber yarns in load bearing and transferring at low

temperature. In addition, ductile matrix deformation and failure were evident at RT (Fig. 4-10b), while resin split and fiber imprint were observed at -50°C indicated a more brittle failure (Fig. 4-10d). More resin debris on fiber indicated the increased interface properties at -50°C. For the NCF GF/epoxy material, however, the damage was more exaggerated. Matrix brittle failure and severe delamination were observed at RT (Fig. 4-11a and b), while multi- and large-scale delamination and smaller cusps at -50°C indicated an increased brittle failure mode (Fig. 4-11c and d). Evidence of fracture in between fiber tows (resin rich regions) and more resin debris on both fiber tows and supporting fiber yarns at -50°C showed the enhanced interface properties at -50°C. It was observed that resin protruded near the stitch sites for both materials at RT due to stitching yarn pull-out (Fig. 4-10b and Fig. 4-11b), while the effect of stitches was not significant at low temperature. The above observations indicated that the failure behavior of NCF GF/acrylic under transverse tension is dominated by the fiber and matrix debonding at RT, though less evident at -50°C. However, for NCF GF/epoxy matrix failure between adjacent fiber tows was more evident at -50°C.

4.2.4 In-plane shear response and fractographic analysis

At RT, both materials exhibited a similar shear stress-strain response characterized by an initial linear region followed by notable nonlinearity with a pronounced stress plateau preceding failure (Fig. 4-12a). The degree of nonlinearity, and hence the strain at failure, was notably higher for the NCF GF/acrylic material due to the local plastic deformation of the thermoplastic resin. At -50°C, however, the stiffness of the resin increased, leading to a markedly less nonlinearity in the shear stress-strain response for both materials. As a result, the strain at failure at low temperature decreased by 84.54% and 62.93% for the NCF GF/acrylic and NCF GF/epoxy, respectively (Table 4-6, Fig. 4-12d), revealing that the former is more sensitive to low ambient temperature. Torabizadeh [51] reported similar influence of low temperature on the strain at failure of a unidirectional GF/epoxy tape composite material subjected to in-plane shear loading. This behaviour is markedly different than that observed for transverse tension where the strain at failure increased at low ambient temperature, which may be due in part to the reduced contribution of the supporting fiber yarns in carrying the load. Moreover, both shear strength and modulus increased significantly at -50°C, respectively by 23.74% and 50.74% for the NCF GF/acrylic material and 44.84% and 34.86% for the NCF GF/epoxy material (Table 4-6, Fig. 4-12b and c), due to the increased modulus of the matrix and increased fiber-matrix interfacial strength with the decreasing temperature.

Table 4-6. Average in-plane shear properties (± STV). Change in low temperature property determined with respect to the corresponding room temperature property.

Property	UD-NCF GF/acrylic RT	UD-NCF GF/acrylic -50°C	Change in property	UD-NCF GF/epoxy RT	UD-NCF GF/epoxy -50°C	Change in property
Shear Strength S_L (MPa)	46.41 (±1.50)	57.42 (±2.63)	+23.74%	45.37 (±0.31)	65.71 (±2.28)	+44.84%
Shear Modulus G_{12} (GPa)	6.00 (±0.10)	9.05 (±0.82)	+50.74%	6.05 (±0.19)	8.17 (±0.34)	+34.86%
Strain at failure γ_{12f} (%)	5.79 (±0.60)	0.90 (±0.14)	-84.54%	3.98 (±0.44)	1.48 (±0.15)	-62.93%

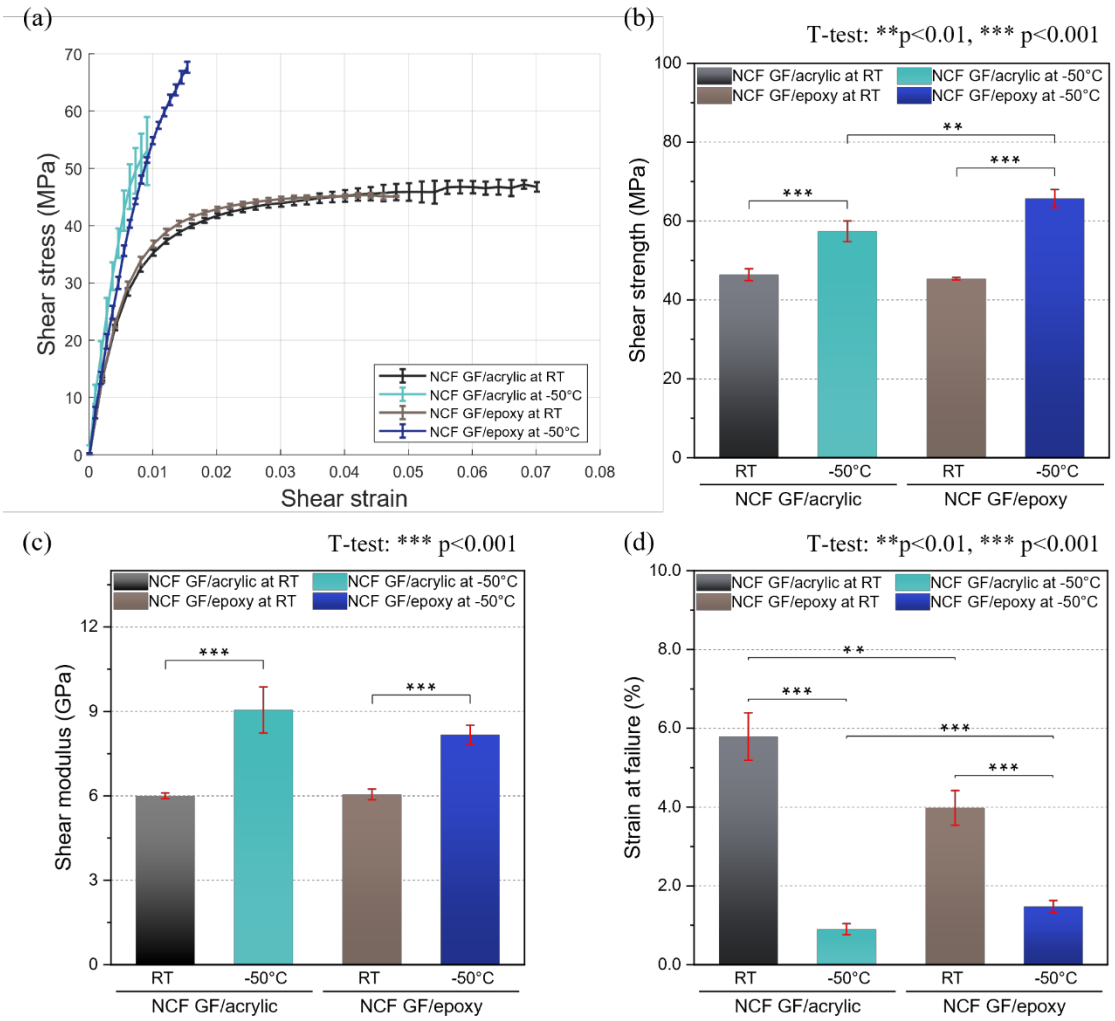


Fig. 4-12. In-plane shear results at RT and -50°C: (a) average stress-strain curves with scatter bars shown; (b), (c), and (d) comparison of mechanical properties.

Macroscopic fractographies reveal that facture occurs along the fiber tows with the plane oriented at a 10° bias for both materials (Fig. 4-13a and b and Fig. 4-14a and b). For the NCF GF/acrylic material at RT, localized delamination in the region adjacent to the fracture plane and a rough fracture surface was observed owing to localized fiber tow reorientation (Fig. 4-13a). At -50°C, notable delamination near the fracture plane was observed as a result of interactions between fiber tows and splitting cracks within the supporting fiber yarn (Fig. 4-13b). Microscopic analysis of RT samples (Fig. 4-13c and e) showed resin shear cusps and a rough fracture plane with localized fiber reorientation due to the ductility of the matrix . This result could help explain the comparable shear strength and increased strain at failure at RT when compared to the NCF GF/epoxy material. At -50°C, however, the fracture plane was smooth with no obvious fiber reorientation (Fig. 4-13d). A closer view from the specimen edge revealed both resin split and bulk resin peel off (Fig. 4-13f), indicating a change of failure behavior from ductile to brittle at -50°C. For the NCF GF/epoxy material, delamination was observed along the fracture plane and splitting of the supporting fiber yarns at both temperatures, while several fiber tow cracks and more exaggerated delamination were evident at -50°C (Fig. 4-14c-f). In addition, microscopic results showed the smooth fracture plane with no fiber tow reorientation at both temperatures due to the brittle thermoset resin behavior (Fig. 4-14c and d). However, local reorientation and breakage of supporting fiber yarns near the fracture surface indicated the supporting fiber yarns did play a role in carrying load and enabling larger strains. This could also help explain the observed higher strength and strain at failure at -50°C compared to NCF GF/acrylic. Evidence of smaller resin debris on fibers and more resin embedded on fibers also demonstrated the enhanced interface properties at -50°C (Fig. 4-14c-f). The above observations indicated that the shear properties of NCF GF/acrylic and NCF GF/epoxy were primarily dominated by the matrix behavior (i.e., shear modulus, shear strain at failure) and the enhanced interface properties at -50°C contributed to the increased shear strength. Moreover, the role of supporting fiber yarns in load carrying was more evident for NCF GF/epoxy, while it contributed to notable delamination in GF/acrylic at -50°C as a result of the interactions between the developed damage modes.

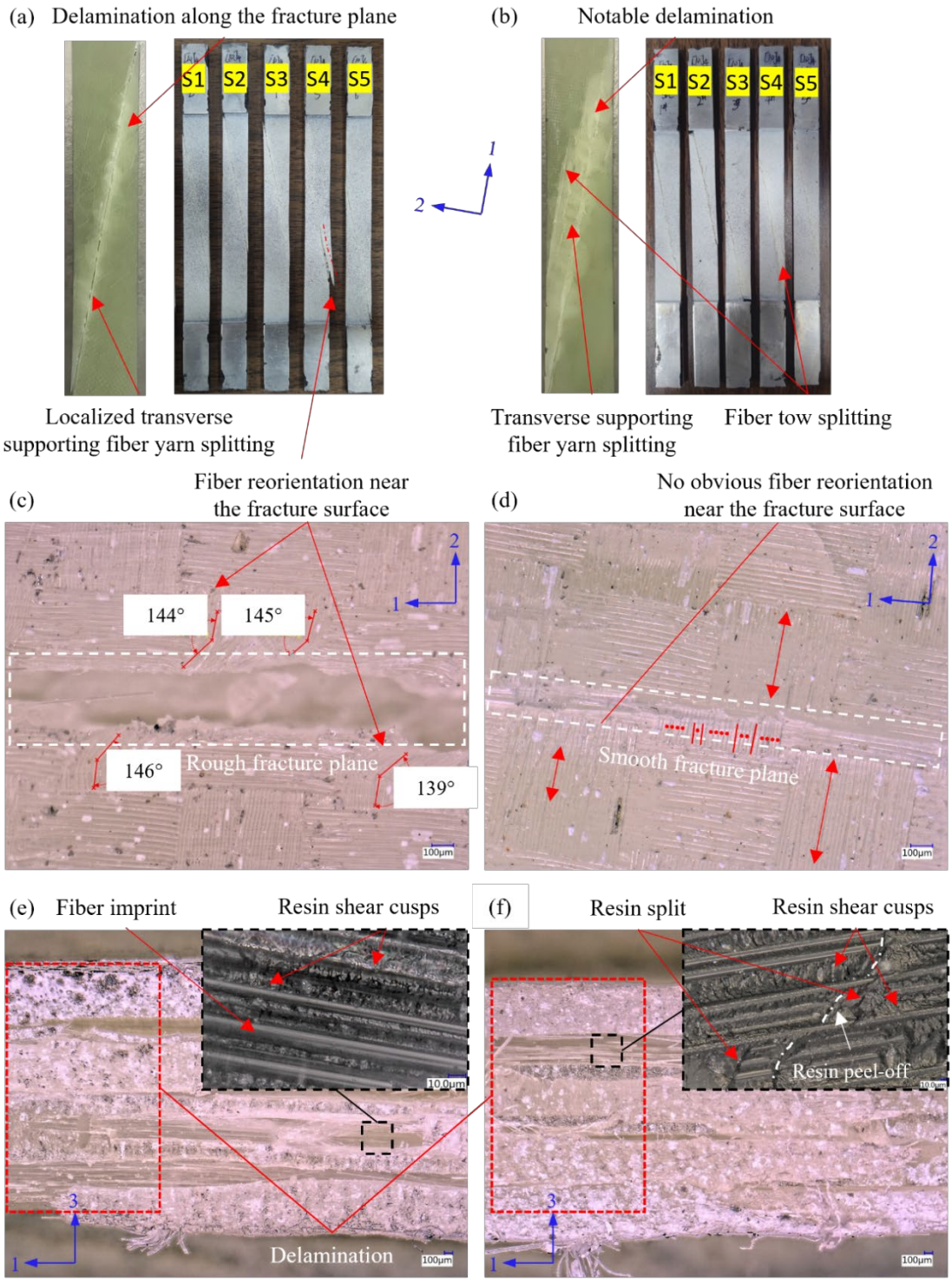


Fig. 4-13. Fractography of UD-NCF GF/acrylic subjected to 10° off-axis tensile loading at: (a), (c), and (e) RT; (b), (d), and (f) -50°C.

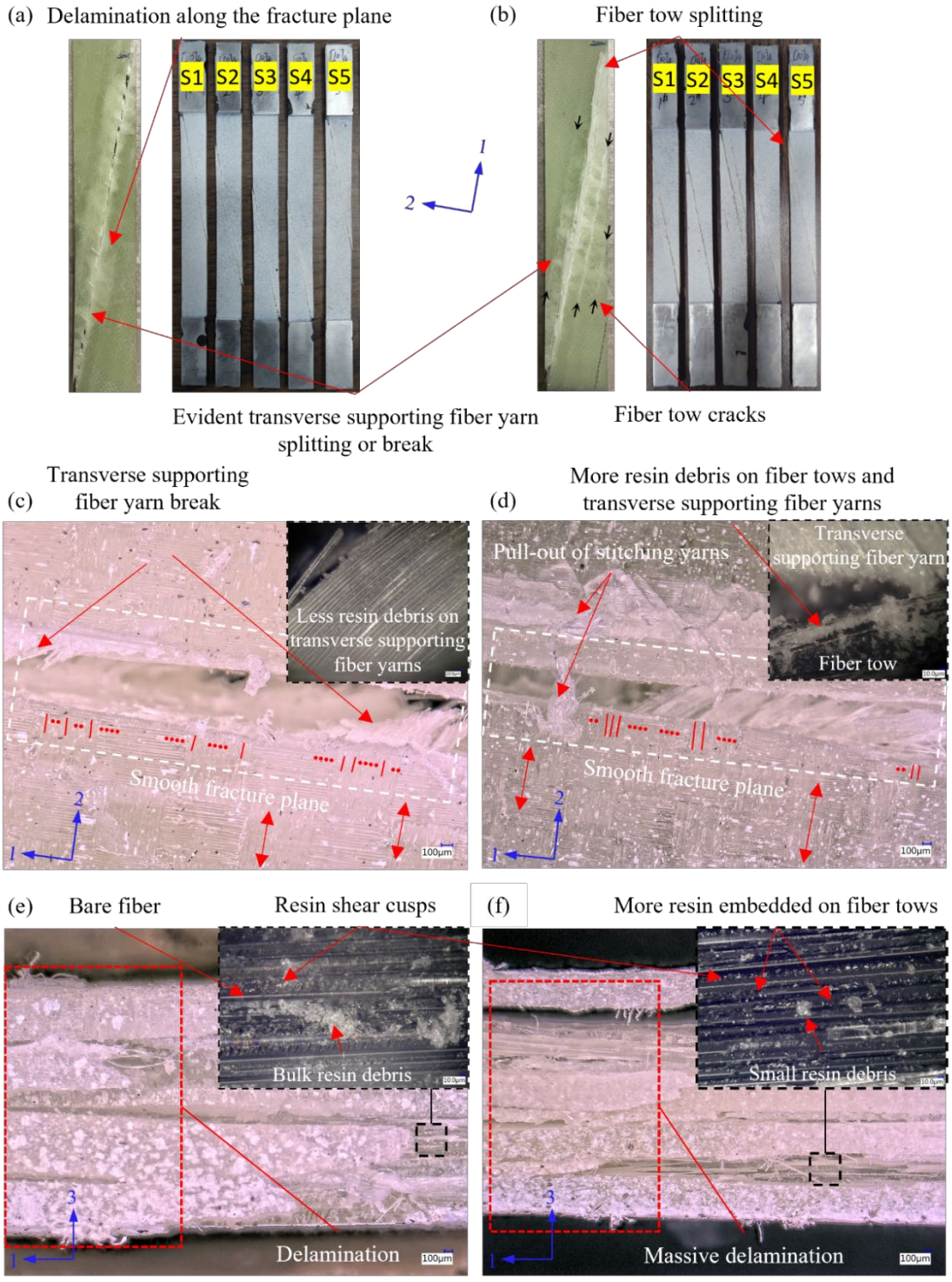


Fig. 4-14. Fractography of UD-NCF GF/epoxy subjected to 10° off-axis tensile loading at: (a), (c), and (e) RT; (b), (d), and (f) -50°C.

4.3 Task 2: In-situ Damage Characterization of Cross-ply UD-NCF Laminates under Quasi-static Tensile Loading using Developed Digital Imaging Technique

An automated in-situ digital imaging technique was developed to characterize damage in infused UD-NCF glass fiber/reactive thermoplastic acrylic (NCF GF/acrylic) cross-ply laminates at RT (22°C) and LT (-50°C). Post test optical microscopy was employed to validate the observed damage modes and identified failure mechanisms for both ambient temperatures. The influence of low ambient temperature on damage evolution of the tested cross-ply specimens was assessed using quantitative damage metrics, including crack density, crack density rate (CDR), and crack length.

4.3.1 Experimental details

4.3.1.1 Mechanical testing procedure

Rectangular specimens measuring 275 mm × 25 mm × 2.8 mm were water jet cut from the fabricated panels and equipped with adhesively bonded aluminum end tabs measuring 50 mm in length (Fig. 4-15). Quasi-static tensile tests were conducted on cross-ply specimens with a $[0°/90°]_s$ stacking sequence (Fig. 4-15a) under displacement control at a crosshead speed of 2mm/min. At least five repeated tests were performed at each temperature condition using a servo-hydraulic MTS 810 test frame with a ±50 kN capacity load cell, in accordance with ASTM D3039 [178]. For low temperature testing, both mechanical grips and test specimens were subjected to the cooling environment under load control to ensure no pre-damage on specimens and achieve thermal equilibrium before performing any test; after reaching the target temperature of -50°C, the specimen was left to condition and stabilize for a minimum of 5 to 10 minutes (see Section 4.2.1 for details).

For strain measurement, 3D DIC was performed on a subset of specimens to monitor the displacement fields using two 5 MP cameras with F2.8/50mm lenses positioned in front of the test specimen (see Section 4.2.1 for details). The ROI for strain evaluation, a 120 mm × 20 mm area at the center of the test specimen, was finely speckled with black-on-white spray paint. GOM ARAMIS was utilized to determine the strain fields using images captured at a frequency of 3 fps. The average strain in the ROI was determined using a subset size of 19 pixels, step size of 6 pixels, and a strain filter of median.

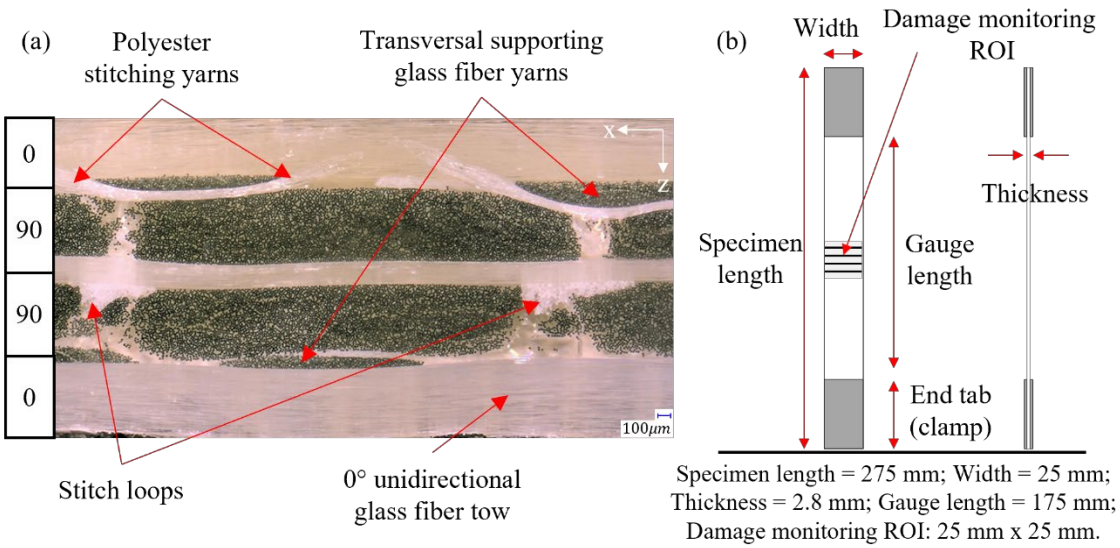


Fig. 4-15. (a) Image of the material microstructure and laminate plies; (b) test specimen configuration and dimension.

4.3.1.2 Digital imaging technique for in-situ damage monitoring

In order to track the evolution of damage during quasi-static tests at both RT and LT, an in-situ digital imaging technique was developed (Fig. 4-16). A dimmable RGB light source was placed behind the specimen during the test and the light transmitted through the material was then captured by two digital cameras positioned in front of the specimen (Table 4-3). Two additional LED lamps were positioned above and below the digital cameras for light compensation and improved damage detection. Due to the translucent nature of the studied material, the initiation and progression of damage was clearly captured as dark bands. To enhance the visibility of these dark bands, violet light was used because of the higher wave energy and the ability to penetrate deeper into the material. From the images of the specimen surface captured by the digital cameras, the initiation and propagation of cracks were automatically quantified by an in-house developed Python@ code which is based in part on the method described in Refs.[26], [146]. Images of 720 x 1600 pixels were first cropped, stacked and shift-corrected to ensure a consistent feature extraction within the damage monitoring ROI (e.g. cracks, Fig. 4-15b). A Gabor filter was then applied to the stacked images to identify cracks in the 90° fiber tow direction. Thresholding was applied to distinguish cracks from the image background and cracks were counted and measured. An example of a processed image (675 x 675 pixels) of a specimen that contains cracks is shown in Fig. 4-17, which demonstrates the ability of the developed code to accurately identify

cracks. At least two additional tests adopting the developed digital imaging technique were conducted at each temperature condition.

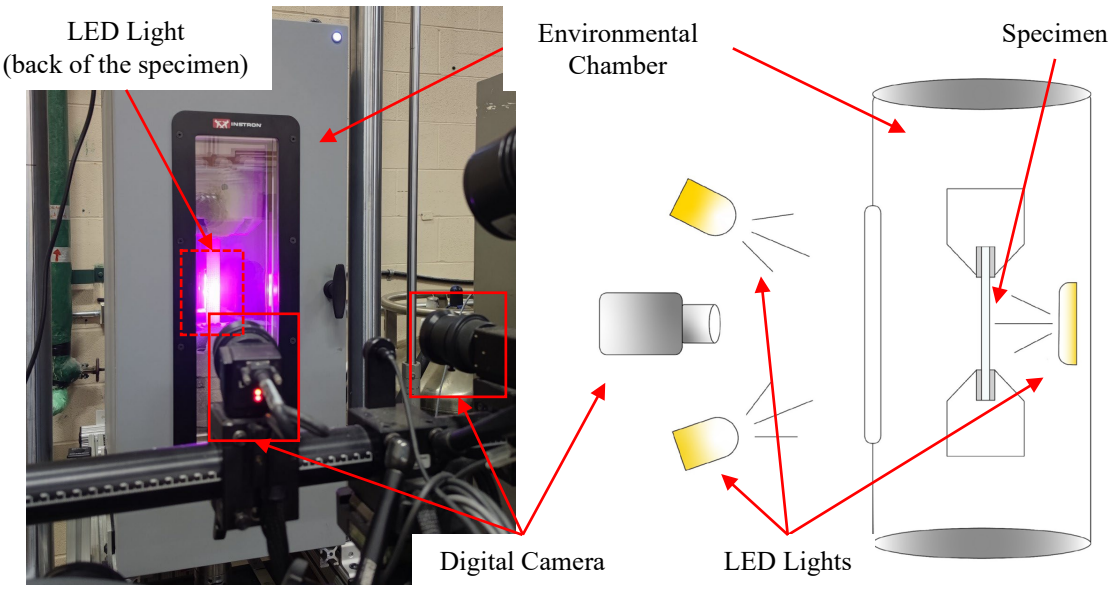


Fig. 4-16. Digital imaging technique for in-situ damage monitoring with environmental chamber set-up for testing at -50°C (only one digital camera is used for damage monitoring).

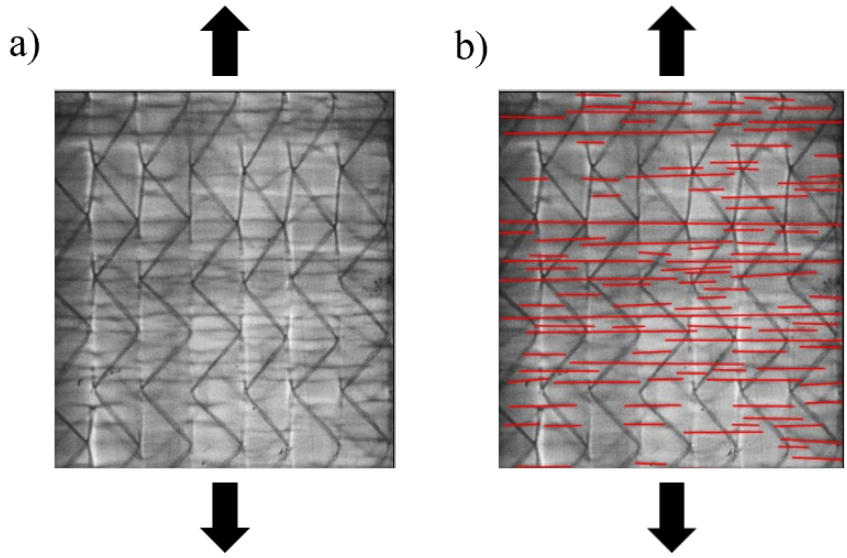


Fig. 4-17. Illustration of image processing to identify cracks: a) original image of specimen containing cracks; b) processed image with cracks identified in red.

4.3.1.3 Destructive and postmortem damage inspection

To validate the capability of the developed digital imaging technique to monitor damage, particularly at low temperature, microscopy was employed to observe axial- and cross-sectional samples extracted from test specimens that were loaded up to different levels of stress (i.e., 20% UTS, 50% UTS, and 75%-80% UTS; where UTS = ultimate tensile strength). When pre-defined loads were reached, the test specimens were unloaded and sectioned using a wet sectioning machine. The cut samples were then cold mounted in a cylindrical silicon mold using a fast-curing acrylic resin (LECOSET 7008). The visible sample surface was subsequently wet-sanded using 180-grit, 320-grit, 600-grit, 800-grit, 1000-grit, and 1200-grit paper (2 minutes per grit paper), followed by polishing using 3μm and 1μm diamond paste with extender fluid (5 minutes per diamond paste). All the cold-mounted samples were examined under a VHX-5000 opto-digital microscope (Keyence).

Postmortem analysis of failed test specimens was also performed to assess the final stages of damage that led to the observed failure as well as to compare any distinctions in the damage mechanisms at different temperatures. An opto-digital microscope was employed to observe the fracture surfaces and failed specimen edges, while a Quanta FEG-250 SEM was used to examine the specimen fracture surfaces.

4.3.2 Laminate effective stress–strain response and modulus degradation

The effective stress-strain responses of the cross-ply laminates were consistent among different specimens for each temperature condition (Fig. 4-18). The laminate initially exhibited a linear stress-strain response at low strain levels, followed by a slight non-linear response prior to breakage at both ambient temperatures. A sharp transition at the stress in the range of 70-88 MPa (~0.26% strain) was observed at LT (Fig. 4-18a), while at RT a more gradual transition was observed at a stress >100 MPa (>0.5% strain). Several load drops were observed for LT specimens prior to failure due to successive breakage of 0° fiber tows (see Section 4.3.3.3 for more details). The effective laminate longitudinal moduli, extracted from the secant slopes of the stress-strain data, were normalized by the initial Young's moduli and plotted against the applied stress (Fig. 4-18b). Four distinct damage evolution stages were identified and correlated with longitudinal modulus degradation for both ambient temperatures considered: 1) elastic region (stage I), characterized by the constant secant moduli; 2) the initiation and propagation of 90° fiber tow cracks (stage II), corresponding to the greatest drop of longitudinal moduli; 3) the onset of 0° fiber tow cracks (stage III), characterized by a gradual decrease

of longitudinal moduli; 4) 0° fiber breakage and delamination (stage IV) due to the interactions of the developed damage modes, leading to the final failure of the specimen (refer to Sections 4.3.3.2 and 4.3.3.3 for more details).

A two-sample t-test was performed to determine whether the changes in the effective mechanical properties of the laminate at 22°C and -50°C were significant (Fig. 4-18c, Table 4-7). The tensile strength and Young's modulus increased by 4.21% and 13.04%, respectively, at -50°C due to the increased modulus and strength of the matrix and the increased fiber-matrix interfacial strength. The increase of the laminate tensile strength at LT may have been caused by the interaction of several competing mechanisms that were acting simultaneously. First, the low ambient temperature would tend to decrease polymer chain mobility and a allow for a longer time for stresses to relax, which would lead to an increase in the binding force between the PMMA molecules and the matrix strength [16], thus, contributing to the increased strength of the composite material. Secondly, the mismatch in the coefficient of thermal expansion (CTE) between the fibers (~$5 \times 10^{-6} C^{-1}$ for a typical E-glass fiber) and matrix ($6.5 \times 10^{-5} C^{-1}$ [170]) would result in the development of localized thermal stresses near the fiber-matrix interfaces, while the dissimilar effective CTE between adjacent plies with distinct orientations would further contribute the state of the thermal stresses within the plies. The existence of thermal stresses coupled with increased matrix brittleness may lead to the early onset of localized damage at LT conditions (see Section 4.3.3.3) and a more notable degradation of the effective modulus (Fig. 4-18b). Hohe et al. [179] developed micromechanical finite element models to study the local stress distribution in the matrix during temperature cool down (from 20°C to -253°C) for a carbon fiber/epoxy unidirectional composite and cross-ply laminate. They found that the presence of the additional plies in the cross-ply laminate resulted in a further increase in the magnitude of the matrix residual stresses when compared to the unidirectional composite, which was due to the distinct effective CTE between the plies. Similar findings were reported by Sharifpour et al. [180] for cross-ply carbon fiber/epoxy laminate for different cooling temperature ranges (ΔT=-50, -75 and -100°C). Chemical shrinkage during the in-situ polymerization of Elium® could have also contributed to the development of residual stresses, where the extent of volumetric shrinkage may range from 9% to 20% for PMMA [181]. Nevertheless, increased thermal contraction of the matrix relative to the glass fibers along their transversal direction would lead to an increase in the fiber-matrix interfacial strength (see Section 4.3.3.3), which were also reported in previous studies [56],[16]. Moreover, compressive stresses would tend to develop along the glass fiber direction in the 0° plies owing to the mismatch in the effective

CTE between the 0° and 90° plies, which may have also alleviated the tensile stresses in the 0° plies during mechanical loading. Therefore, at a low ambient temperature the combination of increased matrix strength coupled with the effect of thermal stresses within the load bearing 0° plies contributed to an increase in the laminate tensile strength, outweighing the increased brittleness of the matrix. An interesting observation is that the averaged strain at failure were comparable at both temperatures (Fig. 4-18b), which is contrary to some of the literatures where the elongation at break decreased with the decrease of temperature [51],[182],[183]. Therefore, the focus of the subsequent paragraphs is on the damage development and microscopic investigation of the test specimens with the aim of identifying the mechanisms responsible for the difference in the exhibited behavior.

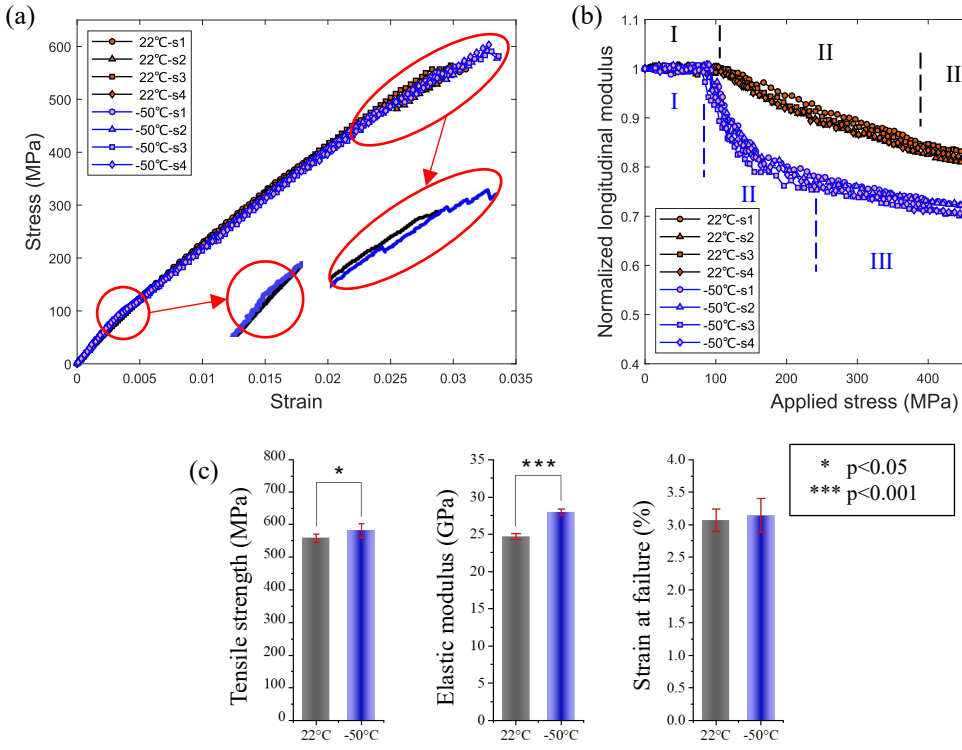


Fig. 4-18. Quasi-static tensile test results at 22°C and -50°C for the cross-ply specimens: (a) stress-strain responses; (b) normalized longitudinal modulus degradation curves (stages I-IV are indicated); (c) mechanical property comparison (average values and standard deviation shown in bar charts).

Table 4-7. Average laminate properties (± STV).

	Tensile Strength (MPa)	Young's Modulus (GPa)	Strain at failure (%)	Strain at onset of damage (%)
RT	558.67 (±13.69)	24.69 (±0.42)	3.072 (±0.17)	0.60
-50℃	582.21 (±22.46)	27.91 (±0.44)	3.144 (±0.26)	0.26
Change in property (p value from t-test)	+4.21% (0.040)	+13.04% (<0.001)	+2.34% (0.309)	-56.67% (-)

4.3.3 Qualitative damage analysis

4.3.3.1 Verification of digital imaging technique and main observed damage mechanisms

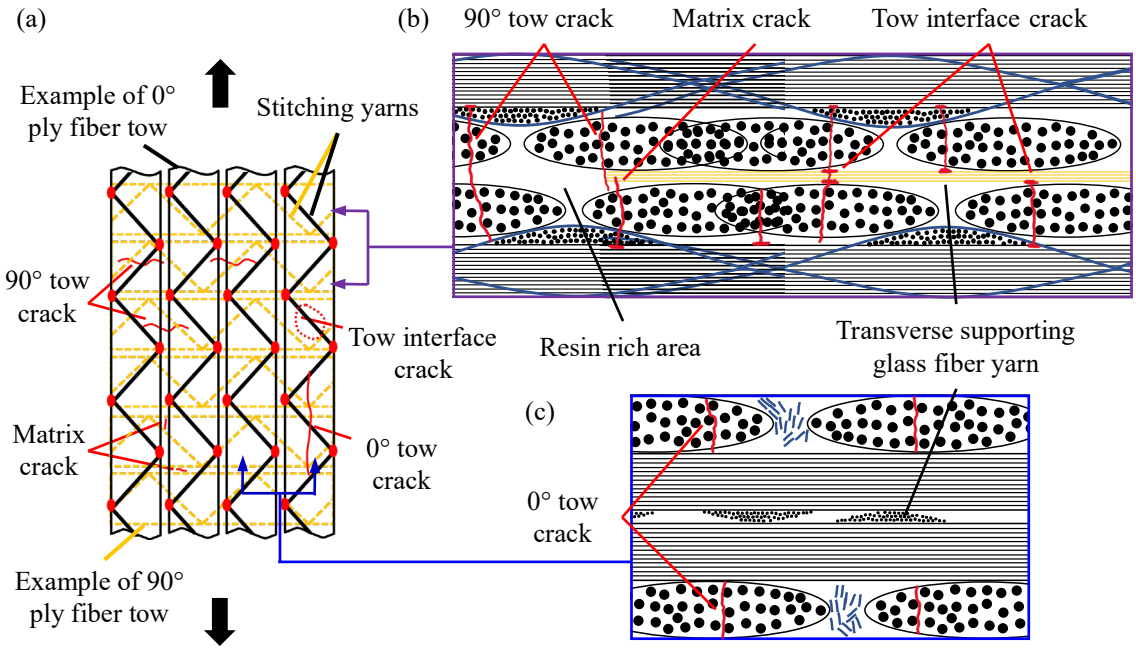


Fig. 4-19. Schematic of the main observed damage modes: (a) specimen surface view; (b) specimen edge view with resin rich area and with supporting glass fiber yarns between adjacent 90° fiber layers, respectively; (c) specimen cross-sectional view.

Qualitative analysis of the UD-NCF glass fiber/acrylic laminates focused on the characterization of damage mechanisms using the developed digital imaging technique and assessing their dependence on temperature. The observed damage mechanisms were complex due to the distinctive microstructure of

the studied material (Fig. 4-19), which included: (i) cracks within the 90° fiber tows which initiated at the stitch sites; (ii) matrix cracks in the resin rich regions; (iii) cracks within 0° fiber tows propagating along their axes; (iv) localized cracks at the 0°/90° fiber tow interface and along the tow peripheries. Note that these damage modes will be referred to as 90° tow cracks, matrix cracks, 0° tow cracks, and tow interface cracks, respectively. Intra-laminar damage modes identified from the captured surface images using the developed digital imaging technique correlated well with the damage observed on the edge and cross-section of the same specimen (Fig. 4-20).

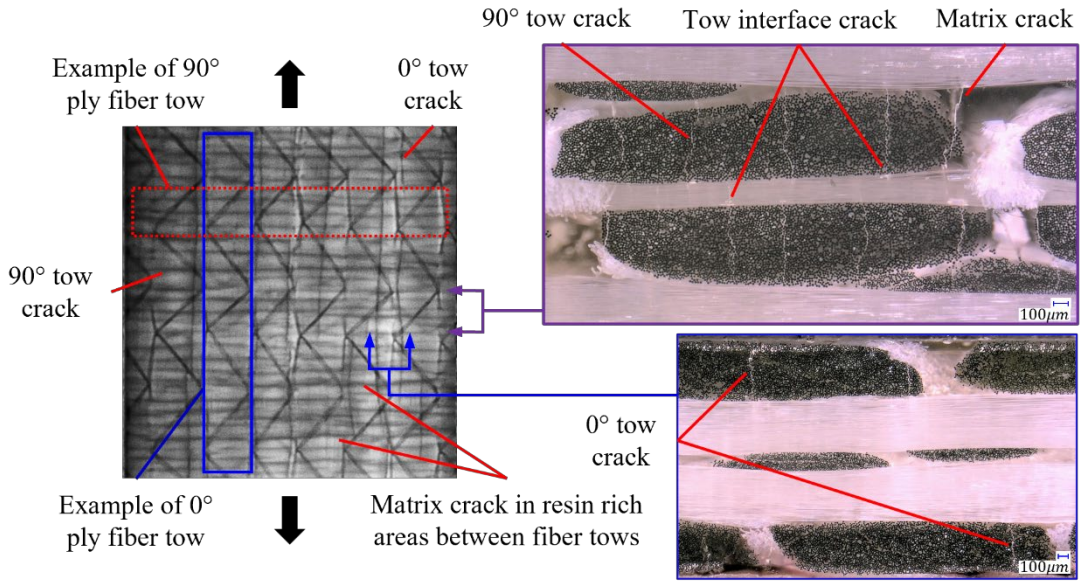


Fig. 4-20. Surface image captured by the developed digital imaging technique and the corresponding microscopic observation on the edge and cross-section of the same specimen.

4.3.3.2 Damage evolution and failure assessment in RT specimens

A series of surface images were captured for the specimens tested at 22°C at different stress levels (Fig. 4-21). The first observed damage mechanisms were 90° tow cracks initiating at 110-140 MPa or ~0.60% strain (Fig. 4-21b), which corresponds to the beginning of stage II in Fig. 4-18b. Fewer cracks were observed at this stress level and the majority of visible 90° tow cracks were localized and located at the adjacent stitching sites. Possible reasons could be the high stress concentrations at the stitch sites or a weak stitch-matrix interface as was reported by Suratkar [73] for a UD-NCF carbon fiber/epoxy composite material. The microstructural characteristics of the studied NCF fabric where stitching loops cause localized in-plane misalignment of the fiber tows (Fig. 4-1), as well as the compaction of the

fabric layers during processing which may result in slight out-of-plane crimping of fiber tows (Fig. 4-15a), might also facilitate damage initiation at stitching sites. This observation was further validated by the microscopic results which showed the initiation of 90° tow cracks at the stitch sites near the stitch loops or in the vicinity of the supporting glass fiber yarns (Fig. 4-22a). Note that there were no visible voids observed in the vicinity of the stitching sites, so the presence of voids in damage initiation was not considered.

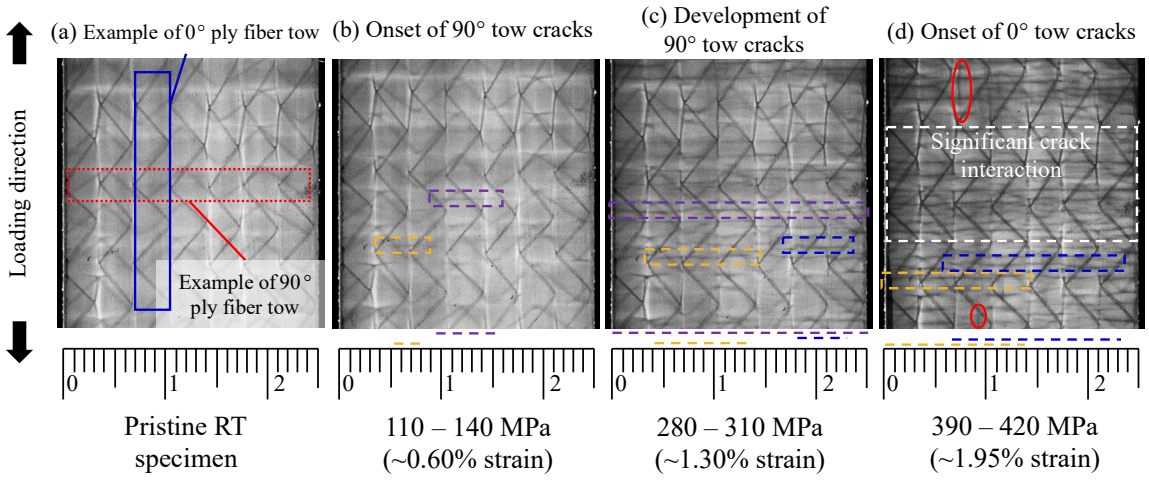


Fig. 4-21. Intra-laminar damage evolution in cross-ply laminates at 22°C (units for scales: cm).

Once the stress increased to 280-310MPa or ~1.30% strain (Fig. 4-21c), additional 90° tow cracks developed and tended to span along the entire width of the specimen, where the majority of tows were limited to one crack. During the evolution of 90° cracks along the fiber tow direction (i.e., crack tunneling), two forms of intra-tow crack interaction cases were observed: (i) cracks coalesced and extended along a straight plane across the width of the specimen (purple dashed line in Fig. 4-21c); (ii) offset cracks that initiated at different locations within the tow propagated passed each other without coalescing (yellow and blue dashed lines in Fig. 4-21c). For the latter case, the interaction of intra-tow cracks resulted in slower crack propagation due to the crack shielding effect. Similar observations were found in the experiments conducted by Shen et al. [145] and Lafarie-Frenot et al. [184]. Note that at this stage in loading, there were no visible cracks in the 0° fiber tows.

Once the applied stress increased to 390-420 MPa or ~1.95% strain, which corresponds to the beginning of stage III in Fig. 4-18b, the number of 90° tow cracks within ROI reached saturation and the crack spacing (i.e., crack density) was constant along the entire specimen length. Significant

interactions between the developed 90° tow cracks (described in the previous paragraph) were observed in the same fiber tow. Some localized 0° tow cracks and tow interface cracks were also observed (Fig. 4-21d and Fig. 4-22b). Similarly, the majority of the observed cracks were located within the 90° fiber tows, where many tows contained two or more cracks. At the resin rich regions between adjacent 90° fiber layers (left configuration in Fig. 4-19b), 90° tow cracks tended to coalesce and cross both layers (Fig. 4-22b). Moreover, there was no evidence of delamination between fiber layers.

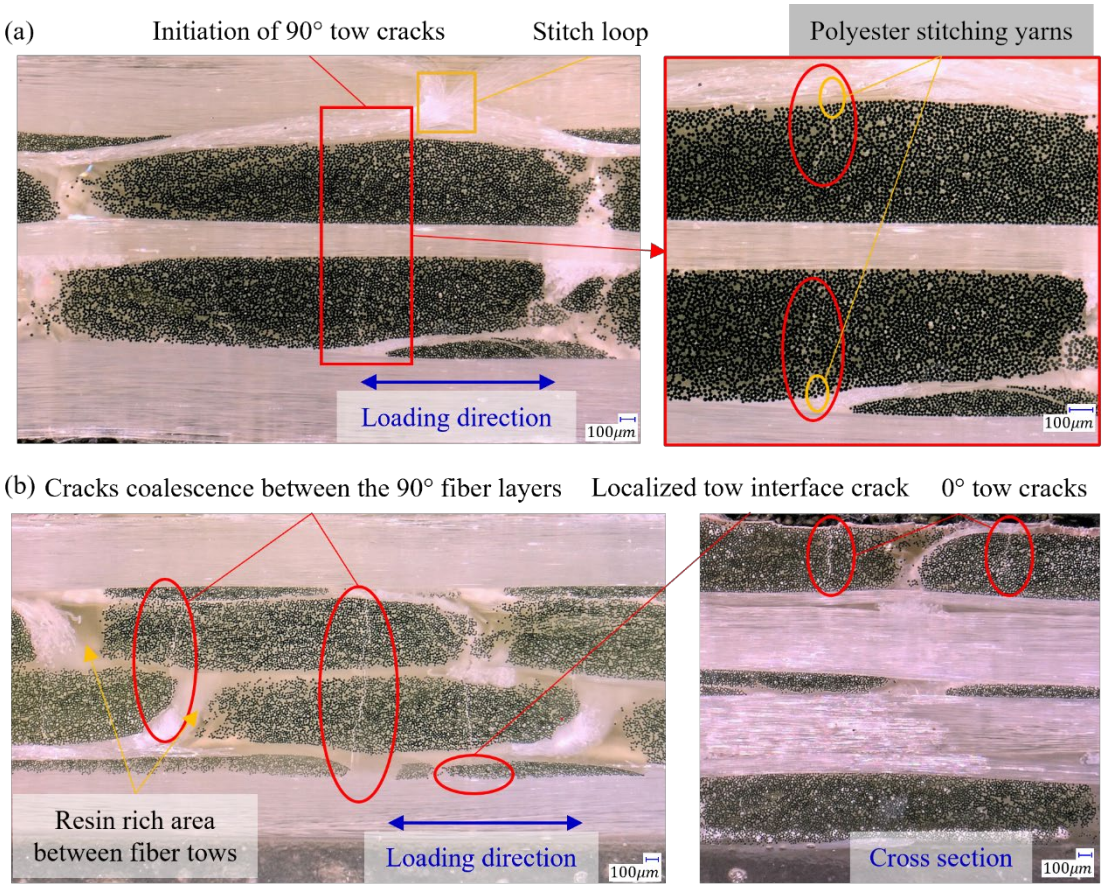


Fig. 4-22. Micro-scale damage observation of RT samples tested up to: (a) 110 MPa; (b) 400 MPa.

With further increase of the load prior to failure (i.e., stage IV in Fig. 4-18b), 0° fiber tows were supporting the entire applied load, which result in localized splitting and weakening of these tows. Subsequently, large-scale 0° fiber tow splitting and delamination cracks between 0° and 90° fiber layers developed, contributing to final failure of the specimen (Fig. 4-23a). The fracture surface of the internal 90° fiber layers was perpendicular to the loading direction. The presence of 0° fiber bundle pull-out

from individual tows and fiber breakage was revealed by the brushy appearance of the fracture surface (Fig. 4-23b). The separation of different fiber layers due to delamination was observed and occurred just prior to fracture (Fig. 4-23c). The above morphology of the fracture surface revealed that failure was brittle in nature.

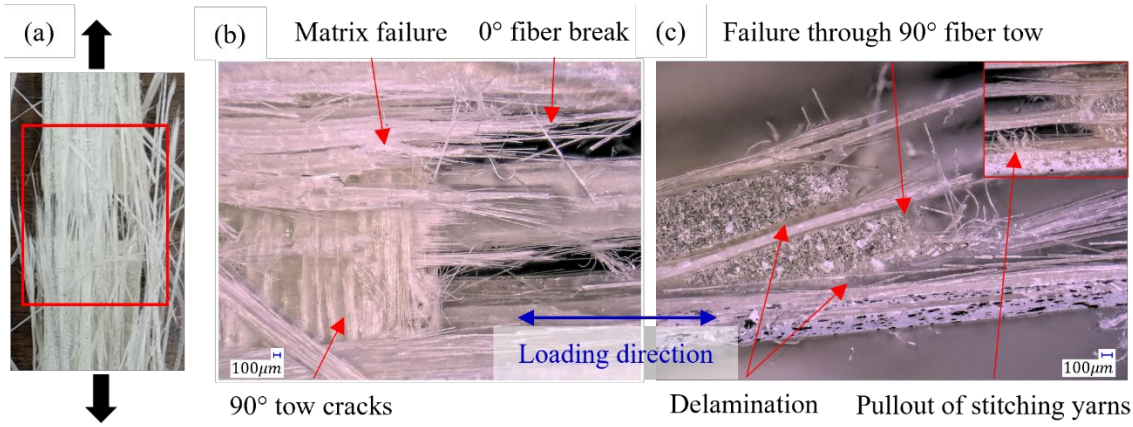


Fig. 4-23. Fractography of specimen tested at 22°C: (a) image of fracture surface; (b) micrograph of fracture surface view; (c) micrograph of fracture edge view.

4.3.3.3 Damage evolution and failure assessment in LT specimens

At -50°C, the material exhibited increased sensitivity to damage and the damage mechanisms were more complex (Fig. 4-24). 90° tow cracks near the stitch sites were first observed at lower stress levels, 60-90 MPa or ~0.26% strain (beginning of stage II), compared to the specimens tested at 22°C due to increased brittleness of the matrix. This result is consistent with the observed bilinear stress-strain response and sudden decrease of the longitudinal modulus at -50°C (Fig. 4-18). Once the applied stress exceeded the transition stress, the number of 90° tow cracks increased significantly and typically two or more cracks were observed per tow. Microscopic observation after loading to 116 MPa further demonstrated that the 90° tow cracks initiated at the stitching sites (Fig. 4-25a). Moreover, there were no 0° tow cracks or tow interface cracks observed at this stage.

When the load increased to 200-230 MPa or ~1.06% strain (beginning of stage III), few 0° tow cracks developed, although most of the observed cracks were 90° tow cracks which had a tendency to span the entire width of the specimen and propagate uniformly throughout the length of the specimen with consistent spacing. With further increase of the applied load, the number of 90° tow cracks reached

saturation and the number of 0° tow cracks increased continuously. However, the developed 90° and 0° tow cracks were not able to extend sufficiently to trigger material failure, where instead their density increased causing a stress relief and enabling larger specimen elongation. Similar findings were observed by Li et al. [55]. Microscopic results (Fig. 4-25b) after applying 230 MPa showed the observed 0° tow cracks and the coalescence of 90° tow cracks at the resin rich area between different 90° fiber layers. Note that at this load condition, there was no indication of tow interface cracks.

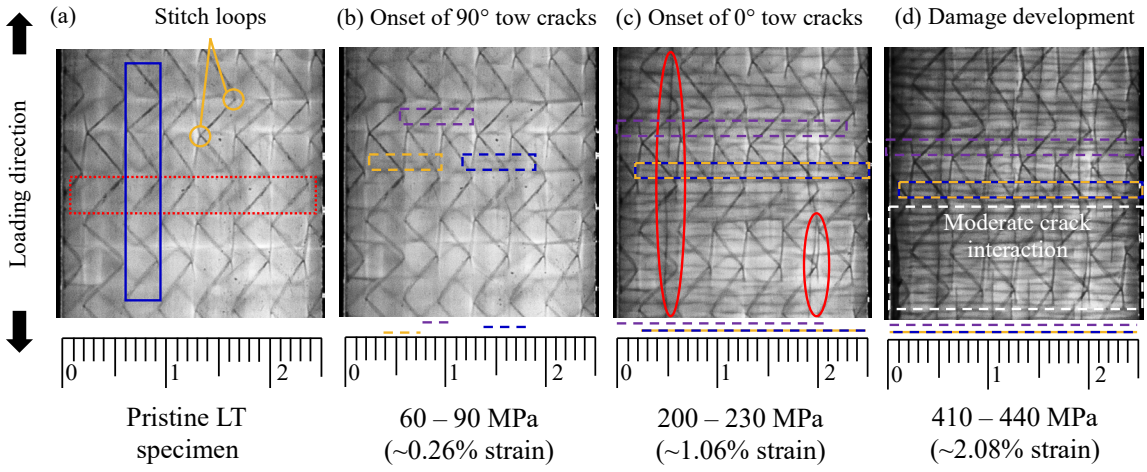
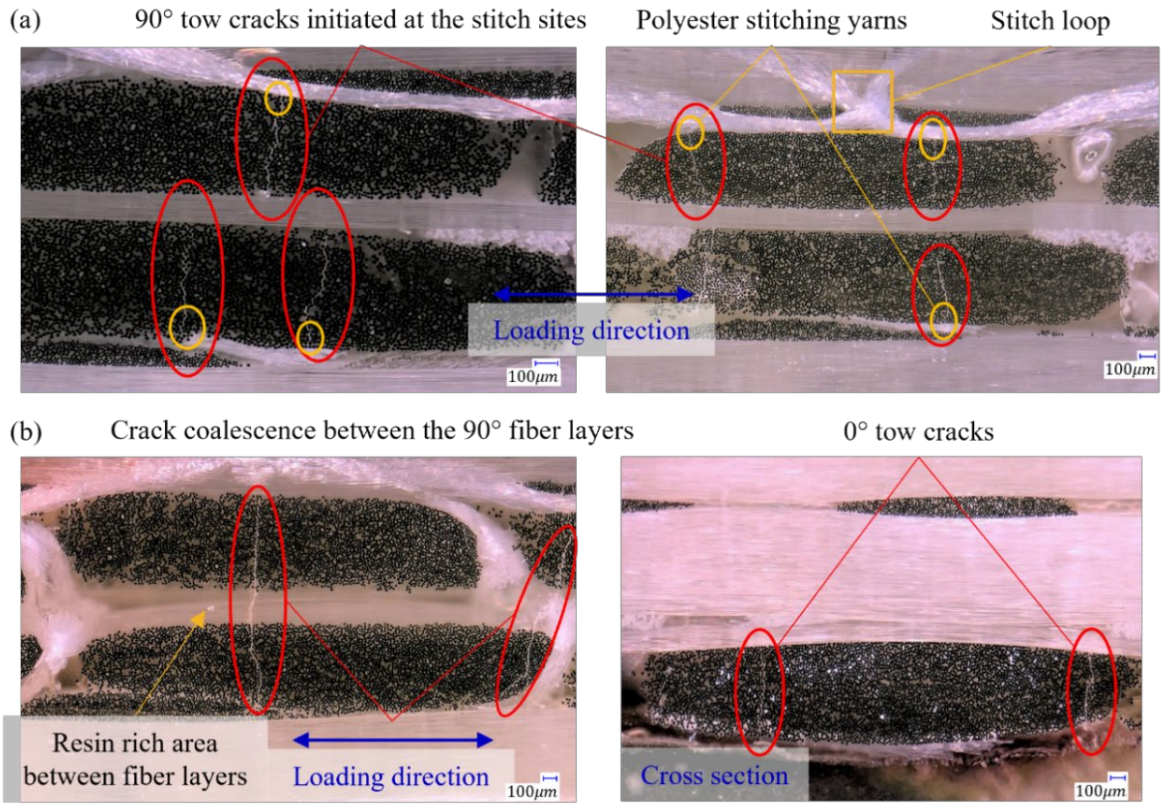


Fig. 4-24. Intra-laminar damage evolution in cross-ply laminates at -50°C (units for scales: cm).

As load continued to increase until 410-440 MPa or ~2.08% strain, localized tow interface cracks were observed at the supporting glass fiber yarn region between adjacent 90° fiber layers (right configuration in Fig. 4-19b). These cracks tended to propagate through the thickness of the material, instead of along the tow interface as a result of the enhanced interlayer adhesion and interface strength between fiber and matrix at -50°C (Fig. 4-25c). In addition, the specimen stacking sequence may have also limited crack propagation along the tow interface, as the 0° fibers provided the primary load-carrying capacity and resisted tow interface crack growth.

With the load increased to 460-525 MPa or 2.60%-3.00% strain (beginning of stage IV), localized 0° fiber tow splitting and delamination between different fiber layers were observed, causing several drops of the load (Fig. 4-18a). The damage continued to develop (subsequent fracture of more 0° fiber tows and, later, large-scale delamination) until ~3.14% strain, leading to the final failure of the specimen (Fig. 4-26). The morphology of the fracture surface was similar to that of the RT specimen (Fig. 4-26a); however, the damage was more exaggerated. The external 0° fiber layers ruptured and

scattered into significantly more slender fiber bundles and there were notably more 90° tow cracks and more extensive 0° fiber tow pull-out compared to the RT specimens. Moreover, more resin debris on fibers (Fig. 4-26b) and resin split (Fig. 4-26c) were observed compared to more bare fibers and matrix failure at 22°C (Fig. 4-23b). SEM results of the associated fracture surfaces for representative specimens further demonstrated these phenomena (Fig. 4-27). Notable matrix plastic deformation near bridged fibers were observed at 22°C (Fig. 4-27a) compared to matrix brittle failure at -50°C (Fig. 4-27c). A detailed observation on single fiber revealed bare fibers at 22°C (Fig. 4-27b) in comparison to fiber surfaces with more resin adhered at -50°C (Fig. 4-27d), indicating an enhanced interface strength at LT. Furthermore, the reduced interaction between 0° tow cracks and the delay in the formation of large-scale delamination cracks also contributed to the increased strength of the specimen by increasing the number and the effective load carrying capacity of fiber tows. This phenomenon can also help explain the observed larger strain at failure when compared to that at 22°C.



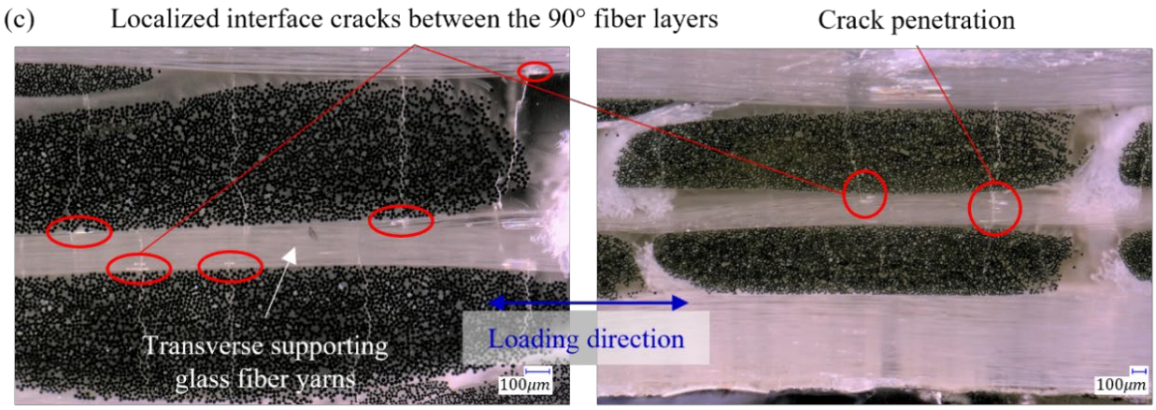


Fig. 4-25. Micro-scale damage observation of LT samples tested up to: (a) 116 MPa; (b) 230 MPa; (c) 440 MPa.

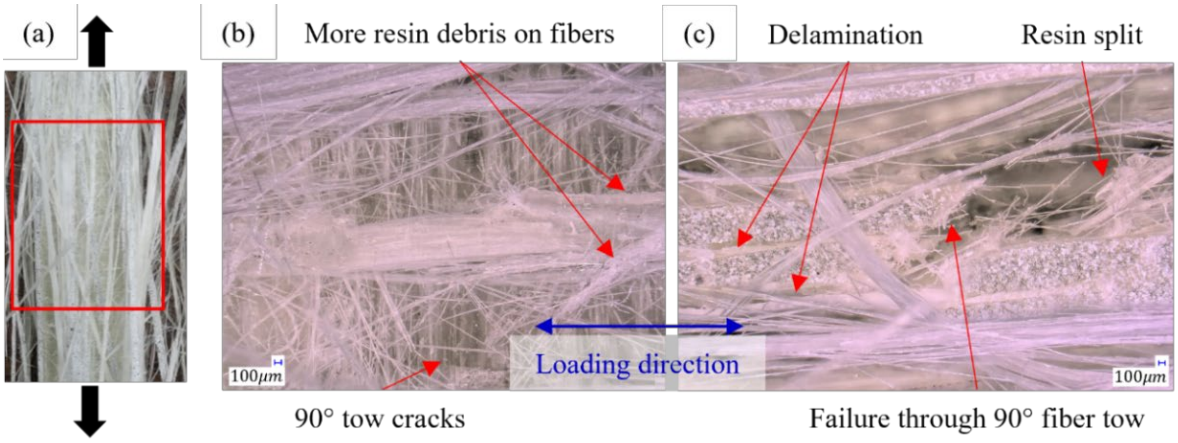


Fig. 4-26. Fractography of specimen tested at -50°C: (a) image of fracture surface; (b) micrograph of fracture surface view; (c) micrograph of fracture edge view.

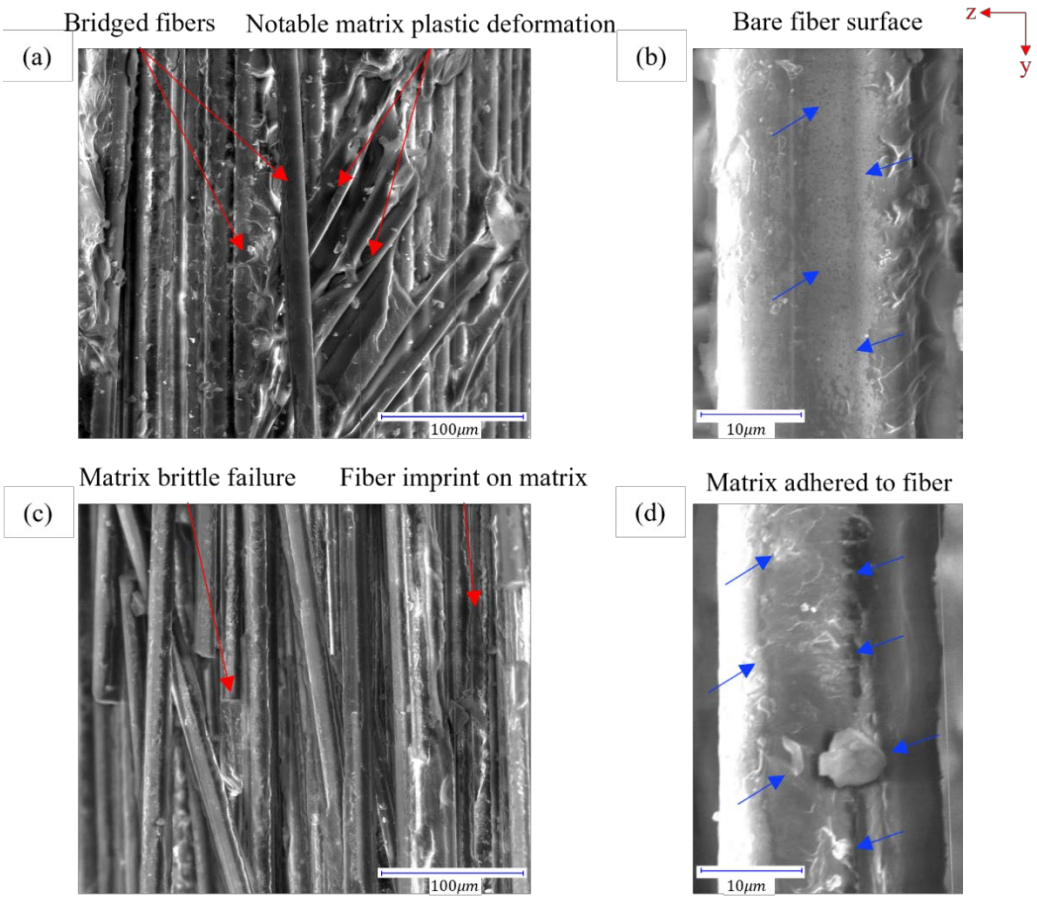


Fig. 4-27. Images of fracture surfaces for representative specimens captured using SEM: (a), (b) View on a fiber tow in the 90° ply for a specimen tested at 22°C; (c), (d) View on a fiber tow in the 90° ply for a specimen tested at -50°C.

4.3.3.4 Chronology of damage evolution

Although significantly more 90° tow cracks and more complex damage modes were observed at -50°C, similar fracture events occurred which ultimately led to the final failure of the specimen. A schematic of the damage evolution from crack initiation to specimen failure is shown in Fig. 4-28 along with the normalized stress-strain curve for both temperatures.

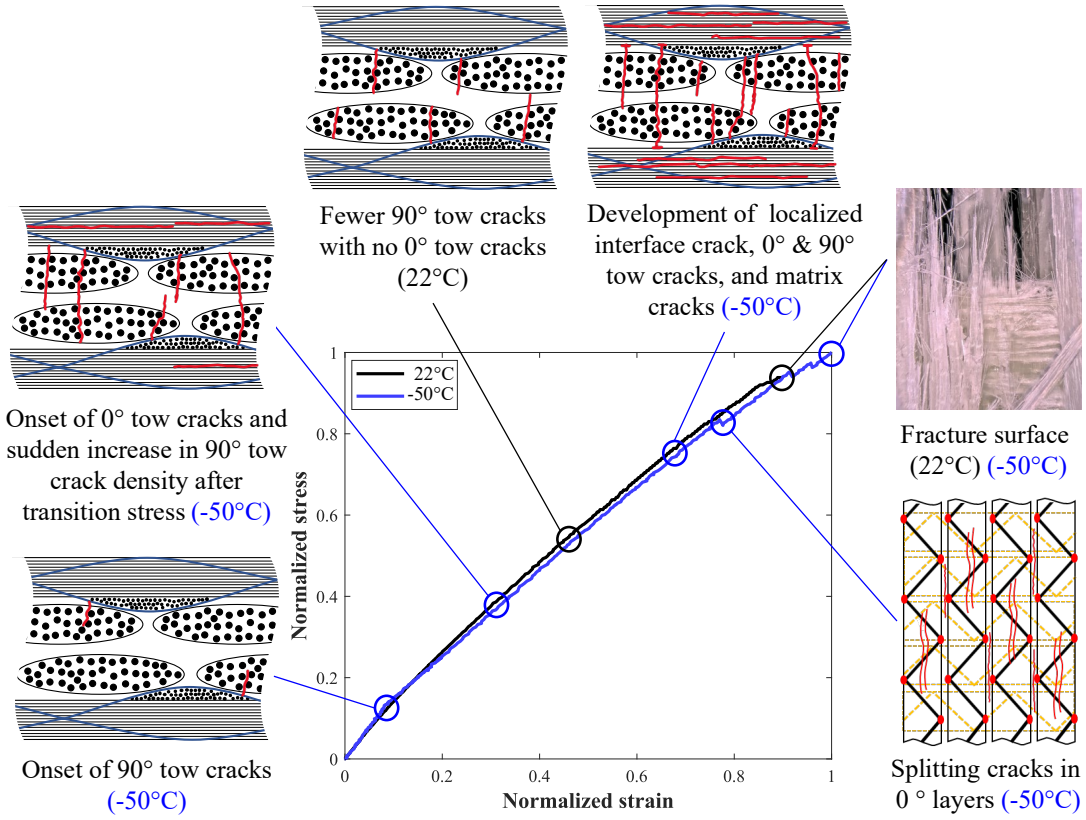


Fig. 4-28. Schematic of damage evolution at 22°C and -50°C subjected to quasi-static tensile loading (only resin rich area between 90° fiber layers is shown).

4.3.4 Quantitative damage analysis

To qualify and compare the damage state in the specimens at 22°C and -50°C, particularly during the crack propagation stage when the greatest stiffness degradation was observed, three damage variables were used, including 90° tow crack density (ρ), 90° tow crack density rate (CDR), and 90° tow crack length increasement (a-a_0) .

The 90° tow crack density (ρ) is defined in [26], [145], [146] as the ratio of the total combined crack length to the area of the observation region, and is given by:

$$\rho = \frac{\sum_{i=1}^{n} L_i}{w \cdot L} \tag{1}$$

where L_i is the length of the i-th crack, n represents the total number of cracks, w is the width of the specimen, and L is the length of the observation region.

90° tow crack density rate (CDR) is defined as the ratio of the change of crack density to the change of applied stress (S) in the propagation analysis, and is given by:

$$CDR = \frac{d\rho}{dS} \tag{2}$$

90° tow crack length increasement (a-a_0) is defined as the difference between the current crack length (a) and the initial crack length (a_0) considered in the propagation analysis, where a_0 was considered as to be at least two times the 90° fiber layer thickness according to Ref. [93].

The in-depth comparison of 90° tow crack density plotted against the applied stress for the specimens tested at 22°C and -50°C is shown in Fig. 4-29. At stage I, the 90° tow crack density grows earlier for LT specimens at ~83MPa compared to ~113MPa for those tested at 22°C. This agrees with the lower stresses to onset of stiffness degradation and crack initiation for LT specimens as shown in Fig. 4-18b and Fig. 4-24 respectively.

After the initiation (stage II), 90° tow crack density increases significantly with the decrease of temperature. This implies that when the applied stress is the same, the crack density evolves faster for the specimens tested at -50°C, indicating a decreased crack growth resistance as a result of the decrease in matrix ductility. Similar observations were found by Boissin et al. [185] in which a decrease of the transverse cracking threshold was observed for biaxial NCF glass fiber/Elium@ composites with a decrease of temperature from 40°C to 15°C. To quantify the rate of crack density evolution at this stage, the CDR for LT specimens was calculated and found to be nearly 2 times greater than the specimens tested at 22°C, contributing to an earlier crack saturation at relative low stress of ~230MPa. This is consistent with the observed damage modes from the front images in Fig. 4-21 and Fig. 4-24. Moreover, the constant CDR during crack propagation reveals a stable crack growth phase.

To gain a further understanding of the crack propagation at different temperatures, the first three independent cracks in different 90° fiber tows were considered to improve the statistical relevance of the results. From the front images captured by the digital camera, 90° tow cracks were found to propagate along the fiber direction (Fig. 4-21 and Fig. 4-24). The crack length was measured and the increasement of crack length was plotted against the applied stress (Fig. 4-30). The cracks propagate with an approximately constant rate at both temperatures, characterized by the slope of the fitted lines representing the crack growth rate (CGR). This further demonstrated a steady state propagation at the tested temperature condition, although the CGR at -50°C was much greater than the CGR at 22°C.

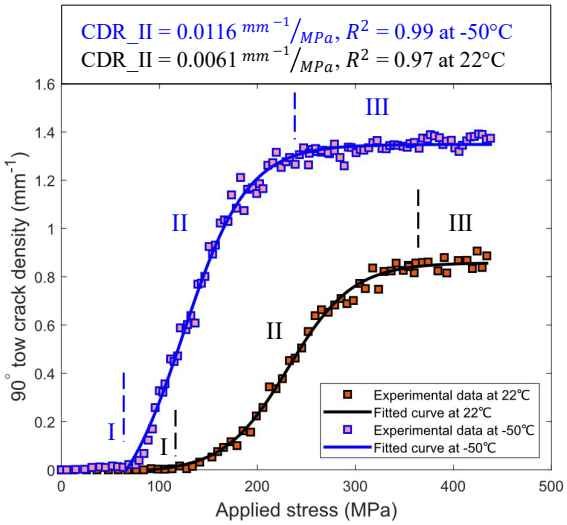


Fig. 4-29. 90° tow crack density evolution at 22°C and -50°C.

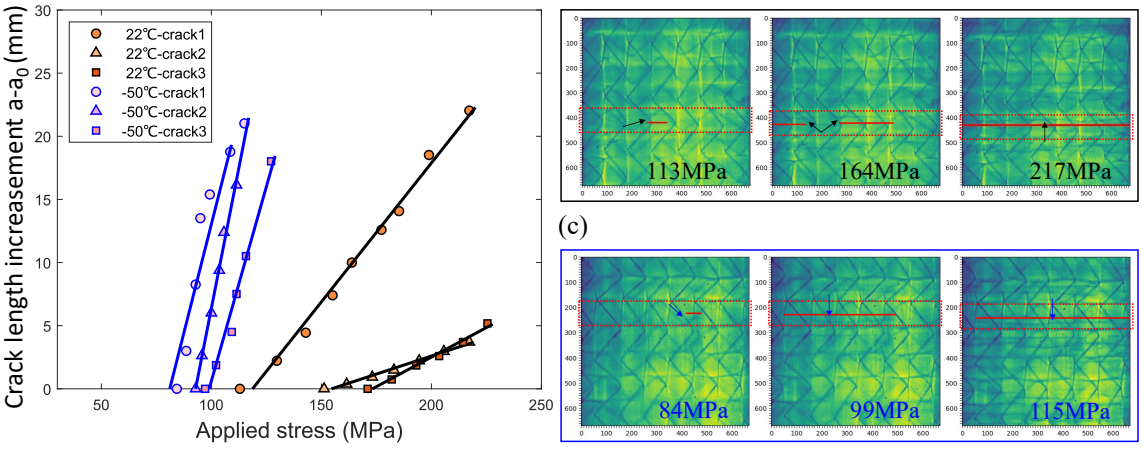


Fig. 4-30. Examples of independent crack propagation at 22°C and -50°C: (a) curves for the first three cracks in different 90° fiber tows; (b) illustration of the length increasement for crack 1 at 22°C; (c) illustration of the length increasement for crack 1 at -50°C (Note that for clear crack visibility purposes, the detected cracks were offset, the color of the images were tuned, and the axis were labeled in pixels).

4.4 Task 3: Characterization of Damage Evolution and Stiffness Degradation of Cross-ply UD-NCF Laminates under Tension-Tension Cyclic Loading using Integrated Digital Imaging Technique

A novel in-situ integrated digital imaging technique was developed to simultaneously characterize damage and monitor stiffness degradation in UD-NCF glass fiber/reactive thermoplastic (NCF GF/acrylic)) cross-ply laminates subjected to tension-tension cyclic loading. The developed digital imaging technique allowed for effective in-situ damage characterization and strain measurement, which enabled the automated identification of different damage mechanisms, observation of the locations of damage initiation, quantification of damage propagation (i.e., crack length increasement), and direct correlation of damage states with stiffness degradation for a single test specimen. Optical microscopy was used to capture damage on the edge of the tested specimens, providing a one-to-one comparison of the damage mechanisms detected using the developed digital imaging technique.

4.4.1 Experimental details

4.4.1.1 Tension-tension fatigue tests

All fatigue tests were conducted at RT on a servo-hydraulic MTS 810 test frame with a ±50 kN capacity load cell and hydraulic wedge grips. A tension-tension cyclic loading profile with a sinusoidal waveform of constant amplitude, a loading frequency of 5Hz, and a stress ratio of 0.1 was applied to the $[0/90]_s$ cross-ply specimens . Preliminary tests were performed on rectangular specimens as recommend by the ASTM D3479 test standard [186] and revealed premature failures at the end tabs. To address this issue, an iterated design process was employed to optimize the specimen geometry to mitigate stress concentrations near the tabbed regions and reduce end tab failures and slippage during the tests, refer to Fig. 4-31a for the optimezed specimen geometry. Two maximum stress amplitudes were chosen to assess fatigue damage evolution under two distinct loading conditions, specifically 50%UTS and 75%UTS (see Table 4-7 for cross-ply laminate strength). The fatigue tests were interrupted periodically to perform quasi-static tests under displacement control with a crosshead speed of 2mm/min to extract images of the specimen for detecting damage using the developed digital imaging technique and to evaluate the elastic modulus (Fig. 4-31b). The elastic modulus was determined using strains calculated using 3D DIC as described in Section 4.2.1. At least three repeated tests were conducted for each peak stress level.

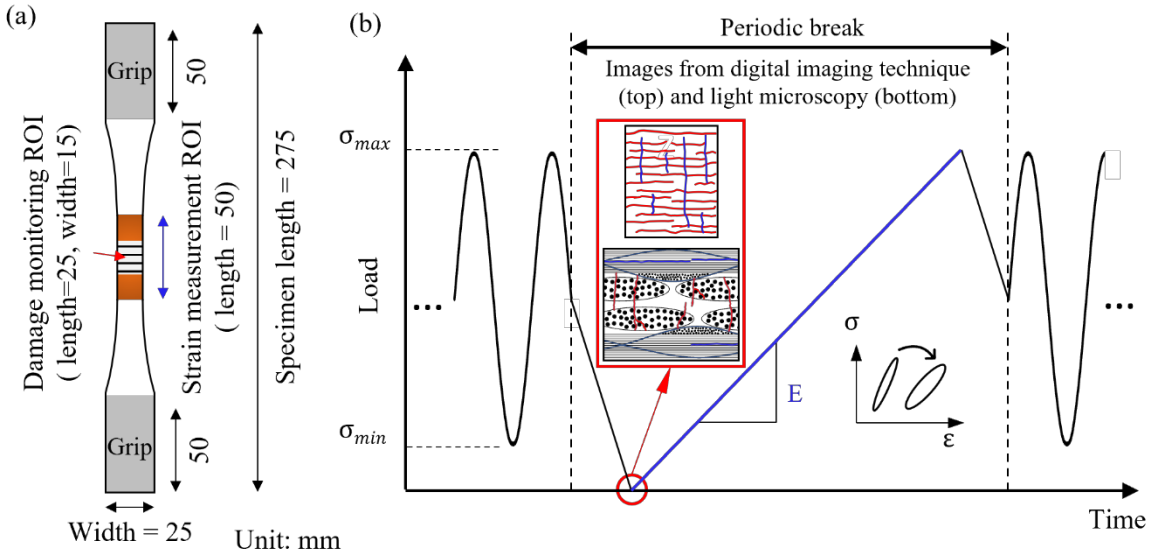


Fig. 4-31. Schematics for: a) specimen geometry and dimension; b) fatigue loading and damage observation profile.

4.4.1.2 Fatigue threshold stepwise cyclic tests

The fatigue threshold of the cross-ply laminate was rapidly determined through additional stepwise tension-tension cyclic tests. A thermographic approach which has proved to be accurate for determining the fatigue threshold of other laminated composite materials [129], [187] was employed. A FLIR A8581 infrared (IR) camera with a pixel resolution of 1280 × 1024 and a temperature sensitivity of <25 mK was used to measure the variation of temperature on the specimen surface during the tests in-situ and in real time. The camera was synchronized with the controller of the MTS 810 test frame via digital trigger and record start signals. Specifically, the camera was configured to capture a thermographic image at the peak stress of each loading cycle to minimize the influence of the thermoelastic effect and ensure that the recorded temperature rises were primarily associated with damage initiation and accumulation. When activated, the IR camera started synchronously upon receiving a trigger pulse from the test frame. The input of the camera was configured to detect a rising-edge 3.3V CMOS logic signal, ensuring precise timing and synchronization. The trigger operates as a purely digital interface, responding only to a transition from low to high (rising edge) rather than a sustained high voltage. The input is buffered and 5V-tolerant, providing voltage protection and compatibility with TTL-level (5V) sources without affecting the internal 3.3V CMOS logic. This ensures robust synchronization and

accurate correlation between the thermal and mechanical data. The dog-bone specimens (Fig. 4-31a) were subjected to a series of cyclic loads (sinusoidal waveform, 5 Hz frequency, stress ratio of 0.1) with increasing maximum stress amplitude (i.e., from 25%UTS up to 70%UTS in 5%UTS intervals) at room temperature conditions. Specimens were loaded for a total of 5,000 cycles under a maximum stress amplitude, followed by a cooldown period. Thereafter, the maximum stress was increased, and the specimen was loaded for an additional 5,000 cycles. This procedure was repeated with the maximum stress amplitude incrementally increasing until the specimen failed. Note, for the material studied 5,000 cycles was sufficient to produce temperature stabilization. A total of three tests were performed using the aforementioned procedure. For each test specimen, the average surface temperature rise at stabilization ($\triangle T_{stab}$), defined as the average temperature increase from the initial temperature to the stabilization temperature at 5000 cycles, for each maximum stress amplitude was plotted against the corresponding maximum stress level and the fatigue threshold was determined according to the method described in Ref.[129].

4.4.1.3 Integrated digital imaging technique developed for fatigue tests

An integrated digital imaging technique was developed to detect damage and capture strains using DIC at different cyclic intervals during fatigue tests, enabling simultaneous monitoring of damage evolution and stiffness degradation for a single test specimen. A synergistic data acquisition system was synchronized with the MTS 810 test frame (Fig. 4-32). A dimmable RGB light source was placed at the back of the clamped specimen to enable the transmission of the light through the center of the gauge region (25 mm × 15 mm, damage monitoring ROI). The transmitted light was then captured by a 5 Megapixel camera with a F2.8/50mm lens positioned in front of the specimen. Two additional LED lamps were placed above and below the digital camera to illuminate the near side if the specimen for light compensation and for improved resolution of damage initiation and growth.

The images were then analyzed automatically to detect crack initiation and evaluate crack density evolution and crack growth using an in-house developed Python@ code based on Gabor filters [25], [26]. The algorithm incorporated a series of image processing steps to ensure accurate damage detection (Fig. 4-33), including (i) image stacking and alignment, which registers all images to compensate for positional shifts and maintain consistent damage detection within the same ROI; (ii) image differentiation, which eliminates constant background features (i.e., surface scratches) by dividing test images by a reference image, enhancing the visibility of developing cracks; (iii) Gabor Filtering, which

applies directionally sensitive filters optimized for specific crack orientations and dimensions; and (iv) thresholding and skeletonization, which binarizes the filtered images and reduces cracks to one-pixel-wide representations that can be analyzed based on length and orientation. The crack density was then calculated from skeletonized images to quantify damage and is defined as the ratio of the total combined crack length to the area of the observation region, Refs [26], [145], [146].

$$\rho = \frac{\sum_{i=1}^{n} L_i}{w \cdot L} \tag{1}$$

where L_i represents the length of the ith crack, n is the total number of cracks, and w and L denote the width and length of the observation region, respectively. Specimens were partially speckled with black on white pattern within the remaining adjacent areas of the gauge region (50 mm × 15 mm, strain measurement ROI) to simultaneously monitor the displacement fields of the specimen and determine strains. Three virtual extensometers with a length of 30 mm were evenly spaced across the specimen width within the gauge region to calculate the averaged strain and determine the specimen stiffness during fatigue testing (Fig. 4-32).

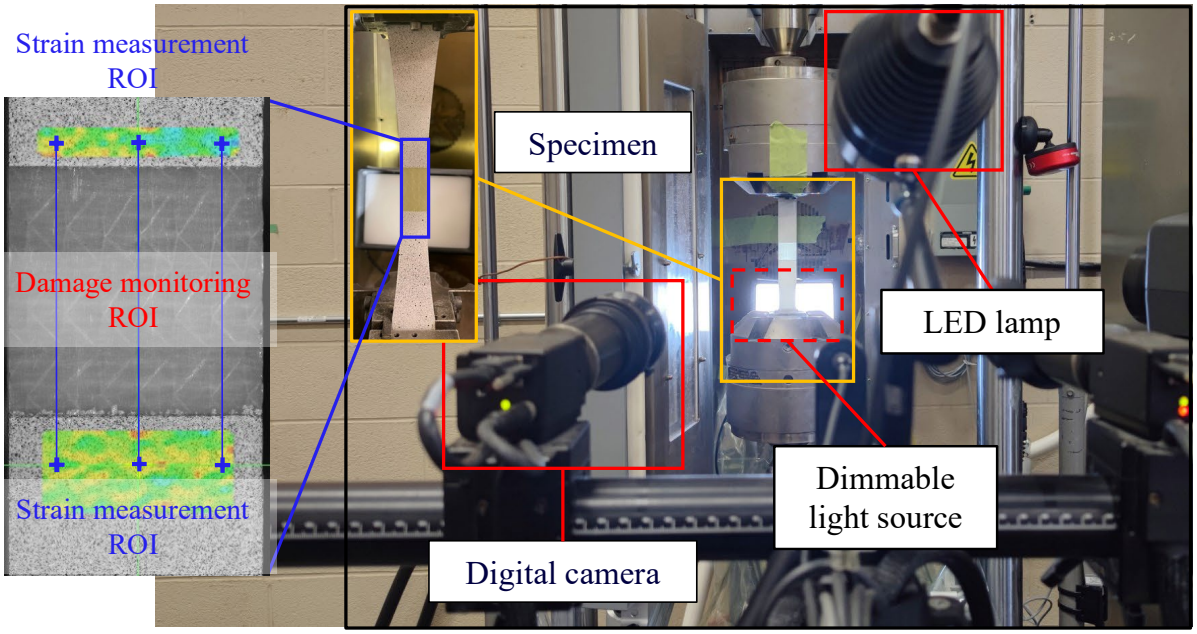


Fig. 4-32. Test setup for use of the integrated digital imaging technique.

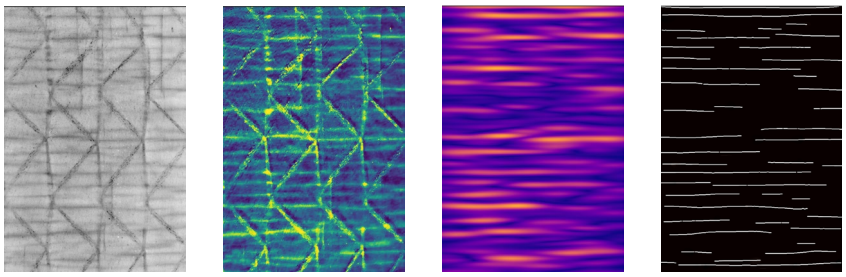


Fig. 4-33. Example of crack counting process.

4.4.2 Verification of integrated digital imaging technique for fatigue testing

Preliminary fatigue tests were performed to verify the accuracy of DIC strain measurements as well as the simultaneous imaging of damage using the experimental setup described in Section 4.4.1.3. A total of six repeated tests were conducted for both fully speckled and partially speckled specimens. Six strain calculation methods were used at predetermined cyclic intervals (Fig. 4-34a), including: (1) the average strain in ROI-1; (2) the average strain in ROI-2; (3) the average strain in ROI-3; (4) virtual extensometer-1; (5) virtual extenometer-3; and (6) the average of virtual extensometers-2, -3, and -4. Normalized longitudinal stiffness degradation calculated using strains from the different strain measurement methods is plotted against the number of cycles for the tests performed with a peak stress of 50% UTS (Fig. 4-34). The main discrepancy of the normalized longitudinal stiffness is observed during the initial 1,000 loading cycles (Fig. 4-34b) where the stiffness values calculated using average strain in ROI-2 and ROI-3 exhibit greater noise when compared to that of ROI-1. The surface areas of ROI-2 and ROI-3 are small compared to that of the entire specimen gauge region; thus, variation in localized damage within these ROIs may be contributing to the discrepancy in the strain measurements and stiffness calculations. A comparison of stiffness degradation curves using virtual extensometers -1 and -3 shown excellent correlation, while the stiffness values calculated from the average of virtual extensometers-2, -3, and -4 exhibit lower noise with good consistency compared to other methods. The virtual extensometers capture the effective change in peak strain during fatigue tests resulting from the diffuse damage evolution over the gauge length considered. Therefore, the averaged strain from three visual extensometers on the partially speckled specimens was used to determine stiffness during subsequent fatigue testing.

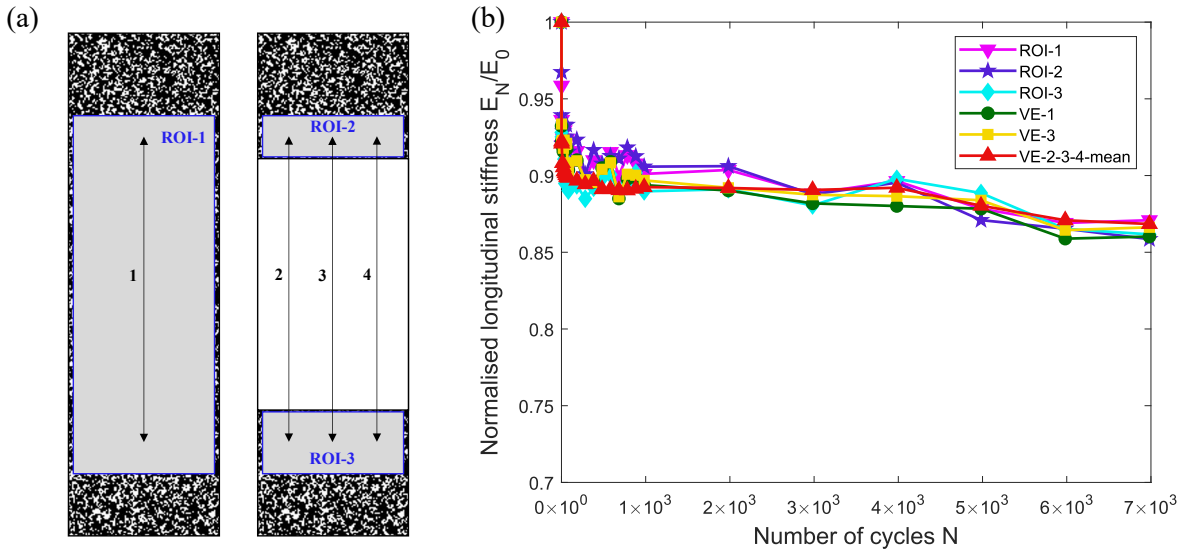


Fig. 4-34. (a) Schematics of strain measurement methods considered for fully speckled and partially speckled specimens, (b) Comparison of normalized longitudinal stiffness degradation curves calculated from average strains in ROIs and virtual extensometers for the fully speckled and partially speckled specimens cyclically loaded in tension-tension at a peak stress of 50%UTS.

The developed integrated digital imaging technique was used to perform preliminary fatigue tests where damage and strain were captured simultaneously. Intralaminar damage modes such as 90° fiber tow cracks were automatically identified in the ROI from the captured surface images using the developed Python@ code (Fig. 4-35a). The length of the automatically detected 90° fiber tow cracks correlated well with the corresponding surface images, which demonstrated the capability of the developed code to accurately detect and identify these cracks. An optical microscope (VHX-5000, Keyence) was employed to inspect damage states on the edge of the same specimen during different cyclic intervals. Prior to any testing, the edges of each specimen were carefully sanded and polished using different size of grit papers (from P180 to P1200) and diamond pastes (3µm and 1µm) with extender fluid. Microscopic results revealed five independent cracks within different 90° fiber tows in the inner two plies of the laminate (region 1 in Fig. 4-35b), which directly correlated with the observed damage using the integrated digital imaging technique (Fig. 4-35a). It should be noted that some closely spaced cracks were detected as a thick dark band (region 2 in Fig. 4-35b). However, this issue could potentially be mitigated by using higher-resolution cameras, while the issue may not occur in laminate with other stacking sequences.

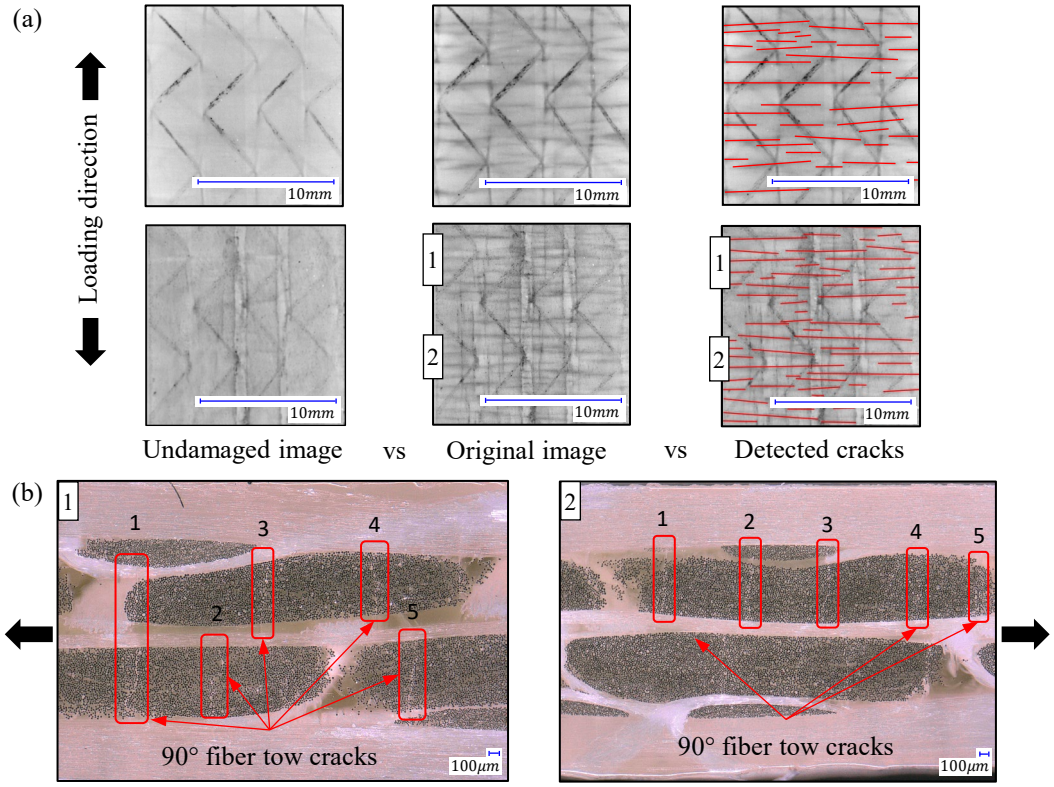
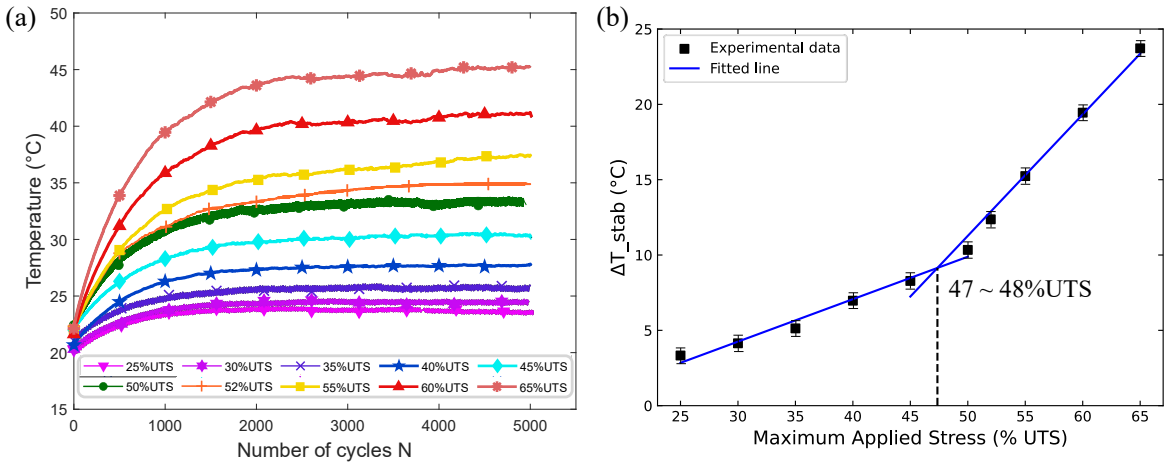


Fig. 4-35. (a) Surface images of two specimens captured prior to testing (undamaged), during a preliminary fatigue test (original image containing damage), and after automated crack identification using the developed digital imaging technique (detected cracks). (b) The corresponding micrograph on the edge of a specimen.

4.4.3 Rapid evaluation of fatigue threshold

The average surface temperature evolution profiles for a representative specimen reveal that temperature stabilized prior to 5,000 loading cycles for all loading intervals considered (Fig. 4-36a), with the exception of when the maximum stress magnitude was 70% UTS where the specimen failed prior to temperature stabilization (not shown). For the loading intervals with a maximum stress amplitude between 25%-45% UTS, the temperature plateaued by 2,000 loading cycles with no observed increase in temperature with further increase in the number of cycles. This result indicates that damage was not advancing at an aggressive rate under these stress levels and/or the temperature rise may be due to the deformation of the resin [129]. A notably larger temperature rise was observed for the cyclic intervals with a maximum stress amplitude of 52%-65% UTS due to the intrinsic energy dissipation

caused by damage evolution. For these tests, a temperature plateau was not strictly achieved as there is a slight temperature rise beyond ~2,000 loading cycles, which indicates stable damage propagation [98],[133]. The specimen failed during the 70% UTS loading interval prior to reaching 5,000 cycles due to accelerated damage growth leading to final failure. The plot of temperature increase at stabilization versus the maximum stress amplitude (Fig. 4-36b) shows the characteristic bilinear shape, revealing greater heat dissipation at higher maximum stresses. The fatigue threshold was therefore determined to be approximately 47–48%UTS. The temperature profiles after stabilization for the indicated maximum stress levels reveal that the temperature was relatively uniform across the specimen surface prior to a peak stress of 45% UTS (Fig. 4-36c), which is close to the fatigue threshold. With further increase of the peak stress, the temperature contour became more nonuniform due to the accelerated development of damage. With the fatigue threshold established, the peak stress levels for the subsequent fatigue tests were selected to be above this threshold to ensure damage initiation and propagation, enabling effective application of the integrated digital imaging technique (Section 4.4.1.3).



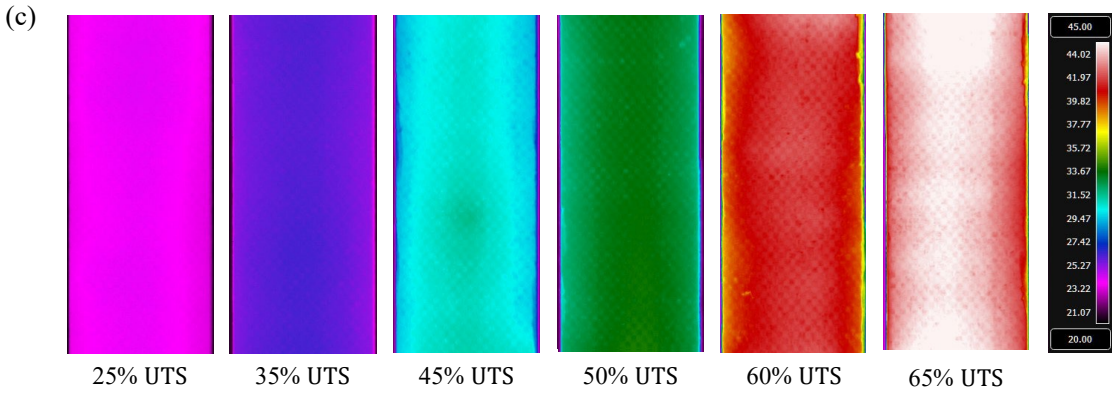


Fig. 4-36. (a) Average surface temperature profile vs. number of cycles at indicated maximum stress magnitudes; (b) increase of average surface temperature after stabilization vs. maximum stress magnitudes; (c) temperature distribution (°C) map after stabilization within the gauge region captured by IR camera.

4.4.4 Damage evolution and stiffness degradation

Two peak stress magnitudes were chosen to assess the damage evolution process and corresponding stiffness degradation under cyclic loading, including 50%UTS (i.e., slightly higher than the fatigue threshold) and 75%UTS. A series of images taken of the surface of representative specimens were directly correlated with the normalized stiffness degradation (Fig. 4-37), where E_0 is the initial stiffness and E_N is the stiffness at the N^{th} cycle.

At a peak cyclic stress of 50%UTS, 90º ply fiber tow cracks were detected during the first loading cycle, which resulted in a rapid decrease in the normalized stiffness from 1.00 to 0.91 (Fig. 4-37). With increasing loading cycles, additional 90º tow cracks developed along the specimen ROI and gradually propagated along the 90º fiber tow direction during the second stage of cyclic loading (i.e., prior to 1,000 cycles). This behavior was characterized by the gradual decrease of the normalized stiffness from 0.92 to 0.89 and a progressive increase of the crack density from 0.85mm^{-1} to 1.10mm^{-1} (Fig. 4-38a). At this stage, the 90º fiber tow cracks propagated at an approximately constant rate (Fig. 4-38b). As 90º tow cracks approached saturation, localized delamination began to appear at the existing crack tips due to stress concentrations (i.e., at 1,050 cycles). During this third stage of cyclic loading, the elastic properties did not significantly degrade during the growth of delamination cracks (i.e., from 1,050 to 4,050 cycles). The above observations are analogous to the experimental results reported by Maragoni et al. [90] and Shen et al. [145] for UD cross-ply laminates. With increasing loading cycles,

delamination cracks propagated at the 0º and 90º fiber tow interfaces along the tow peripheries parallel to the loading direction (i.e., at 49,950 cycles). Moreover, 0º fiber tow pull-out and breakage were observed during the final stage of cyclic loading as a result of the interactions between widespread fiber-matrix debonding and delamination, leading to a significant drop in the longitudinal stiffness and the final failure of the specimen.

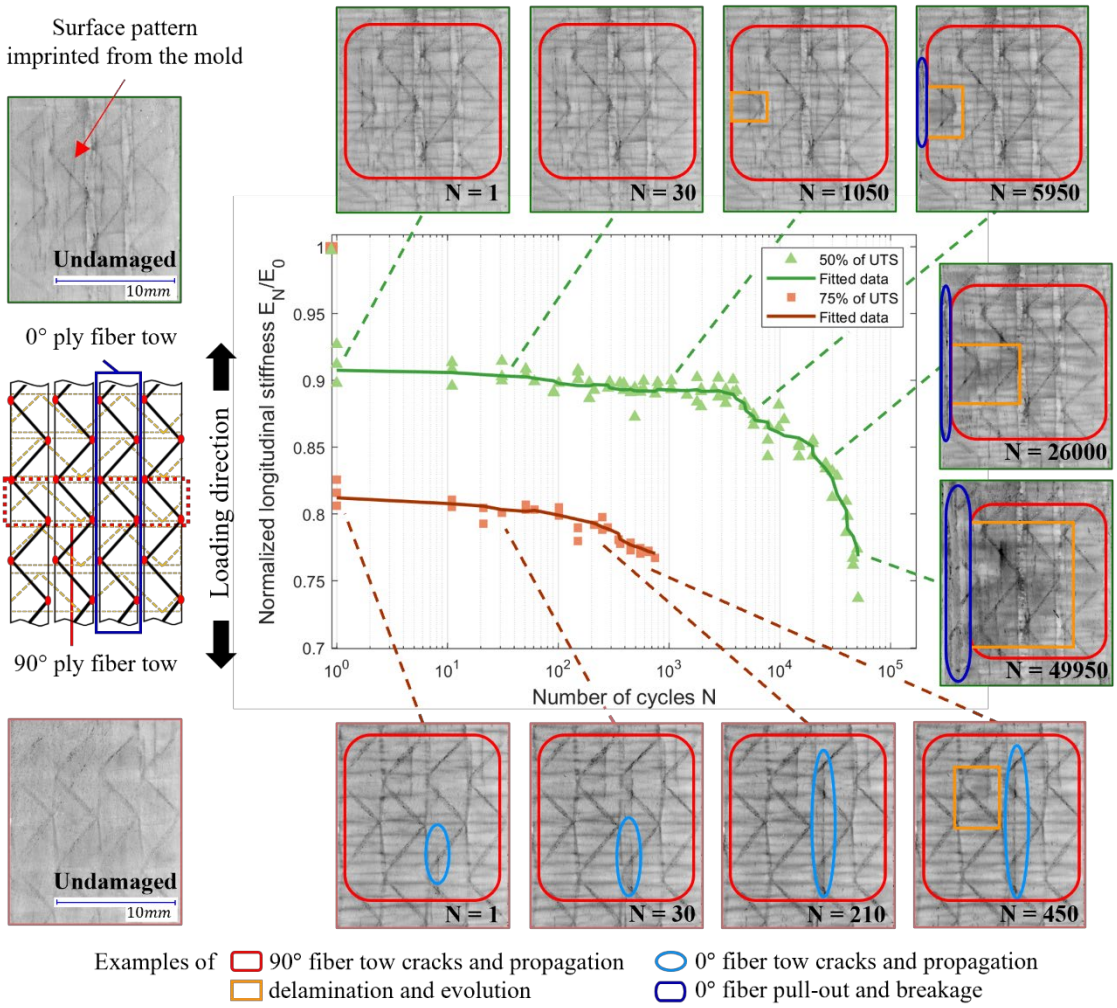


Fig. 4-37. Normalized longitudinal stiffness profiles for indicated peak cyclic stresses and direct correlation with damage evolution at different cyclic intervals. Note, the damage mechanisms automatically identified by the developed code are not identified in the captured images shown for improved clarity.

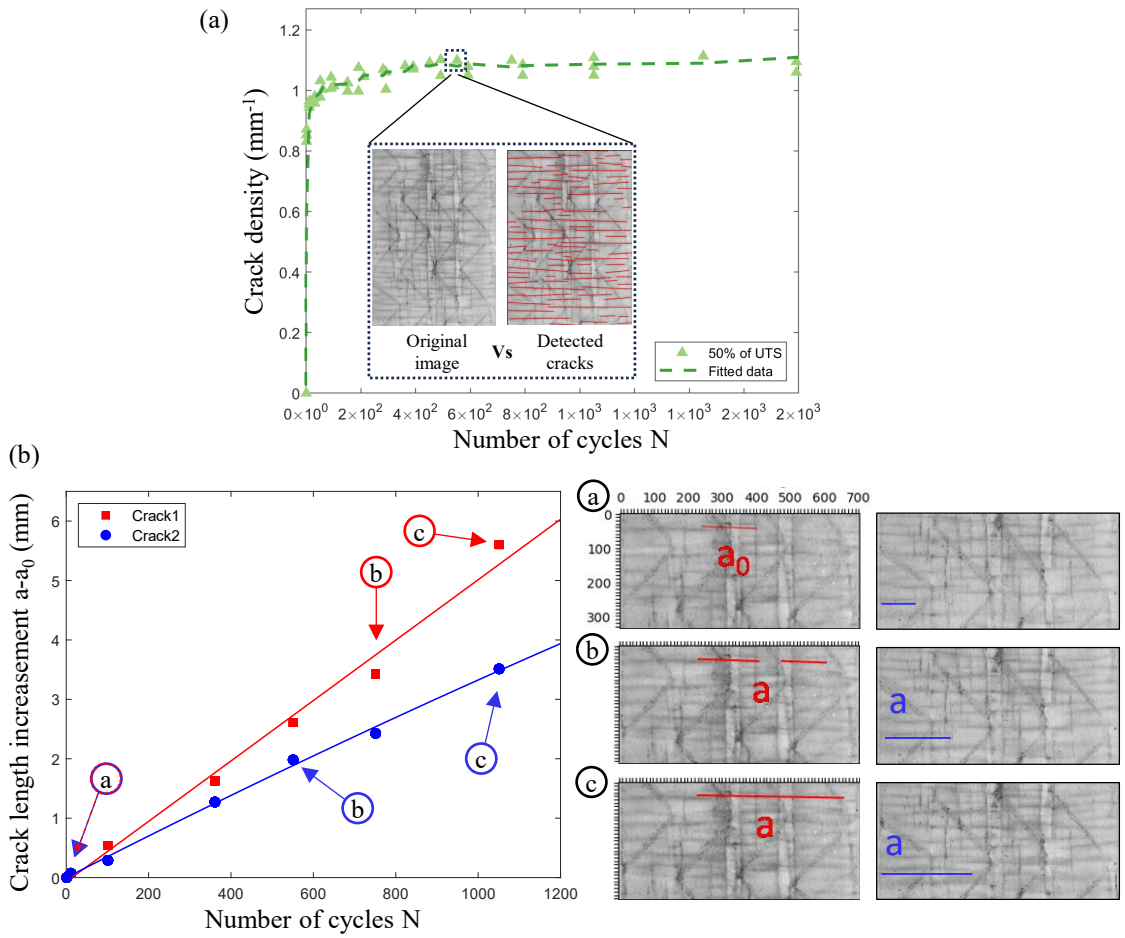


Fig. 4-38. Quantitative damage analysis at 50%UTS: a) 90º tow crack density evolution; (b) representative crack length increasement during fatigue testing for 90° tow cracks (Note that for clear crack visibility purposes, the detected cracks were offset and the axis were labeled in pixels).

At 75%UTS, however, both 0º and 90º fiber tow cracks developed during the first loading cycle, leading to a significant drop (18%) of the normalized stiffness (Fig. 4-37). With increasing loading cycles, the 90º tow cracks saturated quickly after <10% of the total fatigue life (Fig. 4-39) with a lower saturated density compared to the specimens tested at 50%UTS. This result indicates a faster crack growth rate at high stress amplitude, which is analogous to the results reported by Hosoi et al. [188] and Li et al. [94] for UD quasi-isotropic and cross-ply laminates. As 0º fiber tow cracks continued to increase in the regions close to the tips of the developed 90º tow cracks, a gradual decrease of stiffness was observed (i.e., prior to 210 cycles). During this stage, a progressive increase in 0° tow crack length was also observed (Fig. 4-40). With further increase in loading cycles, localized delamination cracks

were observed due to the interactions between the developed 0º and 90º fiber tow interface cracks (i.e., at 450 cycles). Delamination cracks propagated quickly over a brief cyclic interval under a higher magnitude peak stress, which may be attributed to the relatively thin laminate thickness used in this study, as thinner laminates have been shown to inhibit further growth of delamination cracks [92],[189],[190]. The fact that the specimen failed after fewer than 1,000 cycles may have also limited the degree of delamination crack propagation. When cycling at a higher maximum stress amplitude, the growth rate of both 90º fiber tow cracks and delamination cracks was higher. Together with the observed lower saturated 90º tow crack density (Fig. 4-39), these results indicate that there exist significant interactions among the observed damage mechanisms, i.e., 90º tow cracks, 0º tow cracks, and delamination cracks.

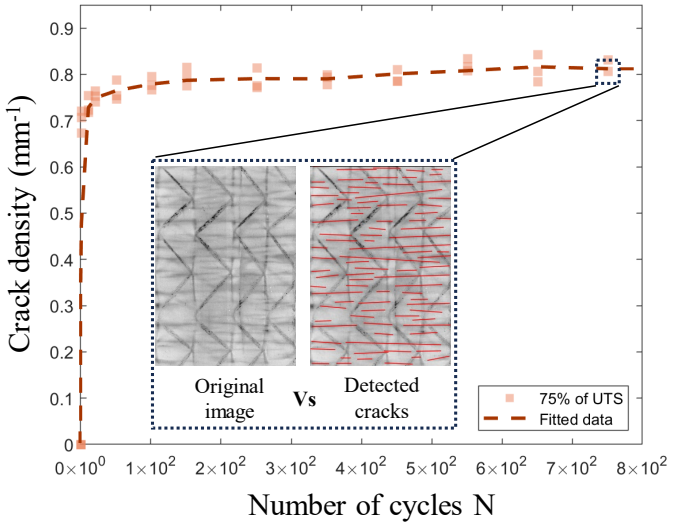


Fig. 4-39. 90º tow crack density evolution at 75%UTS.

Fig. 4-41shows representative microscopic results of observed damage states at different intervals for a specimen cyclically loaded under a peak stress of 50%UTS, with the microstructure of the UD-NCF composite laminate labeled. 90º fiber tow cracks initiated at the stitching sites near the supporting glass fiber yarn regions during the first loading cycle (Fig. 4-41b). The developed cracks were orientated normal to the loading direction throughout the entire thickness of the tow and no delamination was observed at this stage. At 26,000 loading cycles, the additional 90º tow cracks and delamination cracks along the 0º and 90º fiber tow interface that developed during previous loading cycles were observed, which correspond to the dark regions on the surface image (Fig. 4-41c). Note

that during the delamination crack propagation, some branched cracks were also observed in the vicinity of the 0º and 90º fiber tow interface (highlighted with blue arrows in Fig. 4-41c-d) due to the microstructure in the proximity of the tow interface. This phenomenon was also observed during experiments reported in Refs. [23] and [95] and from simulation results reported in Ref. [191]. At 49,950 cycles, localized matrix failure and debris were observed on the specimen edge (Fig. 4-41d). Moreover, 0º fiber pull-out and breakage were evident near the delamination region, indicating the role of delamination propagation in the progressive failure of the 0º fiber tows.

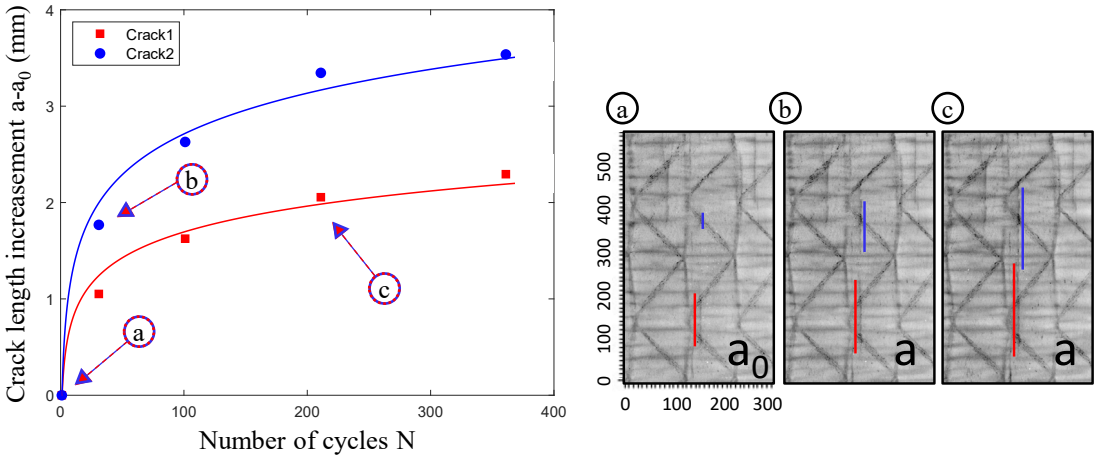


Fig. 4-40. Representative crack length increasement at 75%UTS for 0° tow cracks (Note that for clear crack visibility purposes, the detected cracks were offset and the axis were labeled in pixels).

The developed integrated digital imaging technique was able to effectively identify the evolution of intralaminar damage modes during cyclic loading, including 90° and 0° fiber tow cracks (Fig. 4-38-Fig. 4-40). While the technique has not yet been developed to identify delamination cracks, its ability to identify the evolution of tow crack density and crack length increasement during the latter stages of cyclic loading (i.e., in the presence of delamination cracks) was not hindered. Moreover, for the peak cyclic stresses considered in this study, the tow crack density reached saturation prior to the onset of delamination cracks (Fig. 4-37). Thus, the presented results would not be influenced by the existence of delamination cracks and are deemed to be reliable.

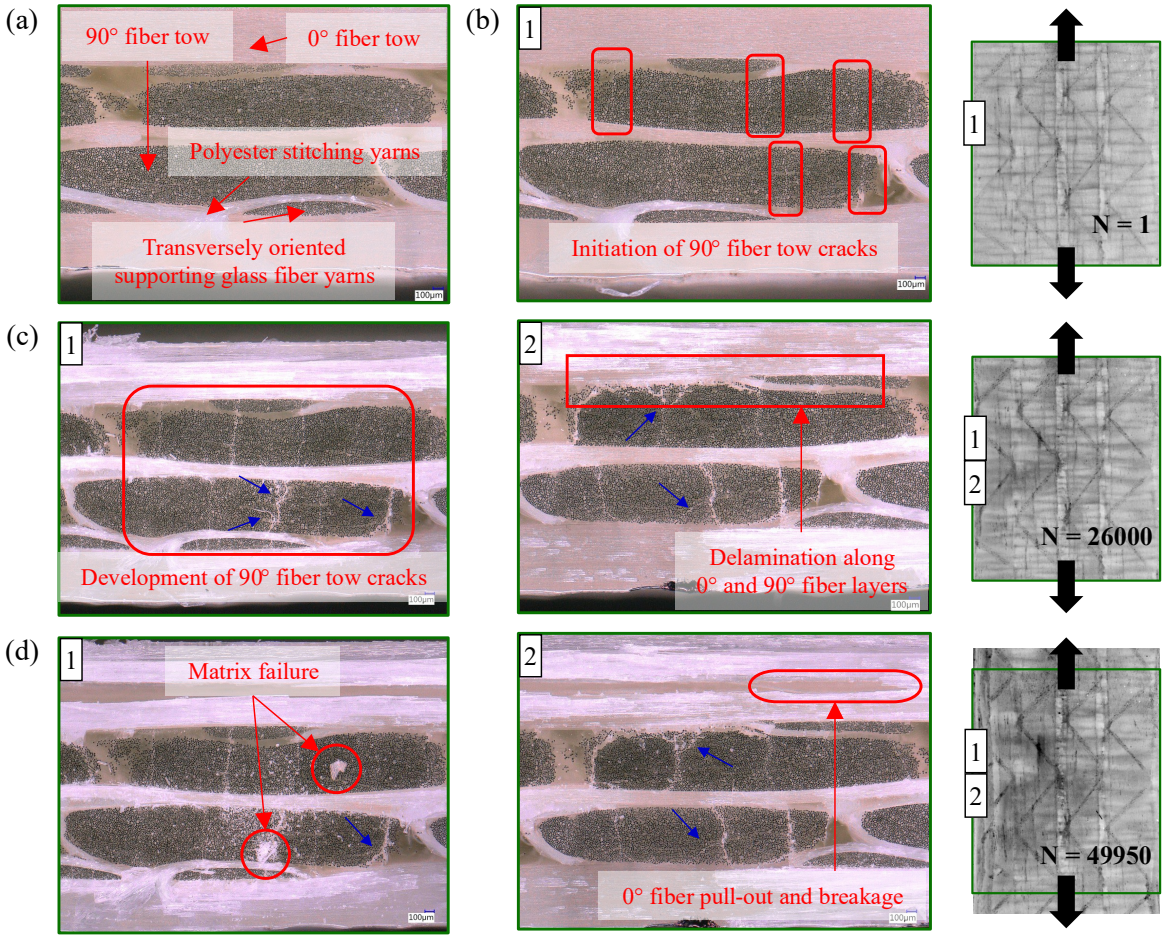


Fig. 4-41. Microscopic observation of specimen edge damage at different cyclic intervals under a peak stress of 50%UTS with corresponding surface images: (a) undamaged specimen; (b) 1 cycle; (c) 26,000 cycles; (d) 49,950 cycles.

4.5 Task 4: Development of A Deep Learning-based CNN Model for Damage Characterization in UD-NCF composites

An integrated deep learning-based CNN model combined with automated crack counting algorithms was developed to characterize damage in UD-NCF glass fiber/reactive thermoplastic (NCF GF/acrylic) cross-ply laminates subjected to both quasi-static tensile and tension-tension cyclic loading. Digital images obtained from Task2 at -50°C (Section 4.3) were preprocessed and annotated. Six classes of features were defined in the images based on experimental observations, and the annotated images were divided into training and testing sets. The U-Net architecture, incorporating skip connection, dropout, and weighted Dice loss, were selected to train and evaluate the model under various hyperparameters, including batch size, class weights, and the number of epochs. The optimal model with pertained weights and tuned hypermeters were then applied to detect damage across the entire dataset. Both qualitative and quantitative validations were performed to assess the model's performance under both loading conditions.

4.5.1 Methodology

4.5.1.1 Image preprocessing and annotation

A series of images captured using the developed digital imaging technique (see Section 4.3.1.2 for details) were imported into Python and structured as stacked NumPy arrays. This approach provided a compact and efficient format for image data representation, enabling sophisticated image analysis and machine learning applications [192]. The histograms of the captured images were analyzed and revealed a high frequency at low pixel values (≈ 0), corresponding to pure black regions at the left and right margins (Fig. 4-42a). To enhance the focus on relevant features, the images were cropped at the center, defining a ROI with dimensions of 700 pixels in height and 650 pixels in width (Fig. 4-42b). The histograms of the cropped images exhibited a more balanced pixel value distribution resembling a normal distribution, which indicates the images were of sufficient quality for subsequent analysis. To ensure consistent damage monitoring within the ROI, image shift correction was performed iteratively by calculating and adjusting shifts. The process began by computing the cumulative shift for each image using phase correlation in the Fourier domain, which identifies the relative displacement between consecutive images with sub-pixel accuracy [193], [194]. These cumulative shifts were then used to geometrically transform each image back to the coordinate system of the first image, ensuring precise alignment. Residual shifts were corrected over multiple iterations, and all images were uniformly

cropped to maintain consistent dimensions. Refer to Fig. 4-42b and Fig. 4-42c for a comparison between the first and last images in the image stack.

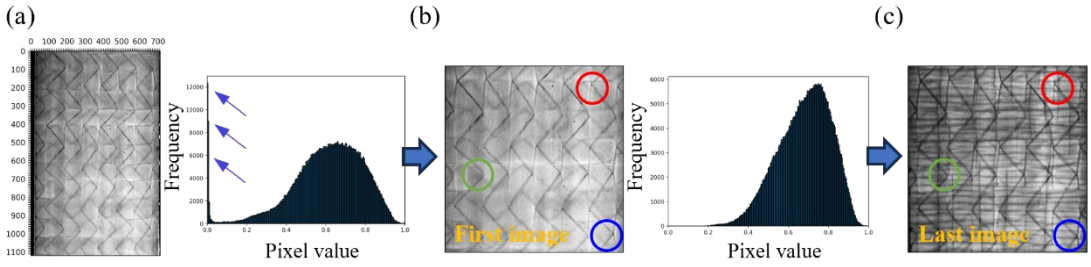


Fig. 4-42. Image preprocessing process: (a) initial image captured using the digital imaging technique with its histogram; (b) image ROI and its histogram; (c) image shift correction to ensure consistent damage monitoring within ROI (examples of stitching loops are circled in the first and last images for comparison).

Out of 108 preprocessed images, 28 were selected at consistent intervals and imported into Computer Vision Annotation Tool (CVAT) for labeling and annotation [195]. Six distinct classes of features were defined based on experimental observation (Section 4.3.3): 90° tow cracks (Class 1), 0° tow cracks (Class 2), 90° stitching yarns (Class 3), 0° stitching yarns (Class 4), laminate surface imprints (Class 5), and background (Class 6). Each image was manually annotated and cross-checked at the pixel level for each class to ensure the creation of high-quality ground truth data (Fig. 4-43a, b). Corresponding masks were subsequently generated for each class, providing essential input for the training process (Fig. 4-43c).

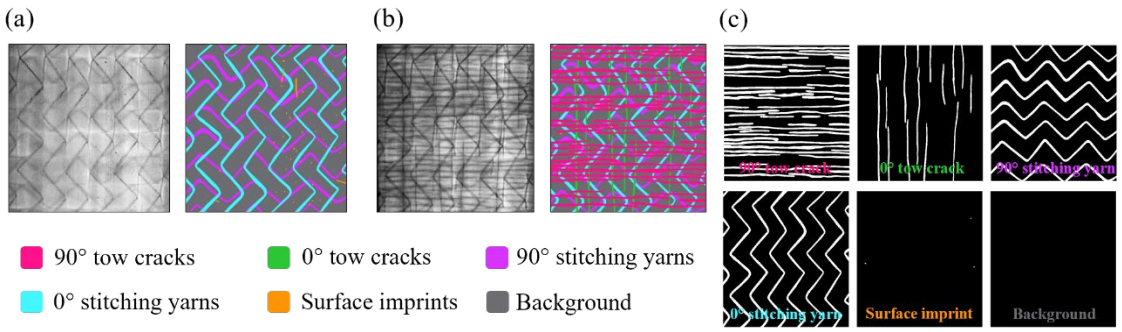


Fig. 4-43. Examples of image annotation in CVAT: (a) the first image with its annotation; (b) the last image with its annotation; (c) masks for different classes.

4.5.1.2 Training and testing sets

A custom dataset splitting approach in PyTorch was employed to partition the image dataset into training and testing sets based on specific index ranges. This approach ensured that both training and testing sets contained examples representing all damage states at various applied stress levels (Fig. 4-28). Three index groups were defined: 1-10 (i.e., early damage stages, Fig. 4-44a) , 11-20 (i.e., damage progression, Fig. 4-44b), and 21-28 (i.e., later damage stages, Fig. 4-44c). For each index range, a subset of the dataset was created and subsequently divided into training and testing sets in a 70:30 ratio, ensuring random distribution within the specified range. As a result, the training and testing set comprised 19 and 9 examples, respectively.

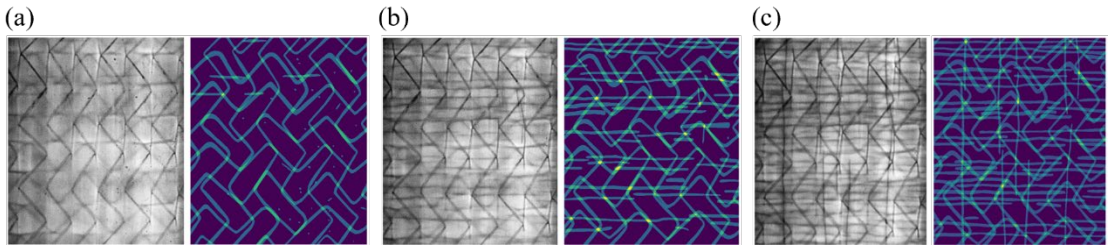


Fig. 4-44. Examples of images and their corresponding masks in the testing set at: (a) first index group; (b) second index group; (c) third index group.

4.5.1.3 Dice coefficient and weighted Dice loss function

The Dice coefficient has been widely employed as a per-class metric to evaluate the quality of pixel-wise predictions in multi-class segmentation tasks [161], [164], [196]. It quantifies the similarity between predicted segmentations and ground truth labels, and is given by:

$$Dice\ coefficient = \frac{(2 \times |P \cap G|)}{(|P| + |G| + \epsilon)} \tag{3}$$

where $|P \cap G|$represents the overlap of predictions and ground truth for a given class, $|P| + |G|$ denotes the sum of predicted and ground truth pixels for that class, and ϵ is a small constant added to prevent division by zero.

The weighted Dice loss was employed as the objective function during the training process, as defined in Eq (4). This choice was motivated by two key reasons. First, it allows the prioritization of critical classes, such as 90° tow cracks (Class 1), while reducing emphasis on less important classes, such as laminate surface imprints and background. This ensures that the model focuses on accurately

predicting essential features. Second, it addresses the issue of class imbalance, particularly in the early stages of loading, where damage is minimal and accounts for only a small portion of the image compared to other classes, such as stitching yarns (Class 3 and Class 4) and background (Class 6). Without weighting, the model might achieve a high overall Dice score by focusing on the majority classes (e.g., background) while neglecting the minority but important classes (e.g., 90° tow cracks).

$$Weighted\ Dice\ Loss = 1 - Weighted\ Mean\ Dice\ Coefficient \quad (4)$$

where the weighted mean Dice coefficient represents the Dice coefficient averaged across all classes, with each class assigned a weight proportional to its importance. To implement class weights, a weight vector (e.g., [211100]) was defined where each value corresponds to a specific class with higher values assigned to critical classes and lower values to less important ones. To ensure the sum of weights equals to 1, the weights were normalized by dividing the total sum of the vector before computing the weighted mean dice coefficient, see Section 4.5.1.5 for more implementation details.

4.5.1.4 U-Net architecture

U-Net architecture was employed to segment various damage classes in this study (Fig. 4-45). The choice of U-Net was motivated by its proven effectiveness and computational efficiency in biomedical and materials image segmentation tasks where datasets are limited in size, and feature localization is critical [197]. Unlike more complex architectures such as TransUNet or Swin-UNet, which rely on transformer-based modules and attention mechanisms and require large datasets and substantial computational resources, U-Net offers a better balance between accuracy and training efficiency, making it suitable for this study. The model comprised two primary components: the encoder (down-sampling) and the decoder (up-sampling), connected by a central bottleneck. Skip connections were integrated to retain spatial information and enhance localization accuracy by transferring features from the encoder to the decoder [161]. Additionally, dropout regularization was applied throughout the network to mitigate overfitting (Fig. 4-45), which is considered beneficial when the training dataset is small and imbalanced [197].

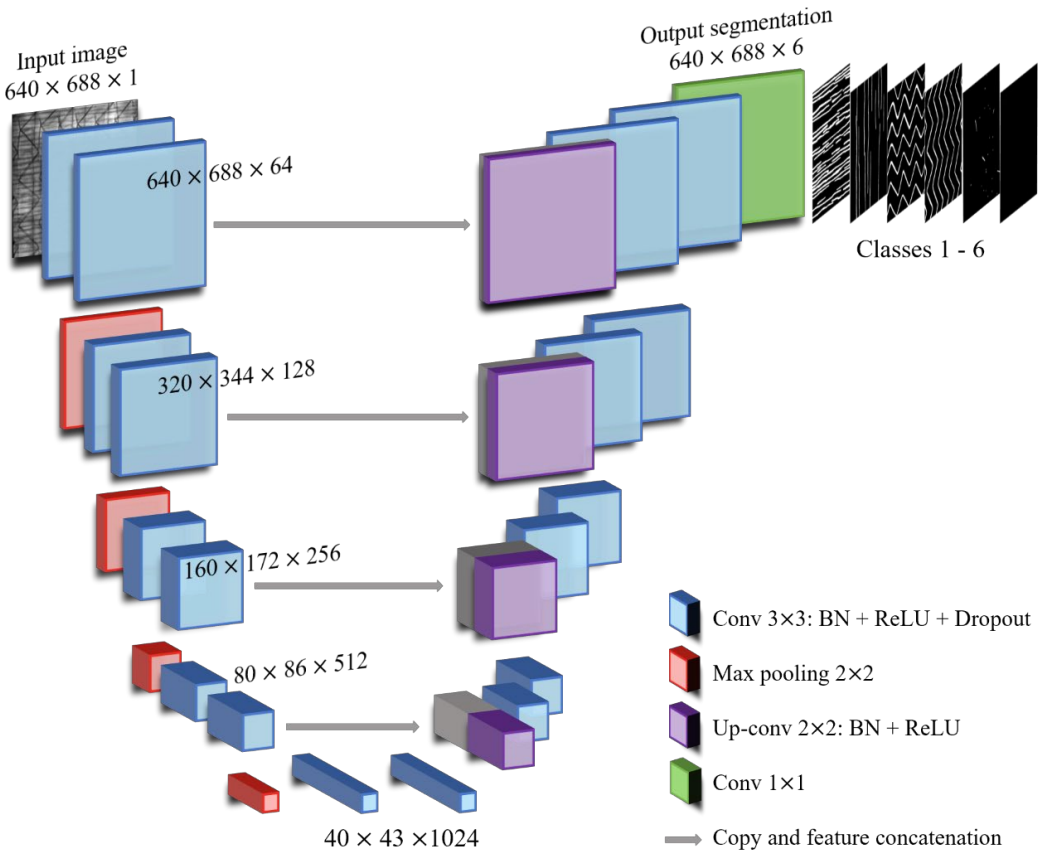


Fig. 4-45. U-Net architecture with the implementation of dropout regularization.

The encoder consisted of four sequential blocks with spatial dimensions (width and height) reduced at the end of each block by applying 2×2 max polling along the down-sampling paths. Each level comprised two convolutional layers with a kernel size of 3×3, followed by batch normalization, ReLU activation, and dropout (probability=0.1). During the training process, augmented images sized 640×688 pixels with a single channel were used as input. The augmentation process introduced variability through transformations such as vertical and horizontal flips (probability=0.5), random rotations (limit =1° with probability=0.5), and random cropping (width=640, height=688, probability=1.0). These augmentations simulated real-world scenarios, expanded the dataset, and improved model robustness. The first block processed the single-channel input image to generate 64 feature maps, with subsequent blocks sequentially doubling the number of channels from 64 to 128, 256, and ultimately 512.

The bottleneck layer acted as a bridge between the encoder and decoder. It consisted of two convolutional layers with 1024 feature channels, followed by batch normalization, ReLU activation, and dropout. This layer captured the most abstract and high-level features of the input image, providing a critical foundation for the subsequent reconstruction of spatial dimensions in the decoder.

The decoder reconstructed the spatial dimensions of the image, aiming to restore the pixel-wise segmentation map through a sequence of up-sampling paths. Each level comprised two convolutional layers with the same structure as those in the encoder. Up-sampling was achieved through transposed convolutional layers, which increased the spatial dimensions while progressively reducing the number of channels from 1024 to 512, 256, 128, and finally 64. Skip connections were used to concatenate features from the encoder to the corresponding decoder block. This integration enabled the network to leverage both high-level semantic information from the bottleneck and low-level spatial details from the encoder, thereby improving segmentation accuracy [161].

The final convolutional layer reduced the number of feature maps to match the desired number of output classes (six in this study). A 1×1 kernel was employed to enable pixel-level classification for each class. The output of this layer was subsequently processed through SoftMax function which calculated the class probabilities for each pixel in the input image.

4.5.1.5 Training and testing the model

A set of hyperparameters, including batch size (BS), class weights, and epochs, were employed to train the model and optimize its performance, as summarized in Table 4-8. The Adam optimizer with a learning rate of 1×10^{-4} was employed for all experiments. All training was conducted on an NVIDIA GeForce RTX 4070 Ti SUPER White OC Edition Gaming Graphics Card, providing efficient computational performance and rapid iteration. It is worth noting that overlaps between different classes were observed (Fig. 4-43 and Fig. 4-44). To prioritize specific classes, such as 90° tow cracks, zero weights were assigned to some classes such as those for the 2nd class (0° tow cracks) in Table 4-8.

Table 4-8. Summary of training hyperparameters used in the experiments.

Hyperparameters	Values
Batch size	BS-1, BS-3, BS-5, BS-7
Class weights	[111111], [211111], [201111], [401111], [601111], [801111]
Epochs	From 1 to 400, at intervals of 2

The same testing set, without transformations, was utilized to evaluate the pretrained models. The optimal model was selected based on its performance and applied to detect damage across the entire dataset. The resulting segmentation masks were subsequently integrated with automated crack counting algorithms for cracking counting, as described in Section 4.5.1.6.

4.5.1.6 Crack counting

A list of binary masks for 90° tow cracks (Class 1) segmented by the selected model was skeletonized to a single-pixel width (Fig. 4-46). Crack density (ρ) was subsequently calculated to quantify the damage state under applied stresses (see Section 4.3.4 for details).

To implement this equation in the algorithm, the total crack length in the mask (numerator of Eq. (1)) was calculated by summing the number of non-zero pixels. This value was then divided by the total number of pixels in the observation region (denominator of Eq. (1)), resulting in a unit of 1/pixel. Finally, ρ was converted to 1/mm by multiplying the actual pixel size of 41.67 pixels/mm, as determined experimentally.

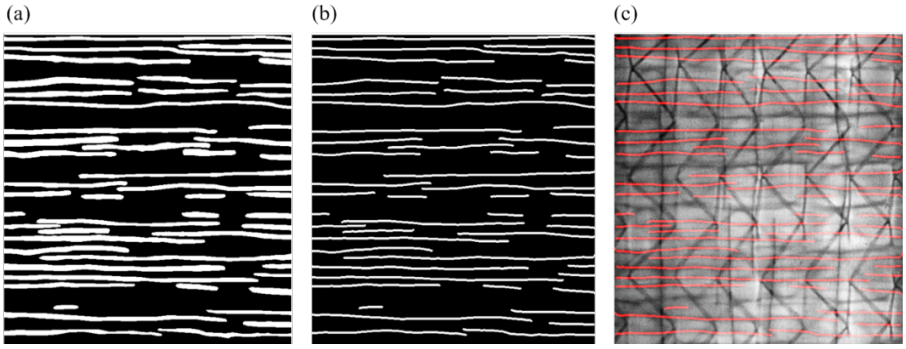


Fig. 4-46. Crack counting process (zoomed-in view): (a) segmented mask example for Class 1; (b) skeletonization to achieve uniform width for crack counting; (c) overlay of the skeletonized mask on the image for visualization.

4.5.2 Effect of batch sizes on characterization results

The impact of different batch sizes on the training process was evaluated using the weighted Dice loss, mean Dice coefficients for Classes 1-4, and as Dice coefficient for Class 1 (Fig. 4-47). Laminate surface imprints (Class 5) and background (Class 6) were excluded from the calculation of the mean Dice coefficient as these classes were deemed less significant.

The convergence of the weighted Dice loss (Fig. 4-47a) over 400 epochs revealed that smaller batch sizes achieved lower loss values (~0.886 for BS-1 and ~0.887 for BS-3) compared to larger batch sizes (> 0.890 for BS-5 and BS-7). A similar trend was observed in the mean Dice coefficient (Fig. 4-47b) where BS-1 achieved the highest value (~0.739) throughout the training epochs. In contrast, BS-5 and BS-7 converged more slowly and exhibited lower mean Dice coefficients (~0.731 and ~0.718, respectively). The Dice coefficient for 90° tow cracks (Class 1) further highlighted the superiority of smaller batch sizes (Fig. 4-47c) with BS-1 and BS-3 achieving higher segmentation accuracy for Class 1 (~0.740 for smaller batch sizes versus ~0.720 for larger batch sizes, respectively). BS-1 consistently exhibited lower loss, higher mean Dice coefficients and higher Dice coefficients for Class 1. Consequently, it was selected for further hyperparameter tuning. While smaller batch sizes may incur higher computational costs due to more frequent gradient updates, the improved performance observed in the study justifies this trade-off.

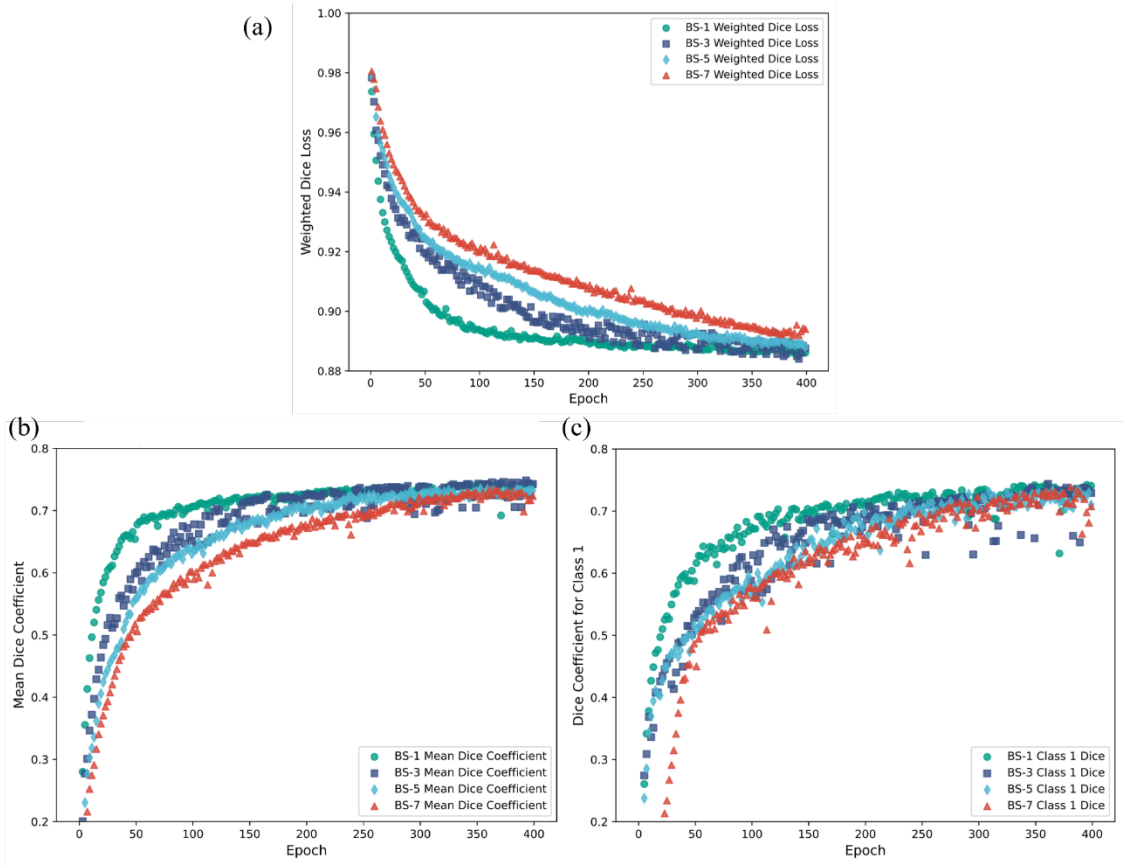


Fig. 4-47. Effect of batch size on the training process: (a) weighted Dice loss over epochs; (b) mean Dice coefficient (Class 1 to Class 4) over epochs; (c) Dice coefficient for Class 1 over epochs.

4.5.3 Effect of weights on characterization results

The effect of different class weight configurations on the training process was evaluated using the weighted Dice loss, mean Dice coefficients for Classes 1, 3, and 4, and the Dice coefficient for Class 1 (Fig. 4-48). The 2nd class (0° tow cracks) was excluded from the mean Dice coefficient calculation to prioritize the accurate segmentation of 90° tow cracks and mitigate the influence of overlap between 90° and 0° tow cracks (further details are provided in subsequent paragraphs). Conversely, both 90° and 0° stitching yarns were included to facilitate the identification of damage initiation and propagation locations.

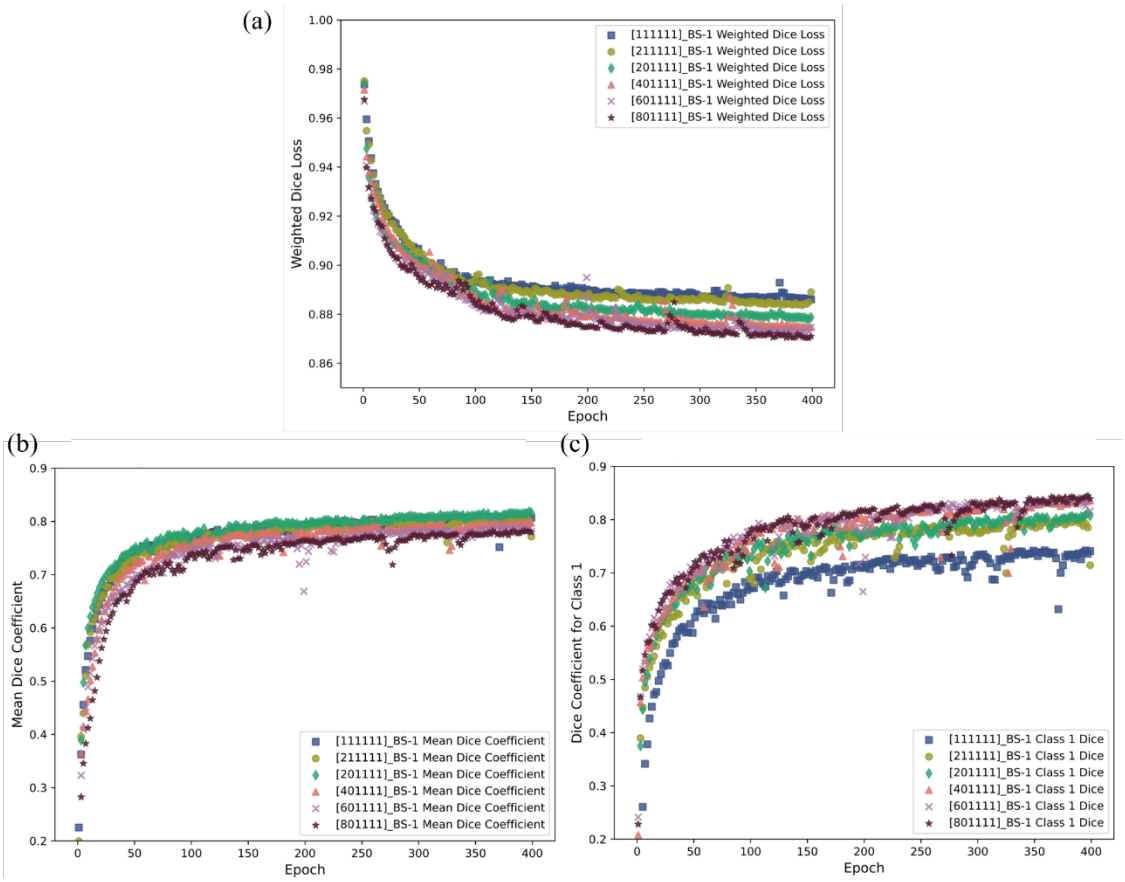


Fig. 4-48. Effect of different class weights on the training process: (a) weighted Dice loss over epochs; (b) mean Dice coefficient (Class 1, Class3, and Class4) over epochs; (c) Dice coefficient for Class 1 over epochs.

The convergence of the weighted Dice loss (Fig. 4-48a) over 400 epochs demonstrated that higher emphasis on Class 1, particularly with weight configurations [801111] and [601111], resulted in lower

Dice loss values (~0.871 and ~0.874, respectively), outperforming the balanced weights [111111] (~0.887). However, slightly lower mean Dice coefficients were observed for weight configurations [801111] and [601111] compared to others (Fig. 4-48b). This was expected, as assigning higher weights to Class 1 reduces the emphasis of other classes, leading to a slight decrease in the mean Dice coefficients. The Dice coefficient for Class 1 underscored the importance of assigning class weights to enhance segmentation results for critical classes (Fig. 4-48c). The Dice coefficient improved significantly from ~0.736 for balanced weights [11111] to ~0.840 for highly biased weights [801111], with minimal difference between weights configurations [801111] and [601111]. Other configurations, such as weights [201111], converged more slowly and achieved lower Dice coefficients (~0.808) compared to weights [601111] (~0.836).

To better understand the effects of assigning zero weight to specific classes on model predictions, two weight configurations ([211111] and [201111]) were compared against the ground truth (Fig. 4-48a). When a non-zero weight was assigned to Class 2 (0° tow cracks), the model accurately classified these cracks, but the corresponding segmentations for Class 1 (90° tow cracks) were incomplete (as indicated by red arrows in Fig. 4-48b). Conversely, assigning zero weight to Class 2 allowed the model to accurately identified 90° tow cracks, although some overfitting was evident at 400 epochs (Fig. 4-48c). Assigning zero weight to Class 2 did not introduce bias in this context, as the damage classes (Class 1 and Class 2) partially overlap and share pixels at their intersections (Fig. 4-43b). In these regions, features from both classes were present, enabling the model to continue learning shared representations despite the exclusion of one class from the loss function. Moreover, 90° tow cracks exhibited consistent propagation along the fiber direction, resulting in more spatially coherent and distinguishable patterns. This characteristic further supports the model's ability to effectively learn

and segment Class 1 features when Class 2 is temporarily excluded from training.

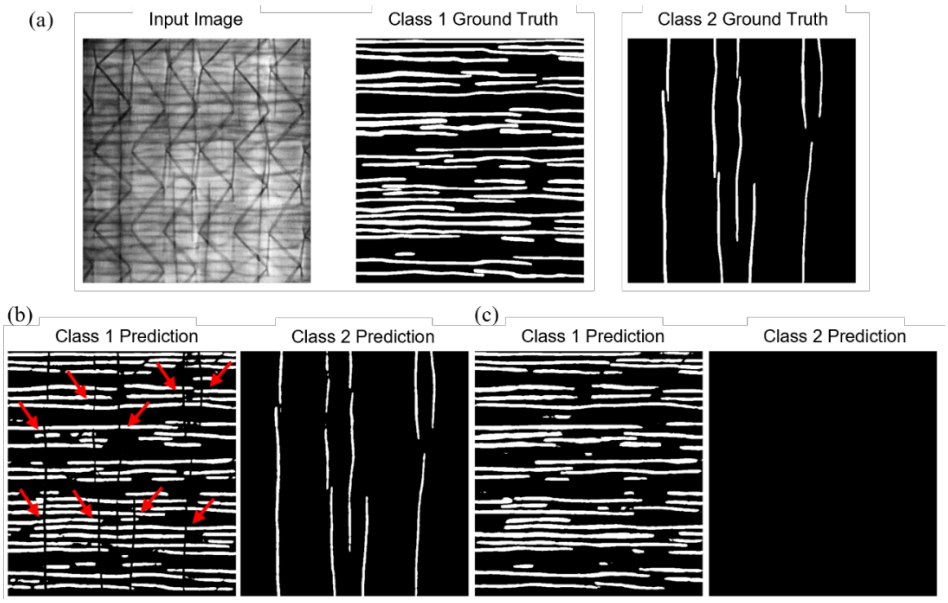


Fig. 4-49. Visualization of the effect of different class weight configurations on model segmentation results: (a) raw input image with ground truth labels for Class 1 and Class 2; (b) segmented results using weight configuration [211111]; (c) segmented results using weight configuration [201111].

The results emphasized that assigning higher weights to Class 1 improves segmentation accuracy for this critical class and effectively reduces the weighted Dice loss. However, higher class weights can slightly impact the segmentation of other classes, as observed in the mean Dice coefficient (Fig. 4-48b). To balance between prioritizing Class 1 and maintaining reasonable segmentation accuracy across other classes, class weight configuration [601111] was selected for further hyperparameter tuning.

4.5.4 Effects of epochs on characterization results

Two metrics were utilized to determine the optimal epoch by analyzing the convergence of the weighted Dice loss and the comparison of the Dice coefficient for Class 1 during training and testing (Fig. 4-50). The model configured with BS-1 and weights [601111] was trained over 400 epochs with periodic evaluations conducted on the same testing set at intervals of two epochs.

The testing weighted Dice loss stabilized after approximately 150 epochs, reaching a minimum value of ~0.885, indicating reduced segmentation errors and improved generalization (Fig. 4-50a). After 150 epochs, the training weighted Dice loss continued to decrease slightly, leading to a gradual widening of the gap between the training and testing curves. The minimum difference between the training and

testing weighted Dice loss was less than 0.016% and observed at 156 epochs (marked as 1 in Fig. 4-50a). This epoch was identified as the point of optimal balance between training and testing performance, where overfitting was minimized.

A detailed evaluation of the Dice coefficient for Class 1 on the training and testing sets over epochs ranging from 150 to 350 further supported this observation (Fig. 4-50b). After 150 epochs, no significant improvement in the testing Dice coefficient for Class 1 was observed, and fluctuations in testing performance became apparent, suggesting potential overfitting. At 156 epochs, the Class 1 Dice coefficients on the training and testing sets were ~0.800 and ~0.795, respectively, with a minimal difference of less than 0.52% (marked as 1 in Fig. 4-50b). In contrast, while the training Dice coefficient for Class 1 increased to ~0.824 at 292 epochs, the difference between the training and testing Class 1 Dice coefficients increased significantly to ~2.96% (marked as 2 in Fig. 4-50b), indicating overfitting at later stages.

Thus, the model at 156 epochs was determined as optimal and was subsequently used for experimental validation on the entire dataset, see Section 4.5.5 for details. Refer to Fig. 4-51 for visualization examples comparing the raw input image, ground truth annotations, and segmented results for Class 1.

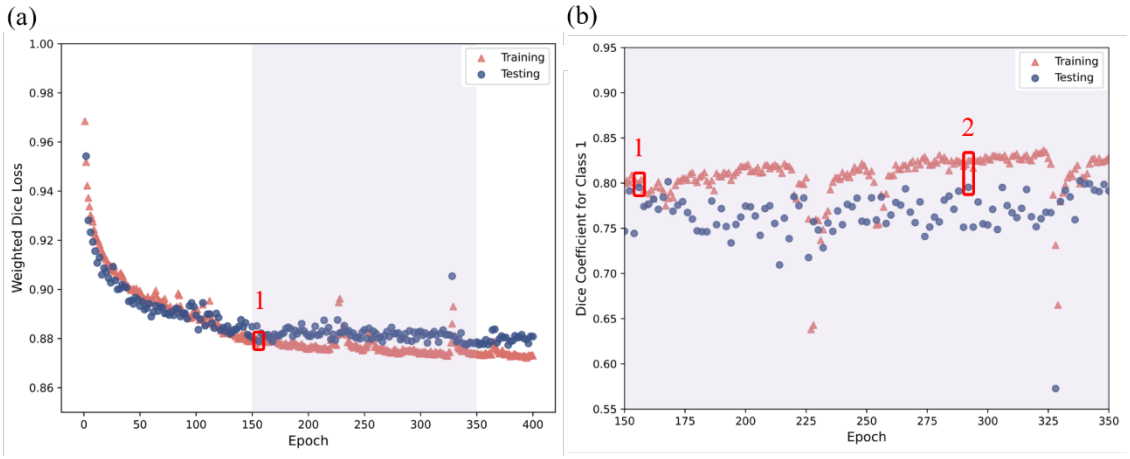


Fig. 4-50. Effect of epochs on training and testing performance: (a) comparison of training and testing weighted Dice loss over epochs; (b) comparison of training and testing Dice coefficient for Class 1 over epochs.

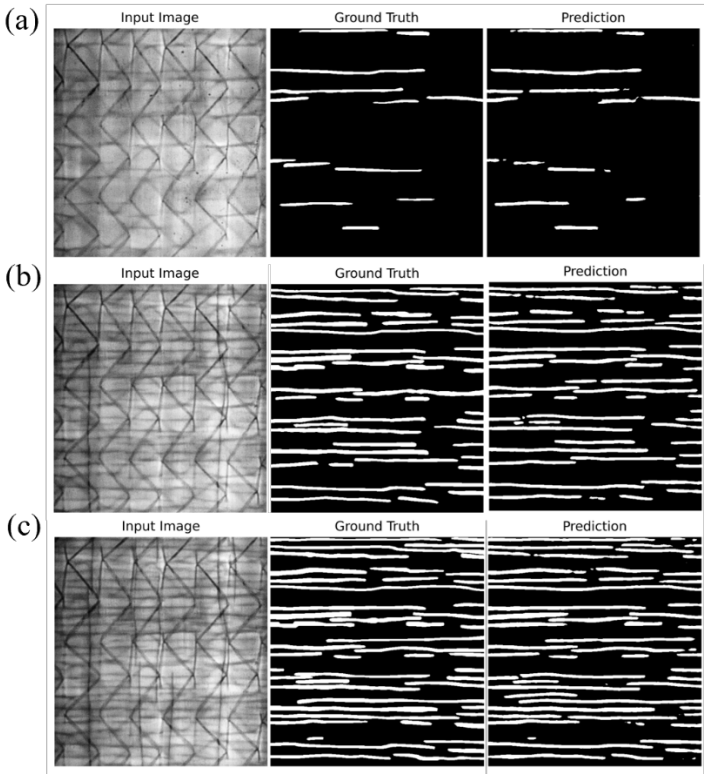


Fig. 4-51. Visualization of model segmentation results in different index groups: (a) representative example from the first index group; (b) representative example from the second index group; (c) representative example from the third index group.

4.5.5 Experimental validation on the entire dataset

Both qualitative and quantitative validations were performed to comprehensively evaluate the capability of the model in damage classification and quantification. This included identifying the location of damage initiation, tracking damage progression and interaction, and counting crack density evolution under quasi-static and fatigue loading conditions. Images captured using the developed digital imaging technique served as inputs to the optimized model, which incorporated pretrained weights and fine-tuned hyperparameters.

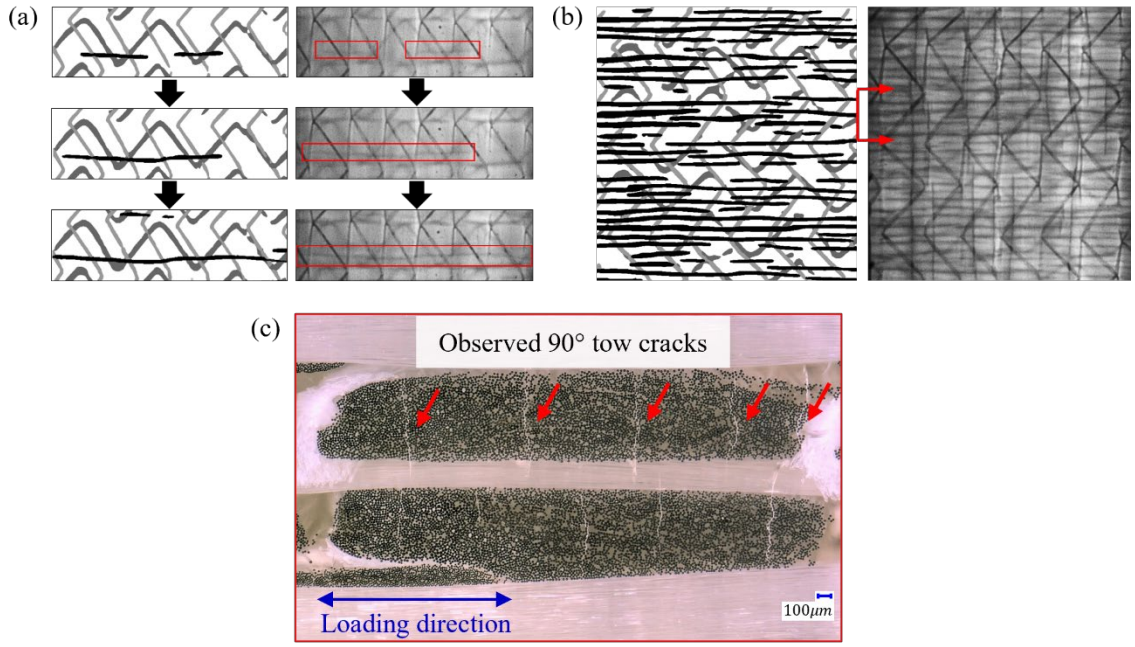


Fig. 4-52. Comparison and validation of segmented and actual 90° tow cracks (Class 1) under quasi-static tensile loading at -50°C: (a) example of crack initiation and evolution within 90° glass fiber tow (generated image on left); (b) crack development and interaction at ~429MPa (generated image on left); (c) microscope observation at the indicated location for validation.

A total of 108 images obtained from quasi-static tensile loading at -50°C and 40 images from tension-tension cyclic loading at 75%UTS were analyzed Under quasi-static conditions, the segmented results for different classes were overlaid, and the model accurately identified damage initiation near the stitch sites, attributed to high stress concentrations (Fig. 4-52a). These findings were consistent with the observations in Section 4.3 for the same material system and Suratkar [73] for UD-NCF carbon fiber/epoxy composites. Furthermore, the evolution of 90° tow cracks was effectively tracked and correlated with applied stress levels, ranging from 61MPa to 104 MPa, and eventually to 154Mpa (Fig. 4-52a). The 90° tow cracks spanned the entire width of the specimen and were evenly distributed along the specimen length and loading direction (Fig. 4-52b). Microscopic observations at the edge of the specimen further validated the capability of the model to accurately characterize damage (Fig. 4-52c). Under tension-tension fatigue loading at 75% UTS, 90º fiber tow cracks were observed during the first loading cycle (Fig. 4-37). A representative specimen surface image was compared with segmentations generated by the optimized deep learning model and those detected using a conventional automated crack counting algorithm (Fig. 4-53a-c). A strong correlation was observed, however, the deep learning

model demonstrated enhanced capability in preserving the architecture of the cracks, thereby enabling tracking crack interactions. The segmented 90° tow cracks were further validated by microscopic observations at the edge of the specimen at the indicated location (Fig. 4-53d).

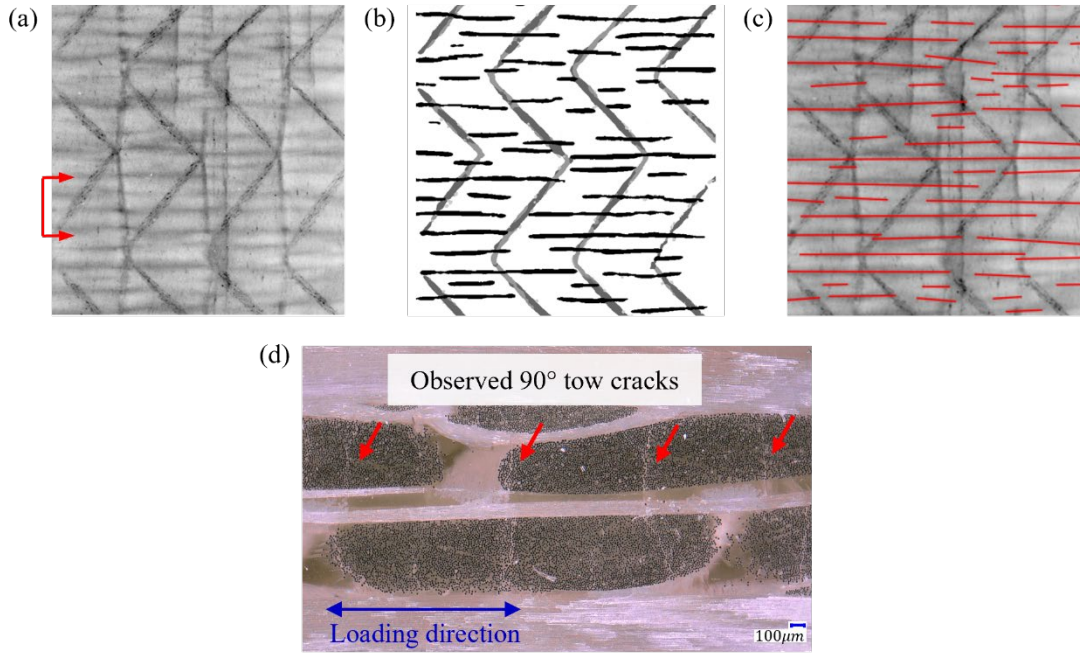


Fig. 4-53. Comparison and validation of segmented and actual 90° tow crack (Class 1) under tension-tension cyclic loading at 75% UTS: (a) example of specimen surface image captured during cyclic loading; (b) segmented 90° tow cracks using the optimized deep learning model; (c) detected 90° tow cracks using conventional automated crack counting algorithms; and (d) microscope observation at the indicated location for validation.

Crack density was calculated based on the segmented 90° tow cracks and compared with experimental data reported in Sections 4.3 and 4.4. for the same material system under quasi-static tensile and tension-tension cyclic loading, respectively (Fig. 4-54). Under quasi-static loading, a good agreement was observed across the entire stress range. The 90° tow cracks initiated at ~85MPa, followed by a pronounced linear increase in crack density due to the progressive evolution of 90° tow cracks. The crack density rate (CDR), defined as the slope of the crack density-stress curve, exhibited close consistency between experimental detection (~0.0116 mm^{-1}/MPa) and model segmentations (~0.0120 mm^{-1}/MPa). Crack density reached a plateau at ~235MPa in the model segmentations, correlating well with the reported value of ~230MPa. Under cyclic loading, a similar trend was

observed throughout fatigue life. As the number of cycles increased, 90º tow cracks rapidly accumulated and saturated less than 10% of the total fatigue life, with crack density reaching a plateau at ~250 cycles, aligning well with the results in Fig. 4-39. Overall, the model demonstrated a robust capability to segmented 90° tow crack evolution with high accuracy, aligning closely with experimental observations. The strong correlation between segmented and experimental crack density, as well as the consistent agreement in crack density rate and plateau values, highlights the reliability and generalization capability of the model.

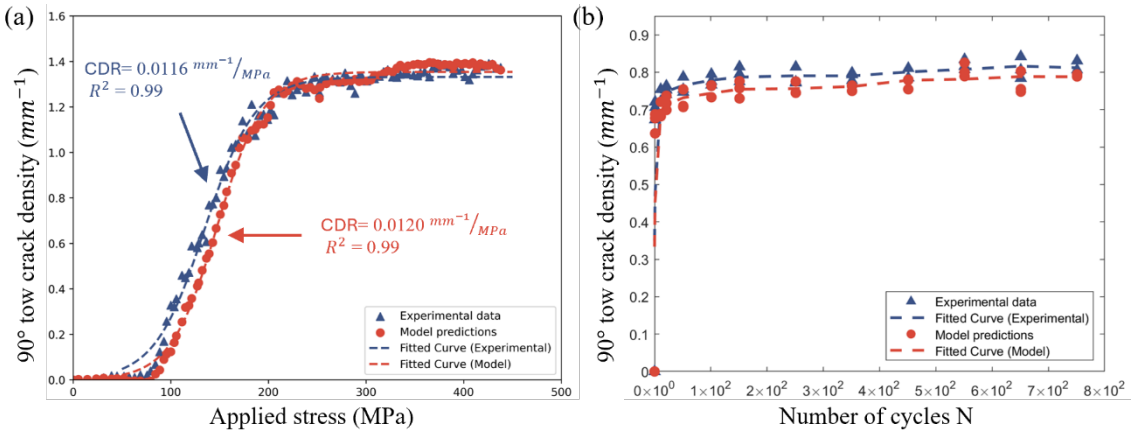


Fig. 4-54. Comparison and validation of segmented and experimental results for 90° tow crack density evolution under quasi-static loading.

Chapter 5
Conclusions and Recommendations

5.1 Conclusions

The primary objective of this research was to develop a deep learning-assisted digital imaging technique to enable the comprehensive characterization of damage progression in unidirectional non-crimp fabric (UD-NCF) glass fiber-reinforced reactive thermoplastic composites under various temperature and loading conditions. The main outcome of this research endeavor was to address key gaps identified in the literature, including to develop an automated in-situ digital imaging technique capable of detecting and characterizing damage in real time and advance the understanding of mechanical behavior and damage mechanisms in the studied material system. To achieve this, the research comprised four main tasks. The first task involved analyzing the deformation response and failure behavior of the material at room and low ambient temperatures. The second task focused on developing and validating an in-situ non-destructive digital imaging technique for monitoring damage evolution during quasi-static tensile loading. The third task aimed to investigate damage progression and stiffness degradation under tension-tension cyclic loading. The last task comprised developing a deep learning-based convolutional neural network (CNN) model for the qualitative and quantitative characterization of damage.

In task 1, the longitudinal tensile, transverse tensile, and in-plane shear response and associated failure behaviour of infusible UD-NCF glass fiber-reinforced reactive Elium® (NCF GF/acrylic) and UD-NCF glass fiber-reinforced epoxy (NCF GF/epoxy) composite materials at room temperature (RT, 22°C) and low temperature (-50°C) were characterized. Digital image correlation (DIC) and post-test optical microscopy were employed to evaluate the effect of temperature on damage evolution and failure mechanisms in the studied material systems. The main results are summarized as follows:

- For the longitudinal tensile mode, both materials exhibited nearly linear elastic stress-strain responses up to failure at both temperatures. The tensile strength increased slightly at -50°C, respectively by 8.12% and 8.95% for the NCF GF/acrylic and NCF GF/epoxy materials. The compressive residual stresses that developed during the temperature cooldown increased the strength of the fiber-matrix interface, which contributed to the increase in tensile strength at low temperature. However, the temperature had a minimal influence on the modulus and strains at failure for both materials. The mechanical properties were comparable for both material systems for each ambient temperature considered owing to the fiber-dominant behaviour. Furthermore, the failure characteristics were dependent on temperature for both material

systems with specimens tested at low temperature exhibiting notably more splitting cracks within the tows.

- For the transverse tensile mode, both materials exhibited a similar nonlinear stress-strain response at RT owing to the accumulation of transverse cracks within the tows. Although, greater strain at failure was observed for the NCF GF/acrylic at RT due to local matrix plastic deformation, which resulted in fiber bridging. At low temperature, both materials exhibited a distinct bilinear stress-strain response with earlier onset of damage and greater density of transverse cracks compared to RT. A significant increase in tensile strength (23.21% for NCF GF/acrylic and 25.01% for NCF GF/epoxy) and elastic modulus (35.26% for NCF GF/acrylic and 29.00% for NCF GF/epoxy) was observed at low temperature. The strain at failure also increased at low temperature by 48% for NCF GF/acrylic and 53% for NCF GF/epoxy. The NCF GF/acrylic material transitioned from ductile to brittle failure at -50°C, which was characterized in part by pullout and breakage of supporting fibers. The NCF GF/epoxy material exhibited similar failure characteristics at both ambient temperatures, with more notable damage at -50°C, which further highlighted the important role of supporting fibers in the failure process during transverse tensile loading. The increased brittle fracture of the materials at low temperature were offset by increased damage tolerance, which ultimately led to the increase in the mechanical properties reported. The mechanical properties were also comparable for both material systems for each ambient temperature considered.
- For the in-plane shear mode, both materials exhibited a notable nonlinear stress-strain response with a pronounced plateau at RT. The degree of nonlinearity was more notable for the NCF GF/acrylic material owing to the ductility of the resin and local fiber reorientation, which led to a higher strain at failure. However, at low temperature the increased stiffness and brittleness of the resin resulted in a markedly less nonlinear response for both materials, leading to a significant reduction in the strain at failure. This behaviour is distinct than that observed for longitudinal and transverse tension were the strain at failure increased at low ambient temperature. The NCF GF/acrylic material transitioned from ductile to brittle failure at low temperature, which was characterized by a smooth fracture surface and splitting of the supporting fiber yarns. The NCF GF/epoxy material exhibited brittle behaviour at both temperatures, with the supporting fiber yarns also influencing the material behaviour. The shear strength and modulus increased by 23.74% and 50.74% for the NCF GF/acrylic and 44.84%

and 34.86% for the NCF GF/epoxy, respectively, and is attributed to the improved matrix and fiber-matrix interface properties at lower temperatures. Also, the shear strength of the NCF GF/epoxy material was greater than that of the NCF GF/acrylic material at low temperature.

In task 2, an automated in-situ digital imaging technique was developed to characterize damage in infused unidirectional non-crimp fabric (UD-NCF) glass fiber/reactive thermoplastic cross-ply laminates at room temperature (RT, 22°C) and low temperature (LT, -50°C). Post test optical microscopy and SEM were employed to validate the observed damage modes and identified failure mechanisms for both ambient temperatures. The influence of low ambient temperature on damage evolution of the tested cross-ply specimens was assessed using quantitative damage metrics, including crack density, crack density rate, and crack length increasement. The main results are summarized as follows:

- The developed digital imaging technique was effective in capturing intra-laminar damage mechanisms through the thickness of the translucent cross-ply specimens at low temperatures, including cracks within the 90° tows, splitting cracks within the 0° tows, and localized inter-tow matrix cracks. The automated technique enabled detailed assessment of the initiation and progression of damage, as well as the interaction of the developed damage modes.
- The characteristic tensile stress-strain response of the cross-ply laminate comprised a linear elastic stage followed by slight nonlinearity prior to failure. For the LT specimens, the transition, which aligned with the onset of stiffness degradation, was abrupt and occurred at a lower magnitude of strain when compared to the RT specimens, demonstrating the temperature-dependency of damage onset.
- At both ambient temperatures, local damage initiated at the stitching locations and developed into 90° tow cracks. These cracks continued to grow and multiply at a constant rate with increasing applied load up to saturation where a reduction in the rate of stiffness degradation was observed. At low ambient temperatures, 90° tow cracks initiated sooner and developed at a rate that was twice as high as that observed for the RT specimens, where damage was more severe at saturation with a crack density 60% greater.
- Final failure was preceded by the development of splitting cracks in the 0° tows and tow interfacial cracks, as well as delamination cracks. The fracture surfaces were brittle in nature

and characterized by an even fracture line along the internal 90° fiber layers as well as fiber bundle pull-out from the 0° tows. At low temperature a greater amount of resin was observed on the surface of the pulled-out fibers, in lieu of predominantly bare fibers at room temperature, which reveals enhanced fiber-matrix interfacial properties and brittle fracture of the resin in the vicinity of the fibers (i.e., a distinct local brittle damage mode). The density of 0° tow cracks observed prior to failure at low temperature was greater when compared to room temperature, providing evidence of strengthening of the laminate, which may be in part due to the mismatch in the coefficient of thermal expansion of the 0° and 90° plies.

- Despite exhibiting an onset of damage at a lower magnitude of strain, an increased CDR, and more severe stiffness degradation owing to increased crack density, the UD-NCF glass fiber/reactive thermoplastic material exhibited higher damage tolerance and a comparable strain at failure at LT.

In task 3, a novel in-situ integrated digital imaging technique was developed to simultaneously characterize damage and monitor stiffness degradation in unidirectional non-crimp fabric (UD-NCF) glass fiber/acrylic cross-ply laminates subjected to tension-tension cyclic loading. Two peak stress magnitudes were chosen to assess the damage evolution process and corresponding stiffness degradation. Crack density, crack density rate during propagation, and crack length increasement were chosen as damage metrics. Optical microscopy was employed to capture damage on the edge of the tested specimens, providing a one-to-one comparison of the damage mechanisms detected using the developed digital imaging technique. The main results are summarized as follows:

- The developed digital imaging technique allowed for effective in-situ damage characterization and strain measurement, which enabled the automated identification of different damage mechanisms, observation of the locations of damage initiation, quantification of damage propagation (i.e., crack length increasement), and direct correlation of damage states with stiffness degradation for a single test specimen.

- For a peak cyclic stress of 50%UTS, which was slightly higher than the fatigue threshold determined using a rapid thermographic technique, the dominant damage mechanisms during the early stages of loading were cracks in the 90º fiber tows which directly correlated to a drop in the laminate stiffness. These 90° fiber tow cracks were observed to initiate at the location of the stitching sites near the transversely oriented supporting glass fiber yarns during the first

loading cycle. With further increase in the number of loading cycles, additional 90º tow cracks initiated along the specimen length which tended to propagate along the fiber tows at consistent rate, causing a more gradual degradation of the laminate stiffness. After the saturation of 90º tow cracks, localized delamination cracks developed, in which the stiffness degradation was minor. As delamination cracks continued to propagate at the 0º and 90º fiber tow interface along the loading direction, 0º fiber tow pull-out and breakage were observed to precede failure of the specimen.

- In contrast, at peak stress of 75%UTS (i.e., low cycle fatigue regime), both 0º and 90º fiber tow cracks were observed to initiate during the first loading cycle, leading to a greater stiffness drop when compared to the specimens tested under a peak cyclic stress of 50%UTS. The high stress magnitude led to a more rapid damage growth rate and lower saturated 90º tow crack density. This phenomenon was also revealed by the significant interactions between the developed damage modes, contributing to failure of the specimen after fewer number of loading cycles.

In task 4, a deep learning-based convolutional neural network (CNN) model with automated crack counting algorithms was developed to characterize damage in unidirectional non-crimp fabric (UD-NCF) cross-ply laminates subjected to both quasi-static tensile and tension-tension cyclic loading. Digital images from Section 4.3 were preprocessed and annotated. Six classes were defined based on experimental observations (Section 4.3.3) and the annotated images were divided into training and testing sets. The U-Net architecture, incorporating skip connection, dropout, and weighted Dice loss were selected to train and evaluate the model under various hyperparameters, including batch size, class weights, and the number of epochs. The optimal model with pertained weights and tuned hypermeters were then applied to detect damage across the entire dataset. Both qualitative and quantitative validations were performed to assess the model's performance. The main results are summarized as follows:

- Batch size impact: Smaller batch sizes (BS-1 and BS-3) consistently outperformed larger batch sizes (BS-5 and BS-7) in terms of convergence speed and higher accuracy. BS-1 achieved the lowest weighted Dice loss (~0.89), approximately 0.45% lower than BS-5 and BS-7. Furthermore, it attained the highest mean and Class 1 Dice coefficient (~0.74), highlighting its clear superiority over larger batch sizes.

- Class weights impact: High bias class weight configurations ([801111] and [601111]) resulted in the lowest weighted Dice loss (~0.87). Assigning higher weights to Class 1 significantly improved Class 1 Dice coefficient, from ~0.736 for balanced class weights ([111111]) to ~0.840, although a slight decrease in mean Dice coefficients was observed. These findings suggest that assigning lower weights to less critical classes can enhance the model's performance on more important classes, particularly in imbalanced datasets.
- Epoch impact: The testing weighted Dice loss and Class 1 Dice coefficients stabilized at approximately 150 epochs with minimum difference observed between the training and testing metrics (~0.016% for weighted Dice loss and ~0.52% Class 1 Dice coefficients). After 156 epochs, fluctuations in testing performance and an increasing discrepancy between training and testing metrics indicated signs of overfitting. These findings suggest that early stopping at 156 epochs optimizes segmentation accuracy while mitigating overfitting, particularly for critical classes such as Class 1.
- Damage segmentation capabilities: The pretrained deep learning model was effective in identifying the location and type of damage, including damage initiation, progression and interaction, enabling a detailed assessment of damage mechanisms. Additionally, the model could be seamlessly integrated with crack counting algorithms to quantitatively assess crack density evolution. It should be noted that the model was specifically trained on the studied NCF material and may not be directly applicable to other fabric types with different surface architectures. Refer to Section 4.5.1 for a detailed guidance on adapting the model for other composite types.

5.2 Contributions

The first task improved the understanding of the low-temperature deformation response and damage and failure characteristics of thermoplastic-based composites and filled a critical gap in literature. This understanding is essential for future studies focused on characterizing the performance and damage behaviour of these materials under cyclic or impact loading and for developing damage-based constitutive models. The comparative assessment with an equivalent glass fiber/epoxy composite provides an important benchmark to enhance the performance of this class of fiber-reinforced composite material under low temperatures and enable replacement in future wind turbine blade structures.

The second task provided deeper insights into the low-temperature deformation response, damage characteristics, and damage tolerance of glass fiber/thermoplastic cross-ply laminates subjected to quasi-static tensile loading. It also demonstrated the effectiveness of the digital imaging technique in capturing intra-lamina damage mechanisms at low temperatures. Furthermore, the developed digital imaging technique can be seamlessly integrated with an automated crack counting algorithm to quantify damage metrics. This study fills a critical gap in the literature for non-crimp fabric composites and the results will be an important database for temperature-dependent damage mechanics modeling in future work.

The third task demonstrated the effectiveness of the integrated digital imaging technique in direct correlating damage events with stiffness degradation during cyclic loading, leading to a more comprehensive understanding of the fatigue damage behavior of glass fiber/thermoplastic composites. The observed trends in damage progression and stiffness degradation offer valuable data for developing predictive models that assess the long-term structural integrity of composite components. Specifically, the number of cycles required to initiate tow cracks and the evolution of tow crack density and length increasement can be used to calibrate progressive damage-based fatigue prediction models for UD-NCF composites.

The final task demonstrated the strong potential of deep learning-based approaches to efficiently and accurately identify damage initiation, progression, and interaction in glass fiber/thermoplastic composites. Furthermore, the model can be seamlessly integrated with automated crack counting algorithms for quantitative damage assessment, enabling a detailed assessment of damage mechanisms The annotated dataset generated provides a solid foundation for future research in advanced deep learning approaches for damage characterization in NCF composites.

5.3 Recommendations for Future Work

5.3.1 Material characterization

Future studies should focus on exploring the influence of prolonged low temperature exposure on the performance and failure characteristics of the material under a range of exposure times, as this would further enhance the understanding of their behavior and durability. Research should also assess damage mechanisms associated with thermal cycling to low temperatures, as this would be representative of in-service conditions. Additionally, evaluating the material's performance under low

temperature impact, compression, and flexure loading as well as determining its fracture toughness would complement the current results and help establish comprehensive material design guidelines for cold-region applications.

5.3.2 Integrated digital imaging technique

Further investigation is needed to fully validate and expand the developed technique. First, multidirectional laminates with off-axis plies should be considered to enable detection of tow cracks across various ply orientations. Testing multidirectional laminates will also provide further opportunity to assess the capability of the technique to detect delamination crack. Second, additional loading conditions, such as compression and impact, should be explored to further evaluate the robustness of the method. Moreover, future studies should include fatigue testing under varying maximum applied stress levels, more complex cyclic loading scenarios (e.g., tension–compression and compression–compression), and an expanded range of temperature conditions to improve the model's generalizability and application to real-world service environments.

5.3.3 Deep learning-assisted damage characterization model

Future work should explore more sophisticated or hybrid models to further improve the segmentation accuracy. For instance, incorporating domain knowledge into network architecture (e.g., physics-informed neural networks) or fusing data from multiple sources (e.g., combining visual imaging with thermal imaging, acoustic emission, or strain sensors) could significantly improve detection accuracy and robustness. It is also important to integrate predictive models capable of assessing the current damage state of the material, thereby supporting decisions related to repair and maintenance planning. Furthermore, these AI-driven approaches should be validated in real-time damage monitoring scenarios, such as detecting damage in wind turbine blades during operation and benchmark their performance against conventional non-destructive evaluation techniques to ensure practical applicability. Additionally, future work could involve training models with different class weight configurations to better distinguish between various damage modes, thereby potentially improving segmentation performance in complex multi-class scenarios.

Letter of Copyrights Permission

In accordance with the author rights policy of Government of Canada, Elsevier, Sage, Springer, CSIR, and Cambridge University Press, individuals retain the right to include their article in a thesis/dissertation without the need for prior formal request. In the preparation of Chapter 3 and 4, the following journals have been referred to as the original source, either in their entirety or in parts.

E. Shi and J. Montesano, "Effect of low temperature on the mechanical properties and failure characteristics of an infused non-crimp fabric glass fiber-reinforced reactive thermoplastic," (Submitted to Composites Science and Technology_ Under Review)

E. Shi and J. Montesano, "Characterization of damage in non-crimp fabric glass fiber-reinforced reactive thermoplastic composites at low temperature using an in-situ digital imaging technique," Composites Part A: Applied Science and Manufacturing, vol. 190, p. 108674, Mar. 2025, doi: 10.1016/j.compositesa.2024.108674.

E. Shi and J. Montesano, "Integrated digital imaging technique for correlation of damage evolution and stiffness degradation in non-crimp fabric composite materials under cyclic loading," Composite Structures, vol. 371, p. 119513, Nov. 2025, doi: 10.1016/j.compstruct.2025.119513.

E. Shi, J. Montesano, Y. Zeng, and K. Rouf, "Deep Learning-Assisted Damage Characterization in Non-crimp Fabric Composites," (Submitted to Composites Science and Technology - Under Review)

Copyright permission has been duly granted for the following materials along with their respective right holders. The agreements have been established between the University of Waterloo (represented by Erli Shi) and the respective right holders, each assigned with unique license numbers or by written approvals:

Figure	Right Holder	Reference	License Number
1-2a	Government of Canada	"Clean Energy for Rural and Remote Communities Program." [Online]. Available: https://natural-resources.canada.ca/reducingdiesel. [Accessed: 16-Apr-2025].	Not needed
1-2b	Government of Canada	"Overview of the Numerical Simulations on Canadian Territory." [Online]. Available: http://www.windatlas.ca/maps-en.php?field=EU&height=30&season=ANU. [Accessed: 16-Apr-2025].	Not needed
1-3a	Elsevier	H. Pakdel and B. Mohammadi, "Stiffness degradation of composite laminates due to matrix cracking and induced delamination during tension-tension fatigue," Engineering Fracture Mechanics, vol. 216, p. 106489, Jul. 2019, doi: 10.1016/j.engfracmech.2019.106489.	6063200216214
1-3b	Elsevier	E. K. Gamstedt and B. A. Sjögren, "Micromechanisms in tension-compression fatigue of composite laminates containing transverse plies," Composites Science and Technology, vol. 59, no. 2, pp. 167–178, Feb. 1999, doi: 10.1016/S0266-3538(98)00061-X.	6063210879254
1-3c	Elsevier	R. Gutkin, S. T. Pinho, P. Robinson, and P. T. Curtis, "On the transition from shear-driven fibre compressive failure to fibre kinking in notched CFRP laminates under longitudinal compression," Composites Science and Technology, vol. 70, no. 8, pp. 1223–1231, Aug. 2010, doi: 10.1016/j.compscitech.2010.03.010.	6063200395758
1-3d	Elsevier	D. T. G. Katerelos, J. Varna, and C. Galiotis, "Energy criterion for modelling damage evolution in cross-ply composite laminates," Composites Science and	6063211060790

		Technology, vol. 68, no. 12, pp. 2318–2324, Sep. 2008, doi: 10.1016/j.compscitech.2007.09.014.	
1-3e	Cambridge University Press	R. Olsson, “Modelling of impact damage zones in composite laminates for strength after impact,” The Aeronautical Journal, vol. 116, no. 1186, pp. 1349–1365, Dec. 2012, doi: 10.1017/S0001924000007673.	Not needed for use of content in a Master's Thesis and/or Doctoral Dissertation
2-2	Elsevier	S. V. Lomov, Ed., Non-Crimp Fabric Composites: Manufacturing, Properties and Applications. Woodhead Publishing Limited, 2011.	6063211493975
2-3	Elsevier	W. Obande, C. M. Ó Brádaigh, and D. Ray, “Continuous fibre-reinforced thermoplastic acrylic-matrix composites prepared by liquid resin infusion – A review,” Composites Part B: Engineering, vol. 215, p. 108771, Jun. 2021, doi: 10.1016/j.compositesb.2021.108771.	6063200573063
2-4	CSIR	M. A. Torabizadeh, “Tensile, compressive and shear properties of unidirectional glass/epoxy composites subjected to mechanical loading and low temperature services,” Indian Journal of Engineering and Materials Sciences, vol. 20, pp. 299–309, Aug. 2013.	By e-mail
2-5	Elsevier	W. Obande, D. Mamalis, D. Ray, L. Yang, and C. M. Ó Brádaigh, “Mechanical and thermomechanical characterisation of vacuum-infused thermoplastic- and thermoset-based composites,” Materials & Design, vol. 175, p. 107828, Aug. 2019, doi: 10.1016/j.matdes.2019.107828.	Not needed, under Creative Commons Attribution-NonCommercial-No Derivatives License (CC BY NC ND)
2-6	Elsevier	Z. Arwood, D. S. Cousins, S. Young, A. P. Stebner, and D. Penumadu, “Infusible thermoplastic composites for wind turbine blade manufacturing: Static characterization of thermoplastic laminates under ambient conditions,”	Not needed, under Creative Commons Attribution-NonCommercial-No Derivatives

		Composites Part C: Open Access, vol. 11, p. 100365, Jul. 2023, doi: 10.1016/j.jcomc.2023.100365.	License (CC BY NC ND)
2-7	John Montesano	John Montesano. Fatigue damage characterization of braided and woven fiber reinforced polymer matrix composites at room and elevated temperatures [Doctoral Thesis]. Ryerson University; 2012.	By e-mail
2-8	Elsevier	M. Drvoderic, M. Gfrerrer, J. Wiener, G. Pinter, M. Pletz, and C. Schuecker, "Comparing crack density and dissipated energy as measures for off-axis damage in composite laminates," International Journal of Fatigue, vol. 169, p. 107486, Apr. 2023, doi: 10.1016/j.ijfatigue.2022.107486.	Not needed, under Creative Commons CC-BY license
2-9	Sage	J. Zangenberg, P. Brøndsted, and J. W. Gillespie, "Fatigue damage propagation in unidirectional glass fibre reinforced composites made of a non-crimp fabric," Journal of Composite Materials, vol. 48, no. 22, pp. 2711–2727, Sep. 2014, doi: 10.1177/0021998313502062.	6063201076884
2-10	Elsevier	M. Drvoderic, M. Rettl, M. Pletz, and C. Schuecker, "CrackDect: Detecting crack densities in images of fiber-reinforced polymers," SoftwareX, vol. 16, p. 100832, Dec. 2021, doi: 10.1016/j.softx.2021.100832.	Not needed, under Creative Commons CC-BY license
2-11b	Springer	O. Ronneberger, P. Fischer, and T. Brox, "U-Net: Convolutional Networks for Biomedical Image Segmentation," in Medical Image Computing and Computer-Assisted Intervention – MICCAI 2015, N. Navab, J. Hornegger, W. M. Wells, and A. F. Frangi, Eds., Cham: Springer International Publishing, 2015, pp. 234–241. doi: 10.1007/978-3-319-24574-4_28.	6063201416675

References

[1] A. Dinita et al., “Advancements in Fiber-Reinforced Polymer Composites: A Comprehensive Analysis,” Polymers, vol. 16, no. 1, Art. no. 1, Jan. 2024, doi: 10.3390/polym16010002.

[2] G. Marsh, “Airbus takes on Boeing with reinforced plastic A350 XWB,” Reinforced Plastics, vol. 51, no. 11, pp. 26–29, Dec. 2007, doi: 10.1016/S0034-3617(07)70383-1.

[3] H. Teng, S. Li, Z. Cao, S. Li, C. Li, and T. J. Ko, “Carbon Fiber Composites for Large-Scale Wind Turbine Blades: Applicability Study and Comprehensive Evaluation in China,” Journal of Marine Science and Engineering, vol. 11, no. 3, Art. no. 3, Mar. 2023, doi: 10.3390/jmse11030624.

[4] “Canada’s 2030 Emissions Reduction Plan - Chapter 2” [Online]. Available: https://www.canada.ca/en/services/environment/weather/climatechange/climate-plan/climate-plan-overview/emissions-reduction-2030/plan/chapter-2.html. [Accessed: 16-Apr-2025].

[5] “Clean Energy for Rural and Remote Communities Program.” [Online]. Available: https://natural-resources.canada.ca/reducingdiesel. [Accessed: 16-Apr-2025].

[6] “Overview of the Numerical Simulations on Canadian Territory.” [Online]. Available: http://www.windatlas.ca/maps-en.php?field=EU&height=30&season=ANU. [Accessed: 16-Apr-2025].

[7] P. A. Carraro and M. Quaresimin, “Fatigue damage and stiffness evolution in composite laminates: a damage-based framework,” Procedia Engineering, vol. 213, pp. 17–24, Jan. 2018, doi: 10.1016/j.proeng.2018.02.003.

[8] H. Pakdel and B. Mohammadi, “Stiffness degradation of composite laminates due to matrix cracking and induced delamination during tension-tension fatigue,” Engineering Fracture Mechanics, vol. 216, p. 106489, Jul. 2019, doi: 10.1016/j.engfracmech.2019.106489.

[9] R. Talreja and C. V. Singh, Damage and failure of composite materials. Cambridge ; New York: Cambridge University Press, 2012.

[10] E. K. Gamstedt and B. A. Sjögren, “Micromechanisms in tension-compression fatigue of composite laminates containing transverse plies,” Composites Science and Technology, vol. 59, no. 2, pp. 167–178, Feb. 1999, doi: 10.1016/S0266-3538(98)00061-X.

[11] R. Gutkin, S. T. Pinho, P. Robinson, and P. T. Curtis, “On the transition from shear-driven fibre compressive failure to fibre kinking in notched CFRP laminates under longitudinal compression,” *Composites Science and Technology*, vol. 70, no. 8, pp. 1223–1231, Aug. 2010, doi: 10.1016/j.compscitech.2010.03.010.

[12] D. T. G. Katerelos, J. Varna, and C. Galiotis, “Energy criterion for modelling damage evolution in cross-ply composite laminates,” Composites Science and Technology, vol. 68, no. 12, pp. 2318–2324, Sep. 2008, doi: 10.1016/j.compscitech.2007.09.014.

[13] R. Olsson, “Modelling of impact damage zones in composite laminates for strength after impact,” *The Aeronautical Journal*, vol. 116, no. 1186, pp. 1349–1365, Dec. 2012, doi: 10.1017/S0001924000007673.

[14] L. Mishnaevsky, K. Branner, H. N. Petersen, J. Beauson, M. McGugan, and B. F. Sørensen, “Materials for Wind Turbine Blades: An Overview,” Materials, vol. 10, no. 11, Art. no. 11, Nov. 2017, doi: 10.3390/ma10111285.

[15] P. S. Veers et al., “Trends in the Design, Manufacture and Evaluation of Wind Turbine Blades,” Wind Energy, vol. 6, no. 3, pp. 245–259, 2003, doi: 10.1002/we.90.

[16] Z. Sápi and R. Butler, “Properties of cryogenic and low temperature composite materials – A review,” Cryogenics, vol. 111, p. 103190, Oct. 2020, doi: 10.1016/j.cryogenics.2020.103190.

[17] J. LeBlanc et al., “Low temperature effects on the mechanical, fracture, and dynamic behavior of carbon and E-glass epoxy laminates,” International Journal of Lightweight Materials and Manufacture, vol. 3, no. 4, pp. 344–356, Dec. 2020, doi: 10.1016/j.ijlmm.2020.05.002.

[18] U. K. Vaidya and K. K. Chawla, “Processing of fibre reinforced thermoplastic composites,” *International Materials Reviews*, vol. 53, no. 4, pp. 185–218, Jul. 2008, doi: 10.1179/174328008X325223.

[19] M. Biron, “Thermoplastics and Thermoplastic Composites”, 2nd ed. Oxford, United Kingdom: William Andrew, 2012.

[20] D. S. Cousins et al., “Infusible Thermoplastic Composites for Wind Turbine Blade Manufacturing: Fatigue Life of Thermoplastic Laminates under Ambient and Low-Temperature Conditions,” Advanced Engineering Materials, vol. 25, no. 11, p. 2201941, 2023, doi: 10.1002/adem.202201941.

[21] O. Ahmed, X. Wang, M.-V. Tran, and M.-Z. Ismadi, “Advancements in fiber-reinforced polymer composite materials damage detection methods: Towards achieving energy-efficient

SHM systems," Composites Part B: Engineering, vol. 223, p. 109136, Oct. 2021, doi: 10.1016/j.compositesb.2021.109136.

[22] P. Duchene, S. Chaki, A. Ayadi, and P. Krawczak, "A review of non-destructive techniques used for mechanical damage assessment in polymer composites," J Mater Sci, vol. 53, no. 11, pp. 7915–7938, Jun. 2018, doi: 10.1007/s10853-018-2045-6.

[23] P. A. Carraro, L. Maragoni, and M. Quaresimin, "Characterisation and analysis of transverse crack-induced delamination in cross-ply composite laminates under fatigue loadings," International Journal of Fatigue, vol. 129, p. 105217, Dec. 2019, doi: 10.1016/j.ijfatigue.2019.105217.

[24] L. Maragoni, P. A. Carraro, M. Peron, and M. Quaresimin, "Fatigue behaviour of glass/epoxy laminates in the presence of voids," International Journal of Fatigue, vol. 95, pp. 18–28, Feb. 2017, doi: 10.1016/j.ijfatigue.2016.10.004.

[25] J. A. Glud, J. M. Dulieu-Barton, O. T. Thomsen, and L. C. T. Overgaard, "Automated counting of off-axis tunnelling cracks using digital image processing," Composites Science and Technology, vol. 125, pp. 80–89, Mar. 2016, doi: 10.1016/j.compscitech.2016.01.019.

[26] M. Drvoderic, M. Rettl, M. Pletz, and C. Schuecker, "CrackDect: Detecting crack densities in images of fiber-reinforced polymers," SoftwareX, vol. 16, p. 100832, Dec. 2021, doi: 10.1016/j.softx.2021.100832.

[27] J. Reiner, R. Vaziri, and N. Zobeiry, "Machine learning assisted characterisation and simulation of compressive damage in composite laminates," Composite Structures, vol. 273, p. 114290, Oct. 2021, doi: 10.1016/j.compstruct.2021.114290.

[28] R. F. Ribeiro Junior and G. F. Gomes, "On the Use of Machine Learning for Damage Assessment in Composite Structures: A Review," Appl Compos Mater, vol. 31, no. 1, pp. 1–37, Feb. 2024, doi: 10.1007/s10443-023-10161-5.

[29] M. Amini and A. Rahmani, "Machine Learning Process Evaluating Damage Classification of Composites," Jan. 01, 2023, Social Science Research Network, Rochester, NY: 4331923. Accessed: Jun. 30, 2025. [Online]. Available: https://papers.ssrn.com/abstract=4331923.

[30] T. W. Clyne and D. Hull, An Introduction to Composite Materials. Higher Education from Cambridge University Press, 2019.

[31] K. van Rijswijk and H. E. N. Bersee, “Reactive processing of textile fiber-reinforced thermoplastic composites – An overview,” Composites Part A: Applied Science and Manufacturing, vol. 38, no. 3, pp. 666–681, Mar. 2007, doi: 10.1016/j.compositesa.2006.05.007.

[32] R. T. Durai Prabhakaran, “Are Reactive Thermoplastic Polymers Suitable for Future Wind Turbine Composite Materials Blades?,” Mechanics of Advanced Materials and Structures, vol. 21, no. 3, pp. 213–221, Mar. 2014, doi: 10.1080/15376494.2013.834090.

[33] R. E. Murray, D. Swan, D. Snowberg, D. Berry, R. Beach, and S. Rooney, “Manufacturing a 9-Meter Thermoplastic Composite Wind Turbine Blade,” Proceedings of the American Society for Composites â€” Thirty-second Technical Conference, vol. 0, no. 0, 2017, doi: 10.12783/asc2017/15166.

[34] D. Snowberg, D. Berry, D. Swan, M. Zhang, S. Nolet, D. Adams, J. Goodsell, D. Penumadu, and A. Stebner, “IACMI Project 4.2: Thermoplastic Composite Development for Wind Turbine Blades,” United States: N. p., 2021. Web. doi:10.2172/1834393.

[35] R. E. Murray et al., “Structural validation of a thermoplastic composite wind turbine blade with comparison to a thermoset composite blade,” Renewable Energy, vol. 164, pp. 1100–1107, Feb. 2021, doi: 10.1016/j.renene.2020.10.040.

[36] D. S. Cousins, Y. Suzuki, R. E. Murray, J. R. Samaniuk, and A. P. Stebner, “Recycling glass fiber thermoplastic composites from wind turbine blades,” Journal of Cleaner Production, vol. 209, pp. 1252–1263, Feb. 2019, doi: 10.1016/j.jclepro.2018.10.286.

[37] S. P. Subadra and P. Griskevicius, “Sustainability of polymer composites and its critical role in revolutionising wind power for green future,” Sustainable technologies for green economy, vol. 1, no. 1, pp. 1–7, 2021, doi: 10.21595/stge.2021.21974.

[38] L. Mishnaevsky, “Sustainable End-of-Life Management of Wind Turbine Blades: Overview of Current and Coming Solutions,” Materials, vol. 14, no. 5, Art. no. 5, Jan. 2021, doi: 10.3390/ma14051124.

[39] S. V. Lomov, Ed., Non-Crimp Fabric Composites: Manufacturing, Properties and Applications. Woodhead Publishing Limited, 2011.

[40] G. Zhou et al., “Experimental investigation on the effects of fabric architectures on mechanical and damage behaviors of carbon/epoxy woven composites,” Composite Structures, vol. 257, p. 113366, Feb. 2021, doi: 10.1016/j.compstruct.2020.113366.

[41] V. Carvelli and S. V. Lomov, Eds., Fatigue of Textile Composites. Woodhead Publishing Limited, 2015.

[42] K. Vallons, G. Adolphs, P. Lucas, S. V. Lomov, and I. Verpoest, “The influence of the stitching pattern on the internal geometry, quasi-static and fatigue mechanical properties of glass fibre non-crimp fabric composites,” Composites Part A: Applied Science and Manufacturing, vol. 56, pp. 272–279, Jan. 2014, doi: 10.1016/j.compositesa.2013.10.015.

[43] H. Krieger, T. Gries, and S. E. Stapleton, “Design of Tailored Non-Crimp Fabrics Based on Stitching Geometry,” Appl Compos Mater, vol. 25, no. 1, pp. 113–127, Feb. 2018, doi: 10.1007/s10443-017-9603-y.

[44] L. Asp, F. Edgren, and A. Sjögren, “Effects of stitch pattern on the mechanical properties of non-crimp fabric composites,” presented at the European Conference on Composite Materials : 31/05/2004 - 03/06/2004, European Society for Composite Materials, 2004. Accessed: Jul. 17, 2023. [Online]. Available: https://urn.kb.se/resolve?urn=urn:nbn:se:ltu:diva-38720.

[45] M. Wouters, Effects of fibre bundle size and stitch pattern on the static properties of unidirectional carbon-fibre non-crimp fabric composites. 2002. Accessed: Jul. 17, 2023. [Online]. Available: https://urn.kb.se/resolve?urn=urn:nbn:se:ltu:diva-43566.

[46] T. C. Truong, M. Vettori, S. Lomov, and I. Verpoest, “Carbon composites based on multi-axial multi-ply stitched preforms. Part 4. Mechanical properties of composites and damage observation,” Composites Part A: Applied Science and Manufacturing, vol. 36, no. 9, pp. 1207–1221, Sep. 2005, doi: 10.1016/j.compositesa.2005.02.004.

[47] S. K. Bhudolia and S. C. Joshi, “Low-velocity impact response of carbon fibre composites with novel liquid Methylmethacrylate thermoplastic matrix,” Composite Structures, vol. 203, pp. 696–708, Nov. 2018, doi: 10.1016/j.compstruct.2018.07.066.

[48] W. Obande, D. Mamalis, D. Ray, L. Yang, and C. M. Ó Brádaigh, “Mechanical and thermomechanical characterisation of vacuum-infused thermoplastic- and thermoset-based composites,” Materials & Design, vol. 175, p. 107828, Aug. 2019, doi: 10.1016/j.matdes.2019.107828.

[49] S. K. Bhudolia, P. Perrotey, and S. C. Joshi, “Optimizing Polymer Infusion Process for Thin Ply Textile Composites with Novel Matrix System,” Materials (Basel), vol. 10, no. 3, p. 293, Mar. 2017, doi: 10.3390/ma10030293.

[50] W. Obande, C. M. Ó Brádaigh, and D. Ray, “Continuous fibre-reinforced thermoplastic acrylic-matrix composites prepared by liquid resin infusion – A review,” Composites Part B: Engineering, vol. 215, p. 108771, Jun. 2021, doi: 10.1016/j.compositesb.2021.108771.

[51] M. A. Torabizadeh, “Tensile, compressive and shear properties of unidirectional glass/epoxy composites subjected to mechanical loading and low temperature services,” Indian Journal of Engineering and Materials Sciences, vol. 20, pp. 299–309, Aug. 2013.

[52] M. Gong, X. F. Wang, and J. H. Zhao, “Experimental study on mechanical behavior of laminates at low temperature,” Cryogenics, vol. 47, no. 1, pp. 1–7, Jan. 2007, doi: 10.1016/j.cryogenics.2006.01.018.

[53] Y. Shindo, S. Takano, F. Narita, and K. Horiguchi, “Tensile and damage behavior of plain weave glass/epoxy composites at cryogenic temperatures,” Fusion Engineering and Design, vol. 81, no. 20, pp. 2479–2483, Nov. 2006, doi: 10.1016/j.fusengdes.2006.07.059.

[54] S. KUMAGAI, Y. SHINDO, K. HORIGUCHI, and F. NARITA, “Experimental and Finite-Element Analysis of Woven Glass-Cloth/Epoxy Laminate Tensile Specimen at Room and Low Temperatures,” Mechanics of Advanced Materials and Structures, vol. 11, no. 1, pp. 51–66, Jan. 2004, doi: 10.1080/15376490490257666.

[55] D.-S. Li, C.-Q. Zhao, L. Jiang, N. Lu, L.-M. Chen, and N. Jiang, “A comparative study on the tensile properties and failure mechanism of 3D MWK composites at room and liquid nitrogen temperature,” Polym. Compos., vol. 35, no. 7, pp. 1294–1305, Jul. 2014, doi: 10.1002/pc.22780.

[56] M.-G. Kim, S.-G. Kang, C.-G. Kim, and C.-W. Kong, “Tensile response of graphite/epoxy composites at low temperatures,” *Composite Structures*, vol. 79, no. 1, pp. 84–89, Jun. 2007, doi: 10.1016/j.compstruct.2005.11.031.

[57] S. Kumagai, Y. Shindo, K. Horiguchi, and T. Takada, “Mechanical Characterization of CFRP Woven Laminates between Room Temperature and 4K,” *Jsme International Journal Series A-solid Mechanics and Material Engineering - JSME INT J A-SOLID MECH MAT E*, vol. 46, pp. 359–364, Jul. 2003, doi: 10.1299/jsmea.46.359.

[58] X. X. Chu, Z. X. Wu, R. J. Huang, Y. Zhou, and L. F. Li, “Mechanical and thermal expansion properties of glass fibers reinforced PEEK composites at cryogenic temperatures,” *Cryogenics*, vol. 50, no. 2, pp. 84–88, Feb. 2010, doi: 10.1016/j.cryogenics.2009.12.003.

[59] T. Gates, K. Whitley, R. Grenoble, and T. Bandorawalla, “Thermal/Mechanical Durability of Polymer-Matrix Composites in Cryogenic Environments1,” *Collection of Technical Papers -*

AIAA/ASME/ASCE/AHS/ASC Structures, Structural Dynamics and Materials Conference, vol. 3, Apr. 2003, doi: 10.2514/6.2003-1600.

[60] M. E. Kazemi, L. Shanmugam, D. Lu, X. Wang, B. Wang, and J. Yang, "Mechanical properties and failure modes of hybrid fiber reinforced polymer composites with a novel liquid thermoplastic resin, Elium®," Composites Part A: Applied Science and Manufacturing, vol. 125, p. 105523, Oct. 2019, doi: 10.1016/j.compositesa.2019.105523.

[61] S. K. Bhudolia, G. Gohel, J. Kantipudi, K. F. Leong, and P. Gerard, "Mechanical performance and damage mechanisms of thin rectangular carbon/ Elium® tubular thermoplastic composites under flexure and low-velocity impact," Thin-Walled Structures, vol. 165, p. 107971, Aug. 2021, doi: 10.1016/j.tws.2021.107971.

[62] T. Lorriot, J. Yagoubi, J. Fourel, and F. Tison, "Non-conventional Glass fiber NCF composites with thermoset and thermoplastic matrices," in Proc. 20th Int. Conf. Composite Materials (ICCM-20), Copenhagen, Denmark, Jul. 19–24, 2015.

[63] Cousins DS. Advanced thermoplastic composites for wind turbine blade manufacturing [Doctoral Thesis]. Colorado School of Mines; 2018.

[64] L. C. M. Barbosa, D. B. Bortoluzzi, and A. C. Ancelotti, "Analysis of fracture toughness in mode II and fractographic study of composites based on Elium® 150 thermoplastic matrix," Composites Part B: Engineering, vol. 175, p. 107082, Oct. 2019, doi: 10.1016/j.compositesb.2019.107082.

[65] S. K. Bhudolia, G. Gohel, D. Vasudevan, K. F. Leong, and P. Gerard, "On the Mode II fracture toughness, failure, and toughening mechanisms of wholly thermoplastic composites with ultra-lightweight thermoplastic fabrics and innovative Elium® resin," Composites Part A: Applied Science and Manufacturing, vol. 161, p. 107115, Oct. 2022, doi: 10.1016/j.compositesa.2022.107115.

[66] S. K. Bhudolia, G. Gohel, K. F. Leong, and S. C. Joshi, "Damping, impact and flexural performance of novel carbon/Elium® thermoplastic tubular composites," Composites Part B: Engineering, vol. 203, p. 108480, Dec. 2020, doi: 10.1016/j.compositesb.2020.108480.

[67] E. Boissin, C. Bois, J.-C. Wahl, and T. Palin-Luc, "Effect of temperature on damage mechanisms and mechanical behaviour of an acrylic-thermoplastic-matrix and glass-fibre-reinforced composite," Journal of Composite Materials, vol. 54, no. 27, pp. 4269–4282, Nov. 2020, doi: 10.1177/0021998320929056.

[68] L. Cadieu, J. B. Kopp, J. Jumel, J. Bega, and C. Froustey, “Temperature effect on the mechanical properties and damage mechanisms of a glass/thermoplastic laminate,” Journal of Composite Materials, vol. 54, no. 17, pp. 2271–2282, Jul. 2020, doi: 10.1177/0021998319894383.

[69] M. J. M. Fikry, Y. Arai, R. Inoue, V. Vinogradov, K. T. Tan, and S. Ogihara, “Damage Behavior in Unidirectional CFRP Laminates with Ply Discontinuity,” Appl Compos Mater, Mar. 2025, doi: 10.1007/s10443-025-10320-w.

[70] J. Montesano, Z. Fawaz, C. Poon, and K. Behdinan, “A microscopic investigation of failure mechanisms in a triaxially braided polyimide composite at room and elevated temperatures,” Materials & Design, vol. 53, pp. 1026–1036, Jan. 2014, doi: 10.1016/j.matdes.2013.08.003.

[71] S. Xu, S. He, J. Li, B. Xiao, and W. Zhang, “A progressive damage model for quasi-static tension of 2D woven composites and FEM implementation,” Composite Structures, vol. 320, p. 117168, Sep. 2023, doi: 10.1016/j.compstruct.2023.117168.

[72] A. Doitrand, C. Fagiano, V. Chiaruttini, F. H. Leroy, A. Mavel, and M. Hirsekorn, “Experimental characterization and numerical modeling of damage at the mesoscopic scale of woven polymer matrix composites under quasi-static tensile loading,” Composites Science and Technology, vol. 119, pp. 1–11, Nov. 2015, doi: 10.1016/j.compscitech.2015.09.015.

[73] Suratkar, Aaditya Pradeep, "Damage in Non-Crimp Fabric carbon fiber reinforced epoxy composites under various mechanical loading conditions" (2022). Electronic Thesis and Dissertation Repository. 8731. https://ir.lib.uwo.ca/etd/8731

[74] Z. Arwood, D. S. Cousins, S. Young, A. P. Stebner, and D. Penumadu, “Infusible thermoplastic composites for wind turbine blade manufacturing: Static characterization of thermoplastic laminates under ambient conditions,” Composites Part C: Open Access, vol. 11, p. 100365, Jul. 2023, doi: 10.1016/j.jcomc.2023.100365.

[75] K. M. Jespersen, J. Zangenberg, T. Lowe, P. J. Withers, and L. P. Mikkelsen, “Fatigue damage assessment of uni-directional non-crimp fabric reinforced polyester composite using X-ray computed tomography,” Composites Science and Technology, vol. 136, pp. 94–103, Nov. 2016, doi: 10.1016/j.compscitech.2016.10.006.

[76] M. Quaresimin, Fatigue in Composites (Second Edition). Woodhead Publishing Series in Composites Science and Engineering, Woodhead Publishing, 2025.

[77] John Montesano. Fatigue damage characterization of braided and woven fiber reinforced polymer matrix composites at room and elevated temperatures [Doctoral Thesis]. Ryerson University; 2012.

[78] I. Burhan and H. Kim, "S-N Curve Models for Composite Materials Characterisation: An Evaluative Review," Journal of Composites Science, vol. 2, p. 38, Jul. 2018, doi: 10.3390/jcs2030038.

[79] Z. Hashin, "Cumulative damage theory for composite materials: Residual life and residual strength methods," Composites Science and Technology, vol. 23, no. 1, pp. 1–19, Jan. 1985, doi: 10.1016/0266-3538(85)90008-9.

[80] T. P. Philippidis and V. A. Passipoularidis, "Residual strength after fatigue in composites: Theory vs. experiment," International Journal of Fatigue, vol. 29, no. 12, pp. 2104–2116, Dec. 2007, doi: 10.1016/j.ijfatigue.2007.01.019.

[81] N. L. Post, J. Cain, K. J. McDonald, S. W. Case, and J. J. Lesko, "Residual strength prediction of composite materials: Random spectrum loading," Engineering Fracture Mechanics, vol. 75, no. 9, pp. 2707–2724, Jun. 2008, doi: 10.1016/j.engfracmech.2007.03.002.

[82] Caprino G, "Residual Strength Prediction of Impacted CFRP Laminates," Journal of Composite Materials, vol. 18, no. 6, pp. 508-518, Nov. 1984, doi:10.1177/002199838401800601

[83] S. G. Lim and C. S. Hong, "Prediction of Transverse Cracking and Stiffness Reduction in Cross-Ply Laminated Composites," Journal of Composite Materials, vol. 23, no. 7, pp. 695–713, Jul. 1989, doi: 10.1177/002199838902300704.

[84] A. El Mahi, J.-M. Berthelot, and J. Brillaud, "Stiffness reduction and energy release rate of cross-ply laminates during fatigue tests," Composite Structures, vol. 30, no. 2, pp. 123–130, Jan. 1995, doi: 10.1016/0263-8223(94)00061-1.

[85] J.-H. Kim, F. Pierron, M. R. Wisnom, and K. Syed-Muhamad, "Identification of the local stiffness reduction of a damaged composite plate using the virtual fields method," Composites Part A: Applied Science and Manufacturing, vol. 38, no. 9, pp. 2065–2075, Sep. 2007, doi: 10.1016/j.compositesa.2007.04.006.

[86] P. Marguères and F. Meraghni, "Damage induced anisotropy and stiffness reduction evaluation in composite materials using ultrasonic wave transmission," Composites Part A:

Applied Science and Manufacturing, vol. 45, pp. 134–144, Feb. 2013, doi: 10.1016/j.compositesa.2012.09.007.

[87] P. A. Carraro and M. Quaresimin, “A stiffness degradation model for cracked multidirectional laminates with cracks in multiple layers,” International Journal of Solids and Structures, vol. 58, pp. 34–51, Apr. 2015, doi: 10.1016/j.ijsolstr.2014.12.016.

[88] M. Drvoderic, M. Gfrerrer, J. Wiener, G. Pinter, M. Pletz, and C. Schuecker, “Comparing crack density and dissipated energy as measures for off-axis damage in composite laminates,” International Journal of Fatigue, vol. 169, p. 107486, Apr. 2023, doi: 10.1016/j.ijfatigue.2022.107486.

[89] M. Simonetto, P. A. Carraro, L. Maragoni, and M. Quaresimin, “Crack initiation and evolution in glass/epoxy laminates under two-stage block loadings,” Composites Science and Technology, vol. 225, p. 109504, Jul. 2022, doi: 10.1016/j.compscitech.2022.109504.

[90] L. Maragoni, P. A. Carraro, M. Simonetto, and M. Quaresimin, “A novel method to include crack-induced delamination in a fatigue damage predictive procedure for composite laminates,” Composites Science and Technology, vol. 238, p. 110011, Jun. 2023, doi: 10.1016/j.compscitech.2023.110011.

[91] O. Castro, P. A. Carraro, L. Maragoni, and M. Quaresimin, “Fatigue damage evolution in unidirectional glass/epoxy composites under a cyclic load,” Polymer Testing, vol. 74, pp. 216–224, Apr. 2019, doi: 10.1016/j.polymertesting.2018.12.027.

[92] M. Quaresimin et al., “Damage evolution under cyclic multiaxial stress state: A comparative analysis between glass/epoxy laminates and tubes,” Composites Part B: Engineering, vol. 61, pp. 282–290, May 2014, doi: 10.1016/j.compositesb.2014.01.056.

[93] P. A. Carraro, L. Maragoni, and M. Quaresimin, “Damage evolution in cross-ply laminates under tension–compression and compression-compression cyclic loads,” Composites Part A: Applied Science and Manufacturing, vol. 156, p. 106888, May 2022, doi: 10.1016/j.compositesa.2022.106888.

[94] X. Li, R. Benedictus, and D. Zarouchas, “Early fatigue damage accumulation of CFRP Cross-Ply laminates considering size and stress level effects,” International Journal of Fatigue, vol. 159, p. 106811, Jun. 2022, doi: 10.1016/j.ijfatigue.2022.106811.

[95] S. Sánchez-Carmona, E. Correa, A. Barroso, and F. París, “Experimental observations of fatigue damage in cross-ply laminates using carbon/epoxy ultra-thin plies,” Composite Structures, vol. 306, p. 116564, Feb. 2023, doi: 10.1016/j.compstruct.2022.116564.

[96] F. Lamon, L. Maragoni, P. A. Carraro, and M. Quaresimin, “Fatigue damage evolution in woven composites with different architectures,” International Journal of Fatigue, vol. 167, p. 107365, Feb. 2023, doi: 10.1016/j.ijfatigue.2022.107365.

[97] J. Montesano, Z. Fawaz, K. Behdinan, and C. Poon, “Fatigue damage characterization and modeling of a triaxially braided polymer matrix composite at elevated temperatures,” Composite Structures, vol. 101, pp. 129–137, Jul. 2013, doi: 10.1016/j.compstruct.2013.01.030.

[98] J. Montesano, Z. Fawaz, and H. Bougherara, “Non-destructive assessment of the fatigue strength and damage progression of satin woven fiber reinforced polymer matrix composites,” Composites Part B: Engineering, vol. 71, pp. 122–130, Mar. 2015, doi: 10.1016/j.compositesb.2014.11.005.

[99] Z. Wu, F. Chen, Z. Pan, Z. Wu, X. Cheng, and K. Zheng, “Fatigue Behavior of Carbon Fiber Woven Composite Laminates with Different Off-Axis Angles Studied by Combining Infrared Thermography,” Fibers Polym, vol. 25, no. 3, pp. 1099–1110, Mar. 2024, doi: 10.1007/s12221-024-00508-5.

[100] J. Zangenberg, P. Brøndsted, and J. W. Gillespie, “Fatigue damage propagation in unidirectional glass fibre reinforced composites made of a non-crimp fabric,” Journal of Composite Materials, vol. 48, no. 22, pp. 2711–2727, Sep. 2014, doi: 10.1177/0021998313502062.

[101] M. Agrawal, M. Gupta, R. T. Durai Prabhakaran, and P. Mahajan, “A comparative study of static and fatigue performance of glass and basalt fiber reinforced epoxy composites,” Polymer Composites, vol. 45, no. 4, pp. 3551–3565, 2024, doi: 10.1002/pc.28008.

[102] K. M. Jespersen, J. A. Glud, J. Zangenberg, A. Hosoi, H. Kawada, and L. P. Mikkelsen, “Uncovering the fatigue damage initiation and progression in uni-directional non-crimp fabric reinforced polyester composite,” Composites Part A: Applied Science and Manufacturing, vol. 109, pp. 481–497, Jun. 2018, doi: 10.1016/j.compositesa.2018.03.002.

[103] D. Mattsson, R. Joffe, and J. Varna, “Damage in NCF composites under tension: Effect of layer stacking sequence,” Engineering Fracture Mechanics, vol. 75, no. 9, pp. 2666–2682, Jun. 2008, doi: 10.1016/j.engfracmech.2007.03.014.

[104] Rouf K *, Worswick M, Montesano J. Effect of strain rate on the in-plane orthotropic constitutive response and failure behaviour of a unidirectional non-crimp fabric composite. Composites Part A 2024;181:108166.

[105] Prajapati, A. Multiscale quantification of damage in composite structures. PhD Thesis, The University of Manchester, 2023.

[106] S. Hassani, M. Mousavi, and A. H. Gandomi, "Structural Health Monitoring in Composite Structures: A Comprehensive Review," Sensors, vol. 22, no. 1, p. 153, Dec. 2021, doi: 10.3390/s22010153.

[107] B. Wang, S. Zhong, T.-L. Lee, K. S. Fancey, and J. Mi, "Non-destructive testing and evaluation of composite materials/structures: A state-of-the-art review," Advances in Mechanical Engineering, vol. 12, no. 4, p. 1687814020913761, Apr. 2020, doi: 10.1177/1687814020913761.

[108] M. D. Crall, S. G. Laney, and M. W. Keller, "Multimodal Damage Detection in Self-Sensing Fiber Reinforced Composites," Advanced Functional Materials, vol. 29, no. 12, p. 1806634, 2019, doi: 10.1002/adfm.201806634.

[109] M. A. Hamstad, "A review: Acoustic emission, a tool for composite-materials studies," Experimental Mechanics, vol. 26, no. 1, pp. 7–13, Mar. 1986, doi: 10.1007/BF02319949.

[110] J. M. Berthelot and J. Rhazi, "Acoustic emission in carbon fibre composites," Composites Science and Technology, vol. 37, no. 4, pp. 411–428, Jan. 1990, doi: 10.1016/0266-3538(90)90012-T.

[111] F. Dahmene, S. Yaacoubi, and M. E. Mountassir, "Acoustic Emission of Composites Structures: Story, Success, and Challenges," Physics Procedia, vol. 70, pp. 599–603, 2015, doi: 10.1016/j.phpro.2015.08.031.

[112] M. BOURCHAK, I. FARROW, I. BOND, C. ROWLAND, and F. MENAN, "Acoustic emission energy as a fatigue damage parameter for CFRP composites," International Journal of Fatigue, vol. 29, no. 3, pp. 457–470, Mar. 2007, doi: 10.1016/j.ijfatigue.2006.05.009.

[113] J. Karger-Kocsis and Z. Fejes-Kozma, "Failure Mode and Damage Zone Development in a GMT-PP by Acoustic Emission and Thermography," Journal of Reinforced Plastics and Composites, vol. 13, no. 9, pp. 768–792, Sep. 1994, doi: 10.1177/073168449401300901.

[114] R. S. Williams and K. L. Reifsnider, “Investigation of Acoustic Emission During Fatigue Loading of Composite Specimens,” Journal of Composite Materials, vol. 8, no. 4, pp. 340–355, Apr. 1974, doi: 10.1177/002199837400800403.

[115] G. Maier, H. Ott, A. Protzner, and B. Protz, “Damage development in carbon fibre-reinforced polyimides in fatigue loading as a function of stress ratio,” Composites, vol. 17, no. 2, pp. 111–120, Apr. 1986, doi: 10.1016/0010-4361(86)90248-x.

[116] P. Mouritz, C. Townsend, and M. Z. Shah Khan, “Non-destructive detection of fatigue damage in thick composites by pulse-echo ultrasonics,” Composites Science and Technology, vol. 60, no. 1, pp. 23–32, Jan. 2000, doi: 10.1016/s0266-3538(99)00094-9.

[117] C. Scarponi and G. Briotti, “Ultrasonic Detection of Delaminations on Composite Materials,” Journal of Reinforced Plastics and Composites, vol. 16, no. 9, pp. 768–790, Jun. 1997, doi: 10.1177/073168449701600901.

[118] M. Beghini, L. Bertini, and E. Vitale, “Analysis of fatigue delamination growth in carboresin specimens with central hole,” Composite Structures, vol. 17, no. 3, pp. 257–274, Jan. 1991, doi: 10.1016/0263-8223(91)90054-3.

[119] H. Nayeb-Hashemi, M. D. Cohen, J. Zotos, and R. Poormand, “Ultrasonic characteristics of graphite/epoxy composite material subjected to fatigue and impacts,” Journal of Nondestructive Evaluation, vol. 5, no. 3–4, pp. 119–131, Dec. 1986, doi: 10.1007/bf00570621.

[120] H. Taheri and A. A. Hassen, “Nondestructive Ultrasonic Inspection of Composite Materials: A Comparative Advantage of Phased Array Ultrasonic,” Applied Sciences, vol. 9, no. 8, Art. no. 8, Jan. 2019, doi: 10.3390/app9081628.

[121] B. Yu, R. Blanc, C. Soutis, and P. J. Withers, “Evolution of damage during the fatigue of 3D woven glass-fibre reinforced composites subjected to tension–tension loading observed by time-lapse X-ray tomography,” Composites Part A: Applied Science and Manufacturing, vol. 82, pp. 279–290, Mar. 2016, doi: 10.1016/j.compositesa.2015.09.001.

[122] S. KELLAS, J. MORTON, and P. CURTIS, “A characteristic fatigue parameter for notched composites,” International Journal of Fatigue, vol. 13, no. 1, pp. 35–43, Jan. 1991, doi: 10.1016/0142-1123(91)90126-j.

[123] M. JEN, Y. KAU, and I. WU, “Fatigue damage in a centrally notched composite laminate due to two-step spectrum loading,” International Journal of Fatigue, vol. 16, no. 3, pp. 193–201, Apr. 1994, doi: 10.1016/0142-1123(94)90003-5.

[124] S. M. Spearing and P. W. R. Beaumont, “Fatigue damage mechanics of composite materials. I: Experimental measurement of damage and post-fatigue properties,” Composites Science and Technology, vol. 44, no. 2, pp. 159–168, Jan. 1992, doi: 10.1016/0266-3538(92)90109-g.

[125] T. W. Coats and C. E. Harris, “A Progressive Damage Methodology for Residual Strength Predictions of Notched Composite Panels,” Journal of Composite Materials, vol. 33, no. 23, pp. 2193–2224, Dec. 1999, doi: 10.1177/002199839903302303.

[126] X. Liu, D. Zhang, H. Qiu, J. Sun, C. Mao, and K. Qian, “On-axis fatigue behaviors and failure characterization of 3D5D braided composites with yarn-reduction using X-ray computed tomography,” Composites Science and Technology, vol. 203, p. 108585, Feb. 2021, doi: 10.1016/j.compscitech.2020.108585.

[127] S. C. Garcea, I. Sinclair, and S. M. Spearing, “Fibre failure assessment in carbon fibre reinforced polymers under fatigue loading by synchrotron X-ray computed tomography,” Composites Science and Technology, vol. 133, pp. 157–164, Sep. 2016, doi: 10.1016/j.compscitech.2016.07.030.

[128] S. C. Garcea, Y. Wang, and P. J. Withers, “X-ray computed tomography of polymer composites,” Composites Science and Technology, vol. 156, pp. 305–319, Mar. 2018, doi: 10.1016/j.compscitech.2017.10.023.

[129] J. Montesano, Z. Fawaz, and H. Bougherara, “Use of infrared thermography to investigate the fatigue behaviour of a carbon fiber reinforced polymer composite,” Composite Structures, vol. 97, pp. 76–83, Mar. 2013, doi: 10.1016/j.compstruct.2012.09.046.

[130] J. Montesano, H. Bougherara, and Z. Fawaz, “Application of infrared thermography for the characterization of damage in braided carbon fiber reinforced polymer matrix composites,” Composites Part B: Engineering, vol. 60, pp. 137–143, Apr. 2014, doi: 10.1016/j.compositesb.2013.12.053.

[131] L. TOUBAL, M. KARAMA, and B. LORRAIN, “Damage evolution and infrared thermography in woven composite laminates under fatigue loading,” International Journal of Fatigue, vol. 28, no. 12, pp. 1867–1872, Dec. 2006, doi: 10.1016/j.ijfatigue.2006.01.013.

[132] R. Steinberger, T. I. Valadas Leitão, E. Ladstätter, G. Pinter, W. Billinger, and R. W. Lang, "Infrared thermographic techniques for non-destructive damage characterization of carbon fibre reinforced polymers during tensile fatigue testing," International Journal of Fatigue, vol. 28, no. 10, pp. 1340–1347, Oct. 2006, doi: 10.1016/j.ijfatigue.2006.02.036.

[133] J. Huang, M. L. Pastor, C. Garnier, and X. J. Gong, "A new model for fatigue life prediction based on infrared thermography and degradation process for CFRP composite laminates," International Journal of Fatigue, vol. 120, pp. 87–95, Mar. 2019, doi: 10.1016/j.ijfatigue.2018.11.002.

[134] M. Seyyednourani, S. Akgun, H. Ulus, M. Yildiz, and H. S. Sas, "Experimental investigation on Compression-After-Impact (CAI) response of aerospace grade thermoset composites under low-temperature conditions assisted with acoustic emission monitoring," Composite Structures, vol. 321, p. 117260, Oct. 2023, doi: 10.1016/j.compstruct.2023.117260.

[135] C. Bu, G. Liu, X. Zhang, and Q. Tang, "Debonding defects detection of FMLs based on long pulsed infrared thermography technique," Infrared Physics & Technology, vol. 104, p. 103074, Jan. 2020, doi: 10.1016/j.infrared.2019.103074.

[136] W. H. Peters and W. F. Ranson, "Digital Imaging Techniques In Experimental Stress Analysis," Optical Engineering, vol. 21, no. 3, Jun. 1982, doi: 10.1117/12.7972925.

[137] D. Chambers, Digital Image Correlation: Advanced Methods and Applications. 2017.

[138] Y. L. Dong and B. Pan, "A Review of Speckle Pattern Fabrication and Assessment for Digital Image Correlation," Experimental Mechanics, vol. 57, no. 8, pp. 1161–1181, May 2017, doi: 10.1007/s11340-017-0283-1.

[139] B. Pan, "Digital image correlation for surface deformation measurement: historical developments, recent advances and future goals," Measurement Science and Technology, vol. 29, no. 8, p. 082001, Jun. 2018, doi: 10.1088/1361-6501/aac55b.

[140] M. L. Aparna, G. Chaitanya, K. Srinivas, and J. A. Rao, "Fatigue Testing of Continuous GFRP Composites Using Digital Image Correlation (DIC) Technique a Review," Materials Today: Proceedings, vol. 2, no. 4–5, pp. 3125–3131, 2015, doi: 10.1016/j.matpr.2015.07.275.

[141] X. Li, J. Kupski, S. Teixeira De Freitas, R. Benedictus, and D. Zarouchas, "Unfolding the early fatigue damage process for CFRP cross-ply laminates," International Journal of Fatigue, vol. 140, p. 105820, Nov. 2020, doi: 10.1016/j.ijfatigue.2020.105820.

[142] I. Miskdjian, M. Hajikazemi, and W. Van Paepegem, “Automatic edge detection of ply cracks in glass fiber composite laminates under quasi-static and fatigue loading using multi-scale Digital Image Correlation,” Composites Science and Technology, vol. 200, p. 108401, Nov. 2020, doi: 10.1016/j.compscitech.2020.108401.

[143] Pannier Y, Foti F, Gigliotti M. High temperature fatigue of carbon/polyimide 8-harness satin woven composites. Part I: digital Image Correlation and MicroComputed Tomography damage characterization. Compos Struct 2020;244. https://doi.org/10.1016/j.compstruct.2020.112255.

[144] F. Foti, Y. Pannier, and M. Gigliotti, “High temperature fatigue of carbon/polyimide 8-harness satin woven composites. Part II: Environmental effects,” Composite Structures, vol. 244, p. 112251, Jul. 2020, doi: 10.1016/j.compstruct.2020.112251.

[145] H. Shen, W. Yao, W. Qi, and J. Zong, “Experimental investigation on damage evolution in cross-ply laminates subjected to quasi-static and fatigue loading,” Composites Part B: Engineering, vol. 120, pp. 10–26, Jul. 2017, doi: 10.1016/j.compositesb.2017.02.033.

[146] J. J. Bender, B. L. V. Bak, S. M. Jensen, and E. Lindgaard, “Effect of variable amplitude block loading on intralaminar crack initiation and propagation in multidirectional GFRP laminate,” Composites Part B: Engineering, vol. 217, p. 108905, Jul. 2021, doi: 10.1016/j.compositesb.2021.108905.

[147] S. Korkiakoski, P. Brøndsted, E. Sarlin, and O. Saarela, “Influence of specimen type and reinforcement on measured tension–tension fatigue life of unidirectional GFRP laminates,” International Journal of Fatigue, vol. 85, pp. 114–129, Apr. 2016, doi: 10.1016/j.ijfatigue.2015.12.008.

[148] A. K. Bangaru, B. F. Sørensen, and L. P. Mikkelsen, “Three dimensional microscale characterization of off-axis tunnelling cracks in non-crimp fabric based composites,” *Composites Science and Technology*, vol. 226, p. 109502, Jul. 2022, doi: 10.1016/j.compscitech.2022.109502.

[149] J. Long, E. Shelhamer, and T. Darrell, “Fully Convolutional Networks for Semantic Segmentation,” Mar. 08, 2015, *arXiv*: arXiv:1411.4038. doi: 10.48550/arXiv.1411.4038.

[150] A. Krizhevsky, I. Sutskever, and G. E. Hinton, “ImageNet Classification with Deep Convolutional Neural Networks,” in Advances in Neural Information Processing Systems, Curran Associates, Inc., 2012. Accessed: Jan. 16, 2025. [Online]. Available:

https://proceedings.neurips.cc/paper_files/paper/2012/hash/c399862d3b9d6b76c8436e924a68c45b-Abstract.html

[151] A. Al-Azzawi, A. Ouadou, H. Max, Y. Duan, J. J. Tanner, and J. Cheng, "DeepCryoPicker: fully automated deep neural network for single protein particle picking in cryo-EM," BMC Bioinformatics, vol. 21, no. 1, p. 509, Nov. 2020, doi: 10.1186/s12859-020-03809-7.

[152] C. Szegedy et al., "Going Deeper with Convolutions," Sep. 17, 2014, arXiv: arXiv:1409.4842. doi: 10.48550/arXiv.1409.4842.P. Gavallas, G. Stefanou, D. Savvas, C. Mattrand, and J.-M. Bourinet, "CNN-based prediction of microstructure-derived random property fields of composite materials," Computer Methods in Applied Mechanics and Engineering, vol. 430, p. 117207, Oct. 2024, doi: 10.1016/j.cma.2024.117207.

[153] E. Karami, M. Shehata, and A. Smith, "Image Identification Using SIFT Algorithm: Performance Analysis against Different Image Deformations," Mar. 13, 2018, arXiv: arXiv:1710.02728. doi: 10.48550/arXiv.1710.02728.

[154] H. Bay, T. Tuytelaars, and L. Van Gool, "SURF: Speeded Up Robust Features," in Computer Vision – ECCV 2006, A. Leonardis, H. Bischof, and A. Pinz, Eds., Berlin, Heidelberg: Springer, 2006, pp. 404–417. doi: 10.1007/11744023_32.

[155] E. Rosten and T. Drummond, "Machine Learning for High-Speed Corner Detection," in Computer Vision – ECCV 2006, A. Leonardis, H. Bischof, and A. Pinz, Eds., Berlin, Heidelberg: Springer, 2006, pp. 430–443. doi: 10.1007/11744023_34.

[156] A. Goldenshluger and A. Zeevi, "The Hough transform estimator," The Annals of Statistics, vol. 32, no. 5, pp. 1908–1932, Oct. 2004, doi: 10.1214/009053604000000760.

[157] N. O. Mahony et al., Deep Learning vs. Traditional Computer Vision, vol. 943. 2020. doi: 10.1007/978-3-030-17795-9.

[158] Y. Gao, M. Berger, and R. Duddu, "CNN-Based Surrogate for the Phase Field Damage Model: Generalization across Microstructure Parameters for Composite Materials," Journal of Engineering Mechanics, vol. 149, no. 6, p. 04023025, Jun. 2023, doi: 10.1061/JENMDT.EMENG-6936.

[159] G. Ammasai Sengodan, "Prediction of two-phase composite microstructure properties through deep learning of reduced dimensional structure-response data," Composites Part B: Engineering, vol. 225, p. 109282, Nov. 2021, doi: 10.1016/j.compositesb.2021.109282.

[160] C. Yang, Y. Kim, S. Ryu, and G. X. Gu, “Prediction of composite microstructure stress-strain curves using convolutional neural networks,” Materials & Design, vol. 189, p. 108509, Apr. 2020, doi: 10.1016/j.matdes.2020.108509.

[161] O. Ronneberger, P. Fischer, and T. Brox, “U-Net: Convolutional Networks for Biomedical Image Segmentation,” in Medical Image Computing and Computer-Assisted Intervention – MICCAI 2015, N. Navab, J. Hornegger, W. M. Wells, and A. F. Frangi, Eds., Cham: Springer International Publishing, 2015, pp. 234–241. doi: 10.1007/978-3-319-24574-4_28.

[162] K. Zhu, W. Cao, C. Ran, and B. Gu, “A novel automatic crack classification algorithm of 3-D woven composites based on deep-learning U-Net model,” Engineering Fracture Mechanics, vol. 289, p. 109488, Sep. 2023, doi: 10.1016/j.engfracmech.2023.109488.

[163] B. de Oliveira, A. Seibert, V. Borges, A. Albertazzi Jr, and R. Schmitt, “Employing a U-net convolutional neural network for segmenting impact damages in optical lock-in thermography images of CFRP plates,” Nondestructive Testing and Evaluation, vol. 36, pp. 1–19, May 2020, doi: 10.1080/10589759.2020.1758099.

[164] J. Dong, A. Kandemir, and I. Hamerton, “Microstructural characterisation of fibre-hybrid polymer composites using U-Net on optical images,” *Composites Part A: Applied Science and Manufacturing*, vol. 190, p. 108569, Mar. 2025, doi: 10.1016/j.compositesa.2024.108569.

[165] J. P. C Bertoldo, E. Decencière, D. Ryckelynck, and H. Proudhon, “A Modular U-Net for Automated Segmentation of X-Ray Tomography Images in Composite Materials,” Frontiers in Materials, vol. 8, Nov. 2021, doi: 10.3389/fmats.2021.761229.

[166] M. E. Kazemi, L. Shanmugam, D. Lu, X. Wang, B. Wang, and J. Yang, “Mechanical properties and failure modes of hybrid fiber reinforced polymer composites with a novel liquid thermoplastic resin, Elium®,” Composites Part A: Applied Science and Manufacturing, vol. 125, p. 105523, Oct. 2019, doi: 10.1016/j.compositesa.2019.105523.

[167] M. Zivkovic. Manufacturing of a fiber-reinforced thermoplastic composite micro-generating wind turbine blade. MASc Thesis, University of Waterloo, 2023.

[168] N. Han, I. Baran, J. S. M. Zanjani, O. Yuksel, L. An, and R. Akkerman, “Experimental and computational analysis of the polymerization overheating in thick glass/Elium® acrylic thermoplastic resin composites,” *Composites Part B: Engineering*, vol. 202, p. 108430, Dec. 2020, doi: 10.1016/j.compositesb.2020.108430.

[169] Matteo Rosso. Process Development and Characterization of Novel VARTM Fiber-reinforced Thermoplastic Composites. Master's Thesis, Politecnico Di Torino, 2020.

[170] Liquid thermoplastic resin for tougher composites. https://www.arkema.com/files/live/sites/shared_arkema/files/downloads/products-documentations/liquid-thermoplastic-resinfor-tougher-composites.pdf

[171] Technical Data Sheet for Pro-Set INF-114/INF-211, Rev 7, Dec 2021.

[172] M. Merzkirch and T. Foecke, "10° off-axis testing of CFRP using DIC: A study on strength, strain and modulus," Compos. Part B Eng., vol. 196, p. 108062, Sep. 2020, doi: 10.1016/j.compositesb.2020.108062.

[173] C. C. Chamis and J. H. Sinclair, "Ten-deg off-axis test for shear properties in fiber composites," Exp. Mech., vol. 17, no. 9, pp. 339–346, Sep. 1977, doi: 10.1007/BF02326320.

[174] M. Merzkirch and T. Foecke, "Investigation of the Interlaminar Shear Properties of Fiber Reinforced Polymers via Flexural Testing using Digital Image Correlation," Mater. Perform. Charact., vol. 9, no. 5, p. https://doi.org/10.1520/mpc20190206, 2020.

[175] "ASTM International - ASTM D5379/D5379M-19E1 - Standard Test Method for Shear Properties of Composite Materials by the V-Notched Beam Method | GlobalSpec." https://standards.globalspec.com/std/14376572/ASTM%20D5379/D5379M-19e1 (accessed Sep. 14, 2023).

[176] "Standard Test Method for Shear Properties of Composite Materials by V-Notched Rail Shear Method." https://www.astm.org/d7078_d7078m-05.html (accessed Sep. 14, 2023).

[177] B. Yang, Z. Yue, X. Geng, P. Wang, J. Gan, and B. Liao, "Effects of space environment temperature on the mechanical properties of carbon fiber/bismaleimide composites laminates," Proceedings of the Institution of Mechanical Engineers, Part G: Journal of Aerospace Engineering, vol. 232, no. 1, pp. 3–16, Nov. 2017, doi: 10.1177/0954410017740382.

[178] ASTM D3039-17. Standard test method for tensile properties of polymer matrix composite materials. ASTM Int 2017. http://dx.doi.org/10.1520/D3039_D3039M- 17.

[179] J. Hohe et al., "Performance of fiber reinforced materials under cryogenic conditions—A review," Composites Part A: Applied Science and Manufacturing, vol. 141, p. 106226, Feb. 2021, doi: 10.1016/j.compositesa.2020.106226.

[180] F. Sharifpour, J. Montesano, and R. Talreja, “Assessing the effects of ply constraints on local stress states in cross-ply laminates containing manufacturing induced defects,” Composites Part B: Engineering, vol. 199, p. 108227, Oct. 2020, doi: 10.1016/j.compositesb.2020.108227.

[181] S. S. Bamane, P. P. Deshpande, S. U. Patil, M. Maiaru, and G. M. Odegard, “Evolution of Physical, Thermal, and Mechanical Properties of Poly(methyl Methacrylate)-Based Elium Thermoplastic Polymer During Polymerization,” J. Phys. Chem. C, vol. 128, no. 37, pp. 15639–15648, Sep. 2024, doi: 10.1021/acs.jpcc.4c04061.

[182] X. X. Chu, Z. X. Wu, R. J. Huang, Y. Zhou, and L. F. Li, “Mechanical and thermal expansion properties of glass fibers reinforced PEEK composites at cryogenic temperatures,” Cryogenics, vol. 50, no. 2, pp. 84–88, Feb. 2010, doi: 10.1016/j.cryogenics.2009.12.003.

[183] Y. Shindo, T. Takeda, and F. Narita, “Mechanical response of nonwoven polyester fabric/epoxy composites at cryogenic temperatures,” Cryogenics, vol. 52, no. 10, pp. 564–568, Oct. 2012, doi: 10.1016/j.cryogenics.2012.07.008.

[184] M. C. Lafarie-Frenot and C. Hénaff-Gardin, “Formation and growth of 90° ply fatigue cracks in carbon/epoxy laminates,” Composites Science and Technology, vol. 40, no. 3, pp. 307–324, Jan. 1991, doi: 10.1016/0266-3538(91)90087-6.

[185] E. Boissin, C. Bois, J.-C. Wahl, and T. Palin-Luc, “Effect of temperature on damage mechanisms and mechanical behaviour of an acrylic-thermoplastic-matrix and glass-fibre-reinforced composite,” Journal of Composite Materials, vol. 54, no. 27, pp. 4269–4282, Nov. 2020, doi: 10.1177/0021998320929056.

[186] ASTM, D 3479/D 3479M–19. Standard test method for tension–tension fatigue of polymer matrix composite materials. ASTM, International, 2023.

[187] J. Huang, M.-L. Pastor, C. Garnier, and X. Gong, “Rapid evaluation of fatigue limit on thermographic data analysis,” International Journal of Fatigue, vol. 104, pp. 293–301, Nov. 2017, doi: 10.1016/j.ijfatigue.2017.07.029.

[188] Hosoi A, Takamura K, Sato N, Kawada H. “Quantitative evaluation of fatigue damage growth in CFRP laminates that changes due to applied stress level,” Int J Fatigue 2011;33(6):781–7. https://doi.org/10.1016/j.ijfatigue.2010.12.017.

[189] A. Arteiro, G. Catalanotti, J. Reinoso, P. Linde, and P. P. Camanho, “Simulation of the Mechanical Response of Thin-Ply Composites: From Computational Micro-Mechanics to

Structural Analysis," Arch Computat Methods Eng, vol. 26, no. 5, pp. 1445–1487, Nov. 2019, doi: 10.1007/s11831-018-9291-2.

[190] A. Arteiro, G. Catalanotti, A. R. Melro, P. Linde, and P. P. Camanho, "Micro-mechanical analysis of the in situ effect in polymer composite laminates," Composite Structures, vol. 116, pp. 827–840, Sep. 2014, doi: 10.1016/j.compstruct.2014.06.014.

[191] F. Sharifpour and J. Montesano, "A three-dimensional micromechanical model for simulating ply crack formation in laminates under in-plane tensile loading," Composites Part A: Applied Science and Manufacturing, vol. 162, p. 107120, Nov. 2022, doi: 10.1016/j.compositesa.2022.107120.

[192] C. R. Harris et al., "Array programming with NumPy," Nature, vol. 585, no. 7825, pp. 357–362, Sep. 2020, doi: 10.1038/s41586-020-2649-2.

[193] B. S. Reddy and B. N. Chatterji, "An FFT-based technique for translation, rotation, and scale-invariant image registration," IEEE Transactions on Image Processing, vol. 5, no. 8, pp. 1266–1271, Aug. 1996, doi: 10.1109/83.506761.

[194] H. Foroosh, J. B. Zerubia, and M. Berthod, "Extension of phase correlation to subpixel registration," IEEE Transactions on Image Processing, vol. 11, no. 3, pp. 188–200, Mar. 2002, doi: 10.1109/83.988953.

[195] CVAT.ai, "Computer Vision Annotation Tool (CVAT)," GitHub. [Online]. Available: https://github.com/cvat-ai/cvat. Accessed: Aug. 11, 2024.

[196] V. I. Petkov, V. R. Pakkam Gabriel, and P. Fernberg, "Semantic segmentation of progressive micro-cracking in polymer composites using Attention U-Net architecture," Tomography of Materials and Structures, vol. 5, p. 100028, Jun. 2024, doi: 10.1016/j.tmater.2024.100028.

[197] R. Azad et al., "Medical Image Segmentation Review: The Success of U-Net," IEEE Transactions on Pattern Analysis and Machine Intelligence, vol. 46, no. 12, pp. 10076–10095, Dec. 2024, doi: 10.1109/TPAMI.2024.3435571.

[198] N. Srivastava, G. Hinton, A. Krizhevsky, I. Sutskever, and R. Salakhutdinov, "Dropout: a simple way to prevent neural networks from overfitting," J. Mach. Learn. Res., vol. 15, no. 1, pp. 1929–1958, 2014.

Appendix A

E. Shi and J. Montesano, “Effect of low temperature on the mechanical properties and failure characteristics of an infused non-crimp fabric glass fiber-reinforced reactive thermoplastic,” (Submitted to Composites Science and Technology_- Under Review)

“Accessible through the University of Waterloo’s Institutional Repository (UW Space)”

Appendix B

E. Shi and J. Montesano, “Characterization of damage in non-crimp fabric glass fiber-reinforced reactive thermoplastic composites at low temperature using an in-situ digital imaging technique,” Composites Part A: Applied Science and Manufacturing, vol. 190, p. 108674, Mar. 2025, doi: 10.1016/j.compositesa.2024.108674.

“Accessible through the University of Waterloo’s Institutional Repository (UW Space)”

Appendix C

E. Shi and J. Montesano, “Integrated digital imaging technique for correlation of damage evolution and stiffness degradation in non-crimp fabric composite materials under cyclic loading,” Composite Structures, vol. 371, p. 119513, Nov. 2025, doi: 10.1016/j.compstruct.2025.119513.

“Accessible through the University of Waterloo’s Institutional Repository (UW Space)”

Appendix D

E. Shi, J. Montesano, Y. Zeng, and K. Rouf, “Deep Learning-Assisted Damage Characterization in Non-crimp Fabric Composites,” (Submitted to Composites Science and Technology - Under Review)

“Accessible through the University of Waterloo’s Institutional Repository (UW Space)”